COMPUTATIONAL MODELING OF FLUID–STRUCTURE INTERACTION IN BIOLOGICAL FLYING AND SWIMMING

By

Hu Dai

Dissertation

Submitted to the Faculty of the

Graduate School of Vanderbilt University

in partial fulfillment of the requirements

for the degree of

DOCTOR OF PHILOSOPHY

in

Mechanical Engineering

May, 2013

Nashville, Tennessee

Approved:

Professor Haoxiang Luo (Chair)

Professor Amrutur Anilkumar

Professor Jon Edd

Professor Caglar Oskay

Professor D. Greg Walker

Acknowledgments

CONTENTS

LIST OF TABLES

LIST OF FIGURES

NOMENCLATURE

v_i, V_j	cell-center and face-center fluid velocity
p	pressure
α	angular amplitude, or weight of the interpolation stencil
h	membrane thickness
ϕ	phase delay
A	area, or tail excursion
ρ_f, ρ_s	density of fluid, density of solid
ν	viscosity of fluid, or Poisson's ratio
c	chord length
U	freestream velocity, or mean tip velocity
L	wing length
Re	Reynolds number
St	Strouhal number
f_o	flapping frequency
ω^*	frequency ratio
m^*	mass ratio
$\mathcal{AR}$	aspect ratio
I	second moment of area
E, G	Young's modulus, shear modulus
K	reduced stiffness
P	power
η	efficiency
C_L, C_D, C_P, C_T	lift, drag, power and thrust coefficients
T	period

CHAPTER I

INTRODUCTION

1.1   Aerodynamics of flapping flight

Insects, birds, and bats are very common flyers in nature. These animals flap their wings in certain manners to acquire sufficient lift to keep themselves aloft, to propel through the air, and to maneuver in complex environment. Flapping flight has been studied by biologists for many years and enjoys renewed interests among engineers due to the advent of micro air vehicles (MAVs) or unmanned air vehicles (UAVs). These vehicles have a wide range of military and civilian applications such as surveillance and environmental monitoring. Different from traditional aircrafts, MAVs and UAVs are small-sized and usually operate at relatively low Reynolds numbers (below 10^5). Current designs of these vehicles are mostly based on conventional fixed wings or on rotary wings. Inspired by great agility of the flyers in nature, biomimetic wings with flapping motions could potentially revolutionize of the MAVs and UAVs by drastically improving their maneuverability. Therefore, a thorough understanding of the unsteady aerodynamics of flapping wings becomes a key component in the development of the bio-inspired aerial vehicles.

Early studies found that the traditional aerodynamics theory largely underestimated the force production by insects and based on the theory the insects can not even stay aloft in air. This dilemma has then led to researchers' attention to unsteady aerodynam-

ics which turned out to be substantial in explaining the mechanisms employed by insects (Weis-Fogh & Jensen, 1956). Weis-Fogh (1973) first proposed a 'Clap and fling' mechanism which accounts for the additional lift produced by a hovering insect. Lighthill (1973) modeled this mechanism and solved it analytically under the assumption of two-dimensional inviscid flow. Edwards & Cheng (1982) proposed an improved model incorporating vortex separation. Ellington *et al.* (1996) visualized the leading-edge vortex generated by flapping wings and pointed out that the 'dynamic stall' mechanism could explain the large lift of flapping wings. Dickinson *et al.* (1999) then used a scaled fruit-fly model in an oil tank, and they found that significant lift peaks were produced by the wake capture after the wing reversal. Wang (2000) used a two-dimensional numerical simulation to show that a hovering wing can generate enough lift to support the weight of the insect. Sun *et al.* did a series of three-dimensional numerical studies with a fruit-fly model to further study the unsteady flow and the effect of wing kinematics on the lift production and power requirements, and they also discussed the flight stability of an insect during steady maneuver through their numerical study (Sun & Tang, 2002*a*,*b*; Sun & Du, 2003; Sun & Wu, 2003; Sun & Wang, 2007).

Those early studies have mainly focused rigid wings, and the role of the wing flexibility only starts to draw attentions from aerodynamicists in recent years (Shyy *et al.*, 2010). Given that the structural deformation is common in flapping wings, it is reasonable to believe that such a feature helps to enhance the aerodynamic performance of the wings. The passive deformation of insects have been discussed by several biologists. For example, Ennos (1988*b*) showed the importance of the vein properties in torsion and bending in creating a camber on the wing chord, and he demonstrated that

the inertial load of the wing is large enough to account for the wing rotation during reversal. Combes & Daniel (2003*a*) studied the flexural stiffness of insect wings and they believe that the wing deformation is mostly caused by the inertial load. Despite these relevant studies, the detailed study on the aerodynamics of flexible flapping wings is still rare, and the cause of the observed wing deformation pattern has not been well explained. There have been a few recent studies focusing on flexible wings (Young *et al.*, 2009; Eldredge *et al.*, 2010), but these studies are limited to specified wing deformation or two-dimensional models. Therefore, the aeroelasticity of flapping wings is still a largely unaddressed topic.

1.2   Fish swimming and related research works

Another area closely related to flapping flight is fish swimming. Majority of fish use body/caudal fin (BCF) for propulsion; others use median or pectoral fins (MPF) for their routine propulsive mode. Those fish relying on the BCF mode utilize the MPF mode instead for maneuvering and stabilization (Videler, 1993). Analogous to the air vehicles that are inspired by flying animals, unmanned underwater vehicles (UUVs) mimicking the propulsive modes of fish have great potential to achieve high efficiency and maneuverability. Also similar to the flapping flight, the flow around fish fins is typically three-dimensional, unsteady, and largely separated. Therefore, in many situations the fluid dynamics in the two problems can be studied in the same way.

Pitching and heaving foils of simple shape in an incidental flow is frequently used as a model to study the thrust production of the fin. Substantial work has been done on the

hydrodynamics of rigid pitching and heaving foils. Early theoretical studies were based on linear inviscid theory of unsteady foil flow (Wu, 1961, 1971; Lighthill, 1960), and experimental studies were done by Koochesfahani (1989); Triantafyllou *et al.* (1991, 1993); Anderson *et al.* (1998). The unsteady wake behind the foil on average was found to be like a jet flow, and vortices closely resemble the von Karman vortex street behind bluff objects but have reversed rotation. In addition, the thrust efficiency is largely dependent on the Strouhal number, defined as the ratio between the transverse velocity of the tail and the freestream velocity. A review of these studies can be found in Triantafyllou *et al.* (2004). More recently, Schnipper *et al.* (2009) investigated the effect of the oscillation frequency and amplitude on the wake structures produced by a pitching foil in a soap film flow. For the foil at low aspect ratios where the flow is essentially three-dimensional, Buchholz *et al.* studied a rigid panel pitching around its leading edge in a free stream (Buchholz & Smits, 2006, 2008). They found that the thrust coefficient depends on both the Strouhal number and the aspect ratio and that the propulsive efficiency is sensitive to the aspect ratio when the span-to-chord ratio is less than 0.83. Dong *et al.* numerically studied a pitching/heaving foil of elliptic shape and investigated the three-dimensional topology of the wake (Dong *et al.*, 2006).

More realistic swimming kinematics has also been incorporated into computational studies of fish hydrodynamics. Using a 3D model fish, Borazjani & Sotiropoulos (2008) studies the carangiform locomotion at various Reynolds numbers and Strouhal numbers, and they explained from a hydrodynamic perspective why the carangiform swimming mode is preferred by fast swimmers in nature. Besides the cruising mode, there have been great interests in the kinematics and hydrodynamics of fish turning (see P & RW,

4

1997). For example, Epps & Techet (2007) studied the vortex dynamics during a typical C-start turning that is typically employed by fish during an escape.

1.3   Wing/fin flexibility: observations and the fluid dynamics

Biological propulsors are usually highly flexible. For example, the jointed fin rays of fish deform both actively and passively during swimming so that the fin changes its area and curvature (Lauder & Madden, 2007). Bird wings also deform significantly while flapping. In addition to the active muscle control of the joint motions that adjusts the wing span and planform, there are passive deformations due to the flexible feathers (Shyy *et al.*, 2008). One of the phenomena caused by passive feather motions is the popped up covert feathers on the upper surface to control flow separation (Bechert *et al.*, 1997). Bats have many independently controlled joints in their wings, highly deformable bones (Swartz *et al.*, 1992), and compliant thin-membrane wing surfaces that enable a wide variation of the angle of attack and the wing camber. These features give bats a complex wing topology and are very important to the flight performance of these animals (Shyy *et al.*, 2008). The membranous wings of flying insects are usually very flexible as well and they display considerable passive deformations during flight (Wootton, 1981, 1992; Combes & Daniel, 2003*b*; Lauder, 2000). In general, the deformation pattern of an insect wing can be described by bending and spanwise twist around the wing axis. These deformation features alter the instantaneous angle of attack, speed of stroke, and pitching velocity (angular velocity around the spanwise axis). Wu *et al.* measured thrust generation of several wing designs using

a test rig that flaps the wings (Wu *et al.*, 2010). Significant thrust was produced due to the passive feathering, twisting, and bending of their membrane wings. Additionally, wing torsion may create a dynamic camber (Ennos, 1988*a*) which could improve the lift production. Therefore, the wing deformation has significant aerodynamic consequences in insect flight. Earlier studies on the low-Reynolds-number aerodynamics of flapping wings have mainly focused on rigid wings (e.g. Dickinson *et al.*, 1999; Sun & Tang, 2002*b*; Wang, 2005). Among the existing studies on the aerodynamics of flexible wings, several have shown that by adding some level of passive flexibility to a rigid flapping wing, the performance of the wing can be significantly improved. For example, Vanella *et al.* used a two-link model to represent the chordwise flexibility (Vanella *et al.*, 2009). Their two-dimensional (2D) simulation shows that the wing deformation can increase the lift-to-drag ratio by 28% and the lift-to-power ratio by 39% and that the best performance is obtained when the flapping frequency is a fraction of the natural frequency of the wing structure. Using a similarly simplified model, Eldredge *et al.* investigated the effect of chordwise deformation over a range of hovering kinematic parameters (Eldredge *et al.*, 2010). They found that a mildly flexible wing consistently has better power efficiency compared to the rigid wing for a wide range of phase differences between pitching and wing translation. In addition to these computational studies, experiments performed in liquid (e.g. Prempraneerach *et al.*, 2003; Heathcote & Gursul, 2007*a*) and in air (Ramananarivo *et al.*, 2011) showed that the chordwise deformation can significantly enhance the propulsive force and efficiency of the wing. Despite these studies, there have been little work on the three-dimensional fluid-structure interaction of the flapping wings (this includes fish fins), mostly due to

the computational challenge involved in the simulation. Consequently, details of the role of the structural flexibility in the animal flight and swimming await further investigation.

1.4   Research Methods

Theoretical analysis of flapping wings and fins has been done using extremely idealized models under the assumption of linear inviscid flow Lighthill (1960, 1973), or using a quasi-steady treatment (Wang *et al.*, 2004). In more general situations, theoretical solutions are not available due to the complexity of the flow field. Therefore, experimental and computational approaches become indispensable. Experiments could be done in a wind tunnel or liquid tank with real animals or physical models of the wings and fins. However, the flow visualization in experiments is typically limited to two-dimensional slices, and the forces in many situations are not easy to measure. Furthermore, the dynamic similarity for a flexible wing is difficult to achieve because it is often impractical to match the Reynolds number, mass ratio, and dimensionless rigidity at the same time. Therefore, the numerical simulation is an important tool for understanding the fluid dynamics of flapping wings and fins.

Numerical approaches for simulating biological locomotion hinges on how to treat the moving boundaries. In addition, the fluid–structure interaction poses great challenges. Conventional numerical solvers are usually based on the finite-volume method or the finite-element method that employs the body-conformal grid. Such a grid has to adapt to the geometry change when a solid surface is moving. Therefore mesh regenera-

tion is required, and the computation can become very expensive. On the other hand, the immersed-boundary method has gain popularities for moving-boundary and complex-geometry problems by employing simple and fixed meshes (Mittal & Iaccarino, 2005). There are several other methods using fixed and structured grids for moving-boundary problems. For example, a finite-element method combined with a fictitious-domain formulation was developed to simulate particle-laden flows, where the rigid-body motion inside the particle volume is enforced through Lagrange multipliers; a penalty/fictitious-domain method was designed to handle solid surfaces and to simulate particle-laden or multiphase flows (Khadra *et al.*, 2000; Randrianarivelo *et al.*, 2005; Sarthou *et al.*, 2008); and a ghost-fluid approach was developed to solve compressible flows (Fedkiw *et al.*, 1999). Compared to these methods, the sharp-interface immersed-boundary method based on flow reconstruction near the solid surface has proven to be an accurate and efficient approach for simulating biological flying and swimming problems (Mittal *et al.*, 2008).

1.5   The specific objectives of this study

Given that an appropriate computational tool for simulating the fluid–structure interaction of biological flying and swimming is still lacking and the role of the structural flexibility in the fluid dynamics of the flapping flight/swimming is still poorly understood, we have proposed the following specific research objectives in this study:

- Develop an accurate and efficient numerical method for computational modeling of the three-dimensional fluid–structure interaction of flapping wings/fins in

nature; the method will combine an immersed-boundary method for the viscous incompressible flow and and a nonlinear finite-element method for thin-walled structures.

- Use the pitching/heaving/revolving thin foils at low aspect ratios as simple models to study the fundamental effect of the structural flexibility on the force production and on the three-dimensional flow.

- Investigate the parameterization of real insect wings and develop a high-fidelity computational modeling approach to study the aeroelasticity and its role in the aerodynamics of the real insect wings.

The thesis is organized as follows.

- In Chapter 2, we describe the immersed-boundary method that has been developed in our lab for the viscous incompressible Navier–Stokes equation. The finite-difference discretization, the boundary treatment, and the remedy to suppress the numerical oscillations associated with moving boundaries will be described. Validation cases will be presented to show the accuracy and versatility of the method. In addition, the finite-element method for modeling thin-wall structures will be introduced, and the approach for fluid–structure coupling will be described.

- In Chapter 3, we adopt a simple flexible pitching foil as a fish fin model to study its thrust performance. The pitching amplitude/frequency and the structural flexibility are systematically varied. We investigate the effect of the passive deformation on the thrust production and study the scaling law of the flexible foil.

- In Chapter 4, we use a rectangular plate flapping around a pivot point to represent the hovering motion of an insect. The interplay of the wing inertia, the aerodynamic force, and the elastic force is investigated by varying the mass ratio and the rigidity of the plate, and the effect of the dynamic deformation of the wing on the performance of the wing is examined in detail. In addition, the implication of the result on the insect wings is discussed.

- In Chapter 5, we describe a high-fidelity modeling approach for modeling the cicada forewing, where experiment studies are performed to measure the mechanical properties of the wing structure and to quantify the three-dimensional wing kinematics during tethered flight. The computational model includes the finite-element modeling of the vein network, the fluid–structure simulation, and the validation of the simulated wing deformation. The role of the wing flexibility in the aerodynamic performance is studied by comparing the flexible wing model and the rigid wing model and also by comparing the cambered wing and the uncambered wing.

- In Chapter 6, we summarize the current work and its contributions. The future direction of the work will be discussed.

CHAPTER II

NUMERICAL APPROACH

2.1   Flow solver

2.1.1   Governing equations and the finite-difference discretization

The flow is governed by the viscous incompressible Navier-Stokes equations. The momentum equation and the continuity equation are written as

$$
\begin{aligned}
\frac{\partial u_i}{\partial t} + \frac{\partial u_j u_i}{\partial x_j} &= -\frac{1}{\rho}\frac{\partial p}{\partial x_i} + \nu\frac{\partial^2 u_i}{\partial x_j^2}, \\
\frac{\partial u_i}{\partial x_i} &= 0,
\end{aligned}
\tag{2.1}
$$

where u_i is the velocity, ρ and ν are the constant density and viscosity, and p is the pressure. The governing equations are discretized on a nonuniform Cartesian grid using a cell-centered, non-staggering arrangement of the primitive variables, u_i and p. The incompressible momentum equation is integrated in time using a variation of Chorin's projection method which consists of three sub-steps (Chorin, 1968). In the first sub-step, an advection–diffusion equation is solved in the absence of the pressure, and an intermediate velocity field, u_i^*, is obtained. In this step, both the nonlinear advection terms and the viscous terms are discretized using the Crank–Nicolson scheme to im-

11

prove the numerical stability. The discrete equation is written as

$$\frac{u_i^* - u_i^n}{\Delta t} + \frac{1}{2}\left[\frac{\delta(U_j u_i)^*}{\delta x_j} + \frac{\delta(U_j u_i)^n}{\delta x_j}\right] = \frac{\nu}{2}\left[\frac{\delta}{\delta x_j}\left(\frac{\delta u_i^*}{\delta x_j}\right) + \frac{\delta}{\delta x_j}\left(\frac{\delta u_i^n}{\delta x_j}\right)\right], \quad (2.2)$$

where U_j is the velocity discretized at the face center of a computational cell, and $\frac{\delta}{\delta x_j}$ represents a finite-difference approximation of the spatial derivative using a second-order central scheme. The nonlinear algebraic system is solved by a successive substitution approach.

In the second sub-step, a projection function is solved as an approximation of the pressure,

$$\frac{\delta}{\delta x_j}\left(\frac{\delta p^{n+1}}{\delta x_j}\right) = \frac{\rho}{\Delta t}\frac{\delta U_j^*}{\delta x_j}, \quad (2.3)$$

and an inhomogeneous Neumann boundary condition is imposed at all boundaries. In our serial code the Poisson equation (2.3) is solved with an efficient geometric multigrid method, as discussed in Mittal *et al.* (2008), and in the parallel version it forms a large linear system solved with AZTEC package. Once the pressure is obtained, the cell-centered velocity is updated as

$$u_i^{n+1} = u_i^* - \frac{\Delta t}{\rho}\frac{\delta p^{n+1}}{\delta x_i}, \quad (2.4)$$

and the final face-centered velocity, U_i^{n+1}, is updated by averaging u_i^{n+1} along the j-direction.

2.1.2   The immersed boundary method

In recent years, the immersed-boundary method that is based on the structured mesh has gained considerable popularity in computational fluid dynamics for solving complex and moving-boundary problems. Despite its wide applications, so far there is not a unified definition of the method, possibly because there are many variations in the existing implementations. Here we follow the classification approach by Mittal & Iaccarino (2005) where the immersed-boundary method is in general classified into two types. One type involves a diffused boundary whose effect on the flow field is incorporated as a volumetric force spread into the bulk fluid, typically within the distance of a few grid cells from the physical boundary (Peskin, 1972; Goldstein *et al.*, 1993). The volumetric force may be determined from the constitutive law in case of an elastic boundary (Peskin, 1972, 2002), or by a feedback mechanism in which the force depends on the difference between the interpolated velocity at the interface and the desired boundary condition (Goldstein *et al.*, 1993). The other type of the immersed-boundary method retains the singular representation of the physical boundary and thus the nature of the surface force exerted by the boundary on the adjacent fluid. This type of "sharp-interface" methods can typically achieve higher order of accuracy than the "diffuse-interface" methods. Several distinct sharp-interface approaches have been formulated in the past to treat the boundary conditions at the fluid–solid interface. For example, in the "cut-cell" approach by Udaykumar *et al.* (2001), a finite-volume scheme is designed to represent the conservation equations for the irregular cells cut through by the boundary, whereas the bulk flow is discretized using the standard finite-difference method. In the method presented by LeVeque & Li (1994); Lee & Leveque (2003),

13

the solution experiences discontinuities across the physical interface immersed in the domain, and the finite-difference formulae involving the nodes across the interface are corrected by taking into consideration of the discontinuities.

In another type of sharp-interface methods, an unknown forcing term is introduced only at the nodal points immediately next to the fluid–solid interface, whose direction and magnitude are such that the boundary conditions at the location of the fluid–solid interface are satisfied. The forcing does not have to be explicitly calculated but can be incorporated through a local flow field reconstruction around the forcing points. To reconstruct the flow locally, an interpolation scheme is applied, and the pressure and velocity information at the fluid–solid interface are included as input data in the scheme. Therefore, the boundary conditions at the interface are enforced through the interpolation, and actual evaluation of the forcing is never needed. Since there is no feedback iteration involved, this method is also termed "direct forcing" approach. Many existing implementations fall into this category (Fadlun *et al.*, 2000; Kim *et al.*, 2001; Tseng & Ferziger, 2003; Yang & Balaras, 2006; Mittal *et al.*, 2008; Berthelsen & Faltinsen, 2008; Pan & Shen, 2009; Vanella & Balaras, 2009).

In the direct-forcing approach, the construction of the interpolation stencil is flexible and may take several topological forms. Figure 2.1 shows some of the examples of the stencil. For simplicity, we only use a non-staggered grid for illustration. The interpolation points may be located either on the fluid side of the interface (Fig. 2.1(a,c)), or on the solid side (Fig. 2.1(b,d)). In the latter case, the values of the flow variables at the points inside the solid body can be considered a smooth extrapolation of the physical flow field (and thus, no discontinuity across the interface is involved). In Fig. 2.1(a,b),
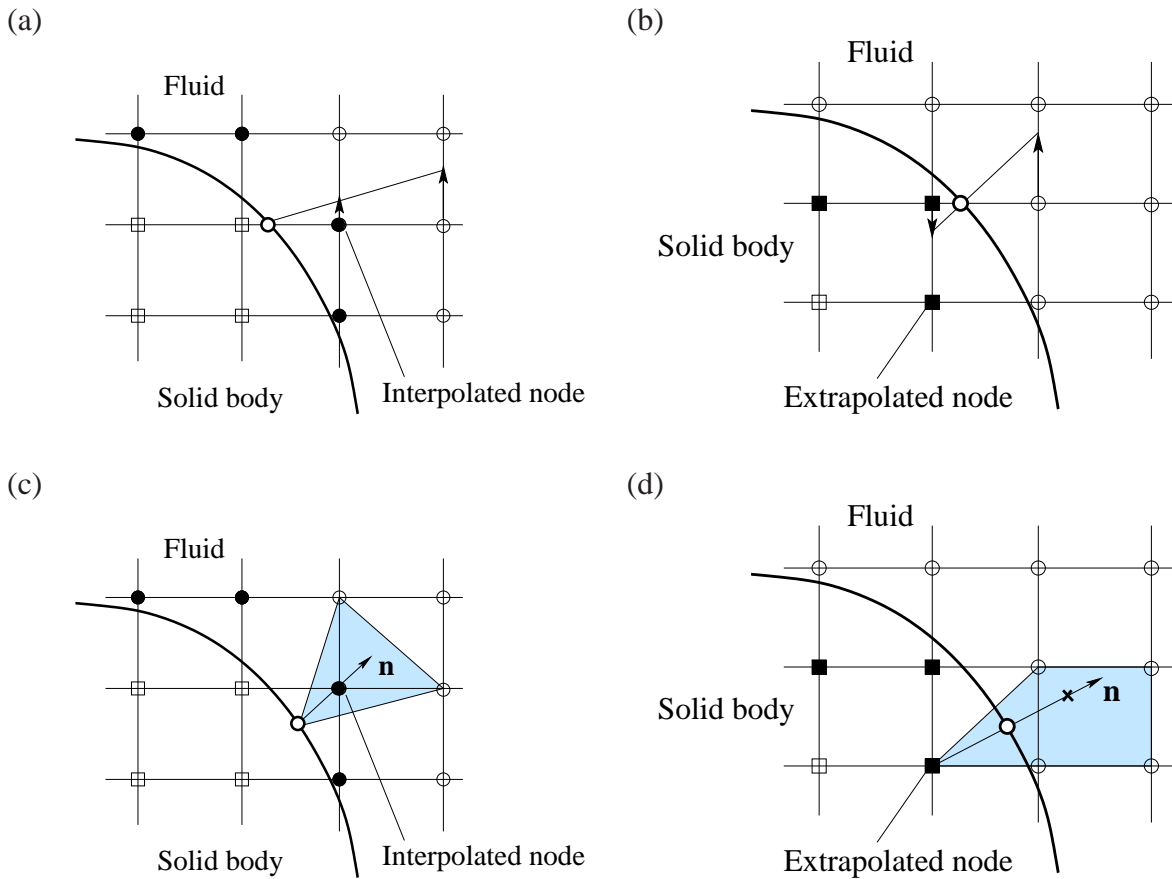
Figure 2.1: Illustration of the flow field reconstruction near the immersed boundary using different interpolation stencils. (a,b) Unidirectional interpolations; (c,d) two-dimensional interpolations where **n** is the surface normal and the shaded area represents the region of support for the interpolation/extrapolation. The interpolation points are on the fluid side in (a,c) and on the solid body side in (b,d).

the interpolation is carried out along the direction of one coordinate. Given boundary

conditions at the body-intercept with the coordinate line (unfilled circle in the figure),

the fluid velocity at the node marked by a filled circle or square is interpolated from

the flow field, and for the rest of the nodes on the fluid side, a standard finite-difference

stencil can be applied to discretize the Navier–Stokes equation. Examples of previous

works that adopted this strategy include Fadlun *et al.* (2000) and Berthelsen & Faltinsen

(2008) among others.

In Fig. 2.1(c,d), a two-dimensional local region around the interpolation point is

chosen, and the normal intersect of the point with the interface is used to determine the region of support in the stencil (correspondingly, a three-dimensional region is chosen for a 3D problem). This strategy, used by several previous works (Tseng & Ferziger, 2003; Yang & Balaras, 2006; Mittal *et al.*, 2008), has been more popular compared to the unidirectional interpolation shown in Fig. 2.1(a,b) since using the closest point on the interface in the interpolation would reduce the numerical error. In addition to these examples, other flow reconstruction strategies have also been adopted, e.g., the least squares fitting (Vanella & Balaras, 2009) where the reconstruction is independent of the mesh topology.

Compared to the other sharp-interface methods such as the cut-cell (Udaykumar *et al.*, 2001) and the discontinuity methods (LeVeque & Li, 1994; Lee & Leveque, 2003), the direct-forcing or flow-reconstruction approach is much simpler in formulation and implementation. In addition, the reconstruction procedure does not incur significant computational cost, and like the other methods, it maintains the order of accuracy of the finite-difference discretization of the bulk flow. Given its advantages, the direct-forcing approach is particularly attractive and has been applied in many problems, especially in biological flows (Yang & Balaras, 2006; Mittal *et al.*, 2008) where the boundaries are typically highly complex and a boundary-conforming mesh is difficult to generate. However, one drawback of the method is that it is prone to temporal oscillations when the boundary is moving (Uhlmann, 2005; Berthelsen & Faltinsen, 2008; Pan & Shen, 2009; Liao *et al.*, 2010). Specifically, pressure fluctuations may happen when a boundary moves across the nodal points on the fixed volumetric mesh and the numerical description of the boundary nodes changes instantaneously between

the standard finite-difference formula and the flow reconstruction. To illustrate the problem, we use the interpolation stencil shown in Fig. 2.2 as an example and provide a brief explanation. As shown in Fig. 2.2(a), when the boundary advances into the fluid region, some of the interpolated nodes may become occupied by the solid body, and nearby nodes in bulk fluid region will thus be defined as the new locations of interpolation. Correspondingly, the stencil at the latter nodes and the numerical description associated with the stencil changes immediately from those for the discrete Navier–Stokes equation to those for the flow field interpolation. Similarly, the immediate switch of the stencil may occur for some of the nodes when the immersed boundary retreats from the fluid region, as shown in Fig. 2.2(b). Such instantaneous change of the numerical description at the boundary nodes creates a temporal discontinuity in the velocity. The discontinuity is further amplified by a factor of $1/\Delta t$ for the right-hand side of the pressure Poisson equation when solving an incompressible flow, thus causing the force to oscillate significantly. From this perspective, the artificial oscillations as seen previously are caused by the inconsistent treatments between the boundary nodes and the bulk flow, and sudden change of the numerical descriptions from one time step to next has created the temporal jump. In Section 2.2, we will give more detailed discussion of this problem.

It has been limited study about the numerical oscillation associated with the direct-forcing approach. Uhlmann (2005) pointed out that the methods of Kim *et al.* (2001) and Fadlun *et al.* (2000) had led to strong force oscillations when simulating flows interacting with rigid particles, and thus he adopted a diffuse-interface approach instead. Berthelsen & Faltinsen (2008) dealt with stationary-boundary flows and only pointed

17
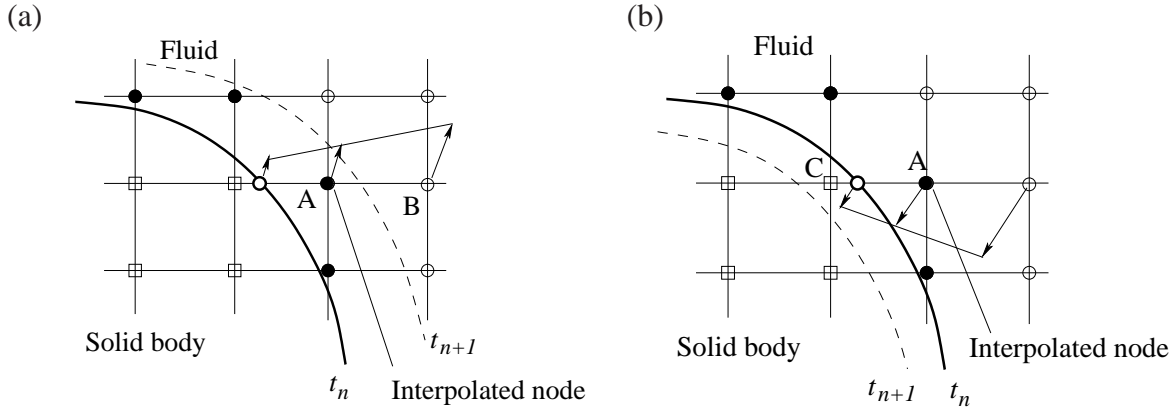
Figure 2.2: Illustrations of the moving boundary where the numerical description at some nodes undergoes instantaneous change as the boundary moves across the grid points.

out the potential problem with moving boundaries. Pan & Shen (2009) illustrated the force oscillations that appeared in their simulation for a moving-cylinder problem, but reduced the oscillations by *increasing* the size of time step. In another work, Liao *et al.* (2010) introduced a forcing term within the solid body when solving the momentum equation. The treatment appears to suppress the force oscillations in their numerical tests. However, it is not clear why the treatment would work or how the treatment could be extended to other direct-forcing implementations.

2.1.3 Numerical oscillations caused by moving boundaries

Using the discretization approach introduced in Section 2.1.1, we now elaborate on how a direct-forcing method could cause numerical oscillations. As an example, we use the specific interpolation approach shown in Fig. 2.2(a) to explain our point. The nodal points in the figure represent the location of the cell centers on a Cartesian mesh. Eq. (2.2) is discretized at the nodes in the bulk flow region which are marked by open

circles in Fig. 2.1(a). The velocity at the points immediately next the boundary (marked by filled circles) is interpolated from the boundary velocity and neighboring fluid node using a linear function as shown. Thus, the discrete Navier–Stokes equation and the interpolation form a closed algebraic system for the velocity at all the nodes on the fluid side of the domain, which may be solved using an iterative approach.

In a moving-boundary problem, the role of a grid point varies as the immersed boundary moves across the point. That is, an interior fluid node may become an interpolated node as the boundary intrudes on the fluid region, or an interpolated node may become an interior fluid node as the boundary withdraws from the fluid region. In the topology shown in Fig. 2.2(a) where the boundary moves into the fluid region, node A will be occupied by the solid body at the next time step, and the fluid node B thus will become a point of interpolation. Therefore, the stencil for the velocity at node B changes from the finite-difference stencil for the discrete Navier–Stokes equation at time level n suddenly to the interpolation stencil for the flow reconstruction at the next time level, $n + 1$. Although both discrete schemes are valid approximations of the same flow field that is physically continuous. However, the two different descriptions are associated with discretization errors of their own characteristics, which in general are not consistent to each other. Therefore, the difference between the two types of error creates a temporal discontinuity in the velocity, as node B switches from an interior fluid node to a boundary node. Similarly, the temporal discontinuity is incurred as the boundary withdraws from the fluid region as shown in Fig. 2.2(b), where node A becomes immediately a regular fluid node and meanwhile node C becomes an interpolated node.
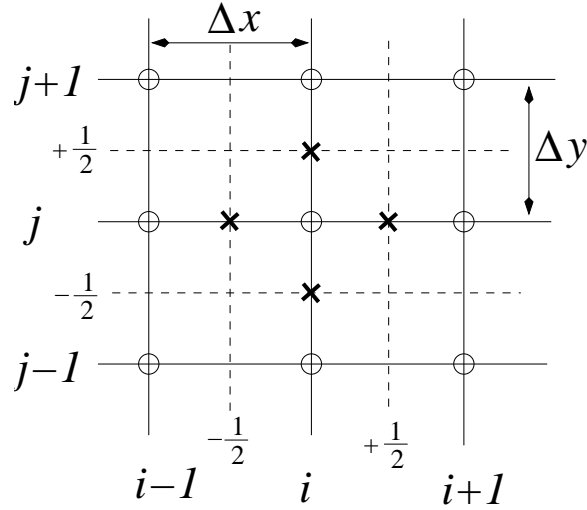
Figure 2.3: A 2D uniform grid showing the finite-difference scheme used in the current study, where the circles are the cell centers and the crosses are the face centers.

In the present case, since both the flow interpolation and the finite-discretization employ a second-order accurate approach, then the numerical errors associated with both stencils are of $O(\Delta x^2)$, and therefore, the difference between them should also be of $O(\Delta x^2)$. However, the corresponding temporal discontinuity for the right-hand-side term of the projection equation, Eq. (2.3), is amplified by a factor of $1/\Delta t$. Note that since the error is inversely proportional to the size of the time step, the resulting pressure oscillation will in fact increase when a smaller Δt is used. It should also be pointed out that the magnitude of the temporal jump depends on the difference between the discretization error of the finite-difference approximation and the interpolation error, and thus, increasing the order of accuracy for the interpolation alone does not necessarily reduce the magnitude of the jump. In order to attenuate the jump, one could increase the spatial resolution around the boundary or utilize higher order schemes for both the finite-difference discretization and the interpolation. However, both of these two approaches would increase the computational cost.

2.1.4   The improved immersed-boundary treatment

Noticing that the numerical oscillation is caused by the instantaneous switch of the numerical description for the nodes near the immersed boundary, we propose a remedy where the temporal discontinuity can be regularized by introducing a smooth transition of the stencils.

In the present numerical method, the surface of the solid body is represented by a set of Lagrangian marker points and linear elements, i.e., line segments in two dimensions and flat triangles in three dimensions. This representation allows efficient calculations of the geometrical quantities, e.g., the surface normal, the interpolation of a variable over the surface, and the location of a nodal point with respect to the interface (either inside or outside of the solid body) (Mittal *et al.*, 2008). To impose the velocity and pressure boundary conditions at the interface, we define ghost cells and hybrid cells near the interface as follows. When a standard second-order central difference scheme is used to discretize the Navier–Stokes equation in the fluid region, incomplete stencils are encountered near the interface. Specifically, at the nodes immediately next to the interface, the finite-difference stencil will involve nodes that are located inside the solid body. These special "fluid nodes" are termed here "hybrid nodes", and the corresponding nodes inside the solid body are termed "ghost nodes". These definitions are illustrated in Fig. 2.4 in two dimensions. Note that the present categorization of the ghost cells is the same as that in Mittal *et al.* (2008), and the categorization of the present hybrid cells is the same as that for the "forcing points" in Yang & Balaras (2006). Next, we will discuss separately the treatment for the ghost cells and for the hybrid cells.

2.1.5   Field extrapolation for the ghost nodes

The treatment of the ghost nodes is essentially the same as that in Mittal *et al.* (2008), and it is summarized here to facilitate the subsequent discussion of the hybrid nodes. We use Fig. 2.4(a) to illustrate a 2D situation, but the corresponding 3D formulation is also provided in the discussion. To formulate a numerical description for a ghost node which incorporates the boundary condition, the body intercept (BI) and the image point (IP) of the ghost node across the boundary are found by projecting the ghost node onto the boundary along the surface normal. Note that when the size of the triangular elements on the surface is comparable to or larger than that of the computational cells nearby, such a projection point may not be found. In that case, an edge point on the surface that is closest to the ghost node is chosen as the body intercept (Mittal *et al.*, 2008). The generic variable, ϕ, in the local area around the image point is approximated by the following interpolating polynomial,

$$\phi(x, y) \quad = \quad c_1 xy + c_2 x + c_3 y + c_4,$$

$$\phi(x, y, z) \quad = \quad c_1 xyz + c_2 xy + c_3 yz + c_4 xz + c_5 x + c_6 y + c_7 z + c_8, \tag{2.5}$$

for 2D and 3D, respectively, where c_m, $m = 1, 2, \ldots, N$, are the polynomial coefficients ($N = 4$ for 2D and 8 for 3D). The interpolated value at the image point takes the form

$$\phi_{\text{IP}} = \sum_{m}^{N} \beta_m \phi_m, \tag{2.6}$$

where ϕ_m is one of the N data points, and β_m is the corresponding weight determined from the interpolating polynomial.

To determine β_i, the vertices on the cube enclosing the image point are used as the interpolation data points, as shown in Fig. 2.4(a) for the ghost node A. In the case where the corresponding ghost node is one of the vertices, e.g., the ghost node B in Fig. 2.4(a), the body intercept is used instead as a data point to replace the ghost node, and the boundary condition for ϕ at the BI is called upon to complete the equations for the coefficients of the polynomial. The boundary condition can either be the Dirichlet condition (for the velocity), $\phi = \phi_{\text{BI}}$, or the Neumann condition (for the pressure), $\partial\phi/\partial\mathbf{n} = [(\partial\phi/\partial x, \partial\phi/\partial y, \partial\phi/\partial z)\cdot\mathbf{n}]$. In the latter case, $\partial\phi/\partial\mathbf{n}$ is used as one of the data points in (2.6).

The velocity at the ghost node (GN) is then obtained through the following linear approximations along the surface normal,

$$\mathbf{u}_{\text{GN}} + \mathbf{u}_{\text{IP}} = 2\,\mathbf{u}_{\text{BI}}, \tag{2.7}$$

and the pressure at the ghost node is obtained through the approximation

$$\left.\frac{\partial p}{\partial\mathbf{n}}\right|_{\text{BI}} = \frac{p_{\text{IP}} - p_{\text{GN}}}{\Delta l} = \left.-\rho\frac{D\mathbf{u}}{Dt}\cdot\mathbf{n}\right|_{\text{BI}}, \tag{2.8}$$

where Δl is the distance from IP to GN, and the inhomogeneous boundary condition for the pressure, $\partial p/\partial\mathbf{n} = -\rho(D\mathbf{u}/Dt)\cdot\mathbf{n}$ has been assumed. Here $D\mathbf{u}/Dt$ represents the material derivative of the velocity and can be easily interpolated over the surface from the acceleration of the Lagrangian marker points. The equations (2.6) to (2.8) complete
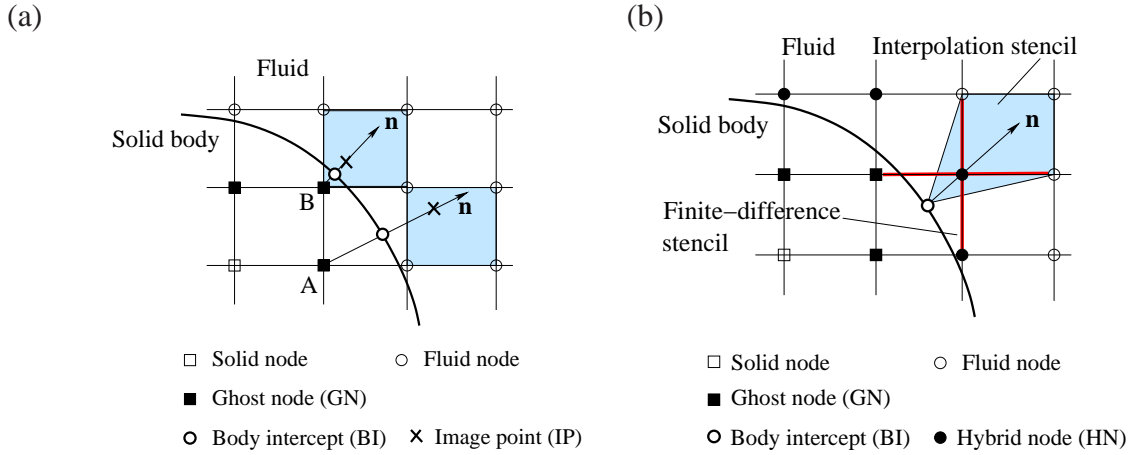
Figure 2.4: Two-dimensional schematics illustrating the immersed-boundary method used in the present solver. (a) The field extrapolation stencil for the ghost nodes defined inside the solid body. (b) The mixed interpolation/finite-difference stencil for the hybrid nodes defined inside the fluid region. The cross in (b) represents the second-order central difference stencil. The shaded areas are the support regions for the interpolating polynomials.

the numerical descriptions for the ghost-node velocity and pressure, and the boundary

conditions at the body intercept have been imposed through these descriptions.

2.1.6   Velocity treatment at the hybrid nodes

With the flow variables described at the ghost nodes, the governing equations (2.2)

to (2.4) could be discretized at all the nodes located on the fluid side. However, we

introduce a mixed stencil for the hybrid nodes, which are the fluid nodes near the im-

mersed boundary and are marked by filled circles in Fig. 2.4(b). The new numerical

description for the hybrid nodes is a combination of the discrete Navier–Stokes equa-

tion and interpolation, which are shown in Fig. 2.4(b) by a five-point (seven-point in

3D) finite-difference stencil and a polygonal region, respectively. We will require that

the numerical description undergo a smooth transition as the hybrid nodes move toward

24

or away from the immersed boundary. More specifically, the closer a hybrid node is to the solid body, the more dominated is the mixed stencil by the flow reconstruction. On the other hand, the farther the hybrid node is to the solid body, the more dominated is the stencil by the discrete Navier–Stokes equation. To formulate the hybrid-node treatment, we shall first discuss separately the discretization of the momentum equation and the interpolation.

For simplicity, we shall use a uniform grid and 2D illustration as shown in Fig. 2.3, and we will only show the treatment for the u-velocity component. The treatments for the other velocity components are exactly the same. At a hybrid node (i, j), the advection–diffusion equation, Eq. (2.2), can be expanded as

$$
\begin{aligned}
\frac{u_{i,j}^* - u_{i,j}^n}{\Delta t} \quad &+ \quad \frac{U_{i+\frac{1}{2},j}^*(u_{i+1,j}^* + u_{i,j}^*) - U_{i-\frac{1}{2},j}^*(u_{i-1,j}^* + u_{i,j}^*)}{4\Delta x} \\
&+ \quad \frac{V_{i,j+\frac{1}{2}}^*(u_{i,j+1}^* + u_{i,j}^*) - V_{i,j-\frac{1}{2}}^*(u_{i,j-1}^* + u_{i,j}^*)}{4\Delta y} \\
&+ \quad \frac{\delta(Uu)^n}{2\delta x}\bigg|_{i,j} + \frac{\delta(Vu)^n}{2\delta y}\bigg|_{i,j} \\
&= \quad \frac{\nu}{2}\left(\frac{u_{i+1,j}^* - 2u_{i,j}^* + u_{i-1,j}^*}{\Delta x^2} + \frac{u_{i,j+1}^* - 2u_{i,j}^* + u_{i,j-1}^*}{\Delta y^2}\right) \\
&+ \quad \frac{\nu}{2}\left(\frac{\delta}{\delta x}\frac{\delta u^n}{\delta x} + \frac{\delta}{\delta y}\frac{\delta u^n}{\delta y}\right),
\end{aligned}
\tag{2.9}
$$

where U and V are the face-center velocity components and only the implicit terms, indicated by an asterisk, have been expanded. The explicit terms at time level n would follow the same spatial discretization. Eq. (2.9) can be re-arranged into

$$
\left(1 + \frac{\Delta t}{2}N_U^* - \frac{\nu\Delta t}{2}D\right)u_{i,j}^* = R_{i,j}^*,
\tag{2.10}
$$

25

where N_U^* represents the coefficient of $u_{i,j}^*$ from the nonlinear terms and D the coefficient from the linear terms, i.e.,

$$
\begin{aligned}
N_U^* &= \frac{U_{i+\frac{1}{2},j}^* - U_{i-\frac{1}{2},j}^*}{2\Delta x} + \frac{V_{i,j+\frac{1}{2}}^* - V_{i,j-\frac{1}{2}}^*}{2\Delta y} \\
D &= -\frac{2}{\Delta x^2} - \frac{2}{\Delta y^2},
\end{aligned}
\tag{2.11}
$$

and R_i^* is the summation of all the rest terms in Eq. (2.9), which include both the explicit terms and the implicit terms that contain the intermediate velocity from the neighboring nodes. Eq. (2.10) is then expressed in the scalar form

$$
u_{i,j}^* = \left(1 + \frac{\Delta t}{2}N_U^* - \frac{\nu\Delta t}{2}D\right)^{-1} R_{i,j}^* = g^* R_{i,j}^*,
\tag{2.12}
$$

where

$$
g^* = \left(1 + \frac{\Delta t}{2}N_U^* - \frac{\nu\Delta t}{2}D\right)^{-1}.
\tag{2.13}
$$

To design an interpolation scheme for the hybrid node (HN), we project the node onto the immersed boundary along the surface normal and find the body intercept (BI), as shown in Fig. 2.4(b). Extending the line that connects the BI and the hybrid node into the fluid region, it will intersect with a cube on which the hybrid node is located. The cube is termed interpolation cube. The velocity field in the local region around the hybrid node is then interpolated by the bilinear polynomial in Eq. (2.5), and the four data points used to determine the polynomial coefficients include the three vertices on the interpolation cube, excluding the hybrid node itself, and the BI, as illustrated by

26

the shaded region in Fig. 2.4(b). The interpolated u-velocity at the hybrid node is thus written as

$$u^*_{i,j} = \sum_{m=1}^{4} \beta_m u^*_{(m)}, \qquad (2.14)$$

where $u^*_{(m)}$ is the intermediate velocity at the mth data point, and β_m is the corresponding weight calculated from the interpolating polynomial.

To derive the mixed stencil, we combine Eq. (2.12) and Eq. (2.14) using the following expression,

$$u^*_{i,j} = (1 - \alpha)g^* R^*_{i,j} + \alpha \sum_{m=1}^{4} \beta_m u^*_{(m)}. \qquad (2.15)$$

where $0 \leq \alpha \leq 1$ is the weight of the interpolation stencil and its calculation will be discussed later. Thus, the velocity at the hybrid node is a weighted average between the Navier–Stokes solution and the interpolated value. Similar expressions can be obtained for 3D and for the v and w velocity components in a straightforward manner.

Another view of the weighted average is that the expression given by (2.15) minimizes the following cost function

$$f(u^*_{i,j}) = (1 - \alpha)\left[u^*_{i,j} - g^* R^*_{i,j}\right]^2 + \alpha\left[u^*_{i,j} - \sum_{j=m}^{4} \beta_m u^*_{(m)}\right]^2. \qquad (2.16)$$

Differentiate f with respect to $u^*_{i,j}$, and assume that $g^* R^*_{i,j}$ has insignificant dependence on $u^*_{i,j}$ (this is because the N^*_U term in $g*$ is on order of Δt). Requiring that the derivative $\mathrm{d}f/\mathrm{d}u^*_{i,j}$ vanish, we obtain the solution in the form of Eq. (2.15).

27

The constant α in Eq. (2.15) determines the relative importance of the interpolated velocity compared to the solution of the advection–diffusion equation. To determine α, we specify the following principles:

1. As the hybrid node becomes a regular fluid node, α should approach zero.

2. As the hybrid node becomes a ghost node in the solid body, α should approach unity.

3. In general, α should increase if the hybrid node moves toward the boundary, and decrease if the hybrid node moves away from the boundary.

According to these principles, as a solid node moves across the boundary into the fluid region and changes its role from a ghost node to a hybrid node and later to a regular fluid node, the velocity at the node will be first calculated through the flow field extrapolation as specified by Eq. (2.7), then through the hybrid expression Eq. (2.15), and finally through the advection–diffusion equation, Eq. (2.2). In Eq. (2.15), α gradually changes from unity to zero as the node moves away from the boundary, therefore allowing a temporally smooth transition of the numerical description near the boundary.

To find an appropriate algorithm for the weight α that satisfies the aforementioned guidelines, we use the information of the ghost nodes that are next to the hybrid node. As shown by the 2D schematic in Fig. 2.5(a), the ghost nodes next to the hybrid node HN are G1 in the x-direction and G2 in the y-direction. Here we assume that each hybrid node has at most two ghost node neighbors and exclude the situation where a fluid node is cut out by the boundary from more than two directions (i.e., sharp inner corners). Let Δ_1 and Δ_2 denote the distances to the boundary from the x- and y-ghost

28
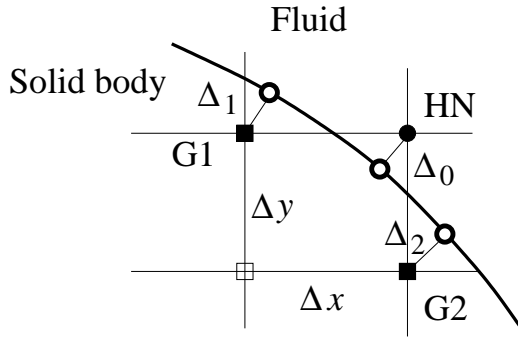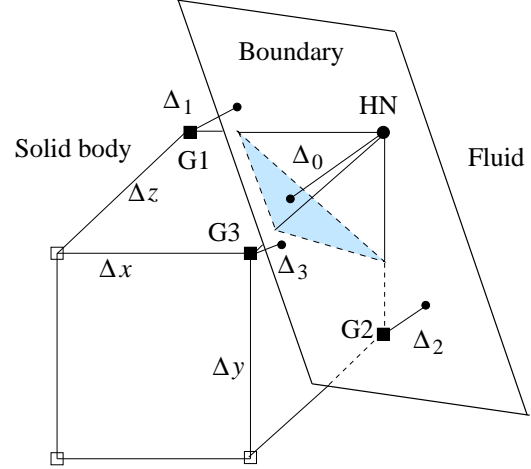
Figure 2.5: The 2D (a) and 3D (b) schematic illustrating calculation of the weight α, which specifies the relative importance of the interpolation in the mixed stencil for the hybrid node HN. In (b), the shaded region represents the intersection of the boundary with the cube.

node, respectively. We then compute α from the following expression

$$\alpha = \sqrt{\left(\frac{\Delta_1}{\Delta x}\right)^2 + \left(\frac{\Delta_2}{\Delta y}\right)^2}, \tag{2.17}$$

where Δx and Δy are the grid intervals in the x- and y-directions. If the hybrid node has only one neighboring ghost node, then the irrelevant term in Eq. (2.17) is undefined and is simply set to zero. Note that if the radius of the local curvature of the boundary is large compared to the cell size and the boundary is assumed to be a straight line, then α given by Eq. (2.17) is always between zero and unity. One could alternatively compute α based on the lengths of the edges cut through by the interface, which would involve computation of the intersections.

Extending the algorithm for α to three dimensions, we have

$$\alpha = \sqrt{\left(\frac{\Delta_1}{\Delta x}\right)^2 + \left(\frac{\Delta_2}{\Delta y}\right)^2 + \left(\frac{\Delta_3}{\Delta z}\right)^2}, \qquad (2.18)$$

where Δx, Δy, Δz are the grid intervals in the x-, y-, and z-directions, and Δ_1, Δ_2, Δ_3 are the distances to the interface from the x-, y-, and z-ghost nodes associated with the hybrid node, as shown in Fig. 2.5(b). In case that the hybrid node has only one or two neighboring ghost nodes, the corresponding irrelevant terms in Eq. (2.18) are set to zero. Note that if the local boundary is flat as seen locally, then α in Eq. (2.18) is always between zero and unity. In addition, it can be verified straightforwardly that α given by (2.17) and (2.18) satisfy the three principles listed earlier.

So far, we have provided the numerical description of the velocity for the ghost nodes, hybrid nodes, and the interior fluid nodes and thus have formulated a complete algebraic system for all the non-trivial nodes.

2.1.7 Pressure treatment at the hybrid nodes

Following the same spirit in the velocity treatment of the hybrid nodes, we now derive a mixed stencil for the pressure that consists of both the Poisson equation and an interpolation scheme. In Section 2.1.5, we have described how to compute the pressure at the ghost nodes by extrapolating the pressure field. Using a mixed stencil for the pressure at the hybrid nodes will allow smooth transition of the numerical description between the interpolation and the finite-difference discretization and will thus further improve the temporal accuracy.

Again, we use a 2D uniform grid to illustrate the pressure treatment. Re-write the discrete Poisson equation, Eq.(2.3), and express the pressure at the hybrid node as

$$p_{i,j} = \frac{1}{c_p}\left[L_P - \frac{\rho}{\Delta t}\left(\frac{U^*_{i+\frac{1}{2},j} - U^*_{i-\frac{1}{2},j}}{\Delta x} + \frac{V^*_{i,j+\frac{1}{2}} - V^*_{i,j-\frac{1}{2}}}{\Delta y}\right)\right], \tag{2.19}$$

where L_P represents the discrete Laplacian with the term involving the hybrid node value excluded, and c_p is the coefficient of $p_{i,j}$ in Eq. (2.3), i.e.,

$$
\begin{aligned}
L_p &= \frac{p_{i+1,j} + p_{i-1,j}}{\Delta x^2} + \frac{p_{i,j+1} + p_{i,j-1}}{\Delta y^2}, \\
c_p &= \frac{2}{\Delta x^2} + \frac{2}{\Delta y^2}.
\end{aligned}
\tag{2.20}
$$

The time level $n + 1$ in Eq.(2.3) has been dropped to simplify the notation.

The interpolation stencil for the hybrid-node pressure is based on the data points used for the velocity interpolation, i.e., the three vertices on the interpolation cube plus the BI point, as shown in Fig. 2.4(b). The bilinear polynomial, Eq. (2.5), is used as the interpolant, and its coefficients are obtained by requiring the polynomial give the desired pressure at the three vertex points and also the Neumann condition, $\partial p/\partial \mathbf{n}$, at the BI point. The interpolated pressure at the hybrid node can be written as

$$p_{i,j} = \sum_{m=1}^{3} \beta_m p_{(m)} + \beta_4 \left.\frac{\partial p}{\partial \mathbf{n}}\right|_{\mathrm{BI}}, \tag{2.21}$$

where $p_{(m)}$ is the pressure at the mth data point, and β_m, $j = m$ to 4, is the weight calculated from the interpolating polynomial. The inhomogeneous Neumann condition is obtained from $\partial p/\partial \mathbf{n} = -\rho(\mathrm{D}\mathbf{u}/\mathrm{D}t) \cdot \mathbf{n}$.

31

We now combine Eq. (2.19) and Eq. (2.21) and compute the pressure at the hybrid node according to

$$p_{i.j} = (1 - \alpha)\frac{1}{c_p}\left(L_P - \frac{\rho}{\Delta t}\textbf{d.i.v.}\right) + \alpha\left(\sum_{m=1}^{3}\beta_m p_{(m)} + \beta_4 \left.\frac{\partial p}{\partial \textbf{n}}\right|_{\text{BI}}\right), \qquad (2.22)$$

where **d.i.v.** represents the divergence term in Eq. (2.19), and α is the weight of the interpolation stencil and is given by Eq. (2.18). Thus, the pressure at the hybrid node is a combination of the solution to the Poisson equation and the interpolated value. In another perspective, The weighted pressure average can be viewed as the solution minimizing the following cost function

$$f(p) = (1 - \alpha)\left[p - \frac{1}{c_p}\left(L_P - \frac{\rho}{\Delta t}\textbf{d.i.v.}\right)\right]^2 + \alpha\left[p - \left(\sum_{m=1}^{3}\beta_m p_{(m)} + \beta_4 \left.\frac{\partial p}{\partial \textbf{n}}\right|_{\text{BI}}\right)\right]^2. \quad (2.23)$$

Note that since the pressure solution at a hybrid node given by Eq. (2.22) does not strictly satisfy Eq. (2.3). This introduces certain numerical error to the divergence-free constraint at the hybrid node after the velocity correction according to Eq. (2.4). However, the error is small because the interpolated solution is still a reasonable approximation of the local pressure, and in addition, the pressure will satisfy Eq. (2.3) more when the hybrid node moves away from the solid surface.

2.1.8   Summary of the solution process

The solution procedure for the entire domain is summarized as follows. At each time step, the position of the body is updated. The fluid nodes, solid nodes, ghost nodes, and

hybrid nodes are determined for the new geometry, and the corresponding stencils for the ghost nodes and hybrid nodes are calculated. The advection–diffusion equation, (2.2), is solved together with Eq. (2.7) and (2.15) in an iterative manner to obtain the intermediate velocity $\mathbf{u}^*$ for the entire field. Note that the nodes in the bulk region occupied by the solid body are irrelevant in the present formulation. In the iteration process, the face-center velocity is also updated. After convergence is reached for the velocity, the Poisson equation, (2.3), is solved together with Eqns. (2.8) and (2.22) iteratively to obtain the full pressure field. Finally, the velocity is updated according to Eq. (2.4) for all the fluid nodes including the hybrid nodes.

To calculate the total force on a solid surface such as lift or drag, the pressure and shear stress are integrated over all the surface elements, assuming that the stress distribution is uniform on each element. For each element, the closest ghost node is first identified, and then the pressure at the body-intercept of this ghost node is computed using a trilinear interpolation. To compute the shear stress at the body-intercept, the velocity at the image point in Eq. (2.7) is first obtained using the established interpolation scheme in Eq. (2.6). Then $\frac{\partial \mathbf{u}}{\partial \mathbf{n}}$ is approximated using the finite difference between the image point and the ghost node. Finally, the tangential stress τ_w is computed using the expression $\tau_w = \mu(\mathbf{I} - \mathbf{nn})\frac{\partial \mathbf{u}}{\partial \mathbf{n}}$. The algorithm for force integration has been tested using the exact solution of Stokes flow past a sphere.

2.1.9   Treatment for infinitesimally thin bodies

In biological locomotion problems of current interest, one often has to deal with thin bodies, e.g., wings and fins, whose thickness is much smaller compared to the characteristic length of the body. Such membranous bodies are often modeled as zero-thickness structures. The vanishing thickness in this case will cause the present method to fail, since a ghost node is also a fluid node at the same time. To avoid the problem, Mittal *et al.* (2008) employed auxiliary arrays to store the interpolated flow variables at the ghost node. In the present work, we circumvent the problem by introducing a uniform artificial thickness, h, along the membranous body. As shown in Fig. 2.6, the nodal points whose distance to the membrane is less than $h/2$ are defined as solid nodes, and the rest of the nodal points are fluid nodes. Once the "interior" and "exterior" regions are determined, the ghost and hybrid nodes can be easily identified in the same way as a regular body. To construct the interpolation and extrapolation stencils for the hybrid and ghost nodes, the body intercepts of the nodes with the inflated surface are needed. Without a mesh representation of the inflated surface, we compute the nearest point on the physical boundary for each hybrid or ghost node, and the point is defined as the true body intercept (BI) of the hybrid or ghost node. Then the pseudo BI point (BI') for a hybrid node is found by truncating $h/2$ off the line connecting the BI and the HN, and for a ghost node, BI' is found by extending the line from the BI to the GN to $h/2$ (Fig. 2.6). Since h is small, we assume that the boundary conditions at the BI are the same as those at the corresponding BI'. After extending the thickness, the membranous body can be treated in the same manner as a regular 3D body. In the present solver, h is typically chosen to be around three cells wide. Thus, the artificial thickness is
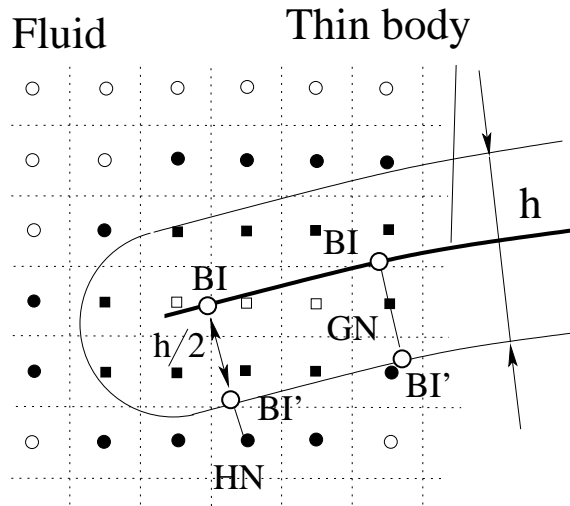
Figure 2.6: A 2D schematic showing the artificial thickness of a membrane-type structure, where HN and GN denote a hybrid node and ghost node, respectively.

automatically decreased as the grid is refined.

Since the numerical accuracy is mainly limited by the resolution of the flow field, the present thin-body treatment should not affect the numerical accuracy significantly compared to the zero-thickness representation. Note that the method in Mittal *et al.* (2008) can also be applied in the present solver. However, by storing the ghost-node flow variables together with the entire flow field, many domain-sweeping calculations such as a spatial derivative for the entire field can be done in a loop without the need to check whether any ghost node is required, thereby speeding up the computation. Moreover, the current method can deal with situations of thin bodies intersecting 3D bodies, e.g., the wing joints of insects, without further spacial treatment.

2.2   Structure solver

The structural solver is the FEM analysis tool for solid mechanics, NONSTAD (standing for nonlinear analysis of statics and dynamics), written by Prof. James F. Doyle at Purdue University. NONSTAD is one of the analysis modules in QED, a visual simulation tool developed by Prof. Doyle that encapsulates modeling, mesh generation, statics and dynamics analysis, and visualization. NONSTAD is designed specially for thin-walled structures such as frames, membranes, plates, and shells. The software has the capability of handling large displacements and large rotations, and it incorporates both elasticity and plasticity. In the flapping-wing MAV design, the wing structure often consists of light frames and plastic membranes (Ol *et al.*, 2008). Therefore, NONSTAD is particularly suitable in the analysis of those bio-mimetic structures.

For reinforced thin structures such as insect wings and fish fins, we approximate the spars with frames and the membranes with plates. For these structures, the local strain is assumed to be small so that the linear stress-strain relationship is used. However, since the structures may experience large-displacement and large-rotation deformations, geometric nonlinearity is thus incorporated in the formulation. Only 2D (for plates) or 1D (for frames) discretization is needed for these structural components. Their deformation under the resultant forces and moments on the cross sections can be derived using the classical theory of beams and plates. The mathematical formulations can be found in many textbooks of solid mechanics (Doyle, 2001).

For example, a 3D frame member has two nodes, and each node has six degrees of

freedom (DoF),

$$\{u\} = \{u_1, u_2, u_3, \phi_x, \phi_y, \phi_z\}, \qquad (2.24)$$

where u_i is the displacement and ϕ_i is the rotational angle. We use $\bar{u}_i$ to represent the displacement measured in the local coordinate system, (ξ, η, ζ), with ξ tangential to the frame. In the local coordinates, the frame member has three deformation behaviors. The first is a rod action with axial displacement $\{\bar{u}_1\}$ along the rod (ξ), and the corresponding force is $F = EA\frac{\partial \bar{u}_1}{\partial \xi}$. The second is two beam actions with bending deformations. The corresponding nodal DoFs in the $\xi\eta$ plane are the transverse displacement $\bar{u}_2$ and rotation ϕ_ζ (or the slope of the deflection curve at the node), and the bending moment is $M_\zeta = EI\frac{\partial^2 \bar{u}_2}{\partial \xi^2}$. The nodal DoFs in the $\xi\zeta$ plane are $\bar{u}_3$ and ϕ_η, and the bending moment is $M_\eta = EI\frac{\partial^2 \bar{u}_3}{\partial \xi^2}$. The third behavior is a twisting action about the frame axis, and the DoF and corresponding torque are ϕ_ξ and $M_\xi = GJ\frac{\partial \phi_\xi}{\partial \xi}$. Here EA, EI, and GJ are the axial, bending, and torsional stiffnesses, respectively.

A 3D plate element is a three-node triangular element which supports both in-plane (membrane) and out-of-plane (flexural) actions. We use $\bar{u}_i$ to represent the displacement measured in the local coordinate system, (ξ, η, ζ), with ζ normal to the plate. The DoF at each node for the in-plane behavior is $\{\bar{u}\} = \{\bar{u}_1, \bar{u}_2, \phi_\zeta\}$, and the element implementation is taken from Bergan & Felippa (1985). Note that the drilling action is included here since $\phi_\zeta = \frac{1}{2}(\frac{\partial \bar{u}_2}{\partial \xi} - \frac{\partial \bar{u}_1}{\partial \eta})$. The out-of-plane behavior of the plate element is represented by the DoF $\{u\} = \{u_3, \phi_\xi, \phi_\eta\}$ at each node, where ϕ_ξ and ϕ_η are rotational deflections. The element used is the Discrete Kirchhoff Triangular (DKT) element,

37

which has been widely researched and documented as being one of the more efficient flexural elements (Batoz *et al.*, 1980). In terms of the local coordinates, the in-plane behavior of the plate can be written as

$$
\begin{aligned}
N_{\xi\xi} &= \frac{Eh}{(1 - v_s^2)}\left[\frac{\partial \bar{u}_1}{\partial \xi} + v_s\frac{\partial \bar{u}_2}{\partial \eta}\right], \\
N_{\eta\eta} &= \frac{Eh}{(1 - v_s^2)}\left[\frac{\partial \bar{u}_2}{\partial \eta} + v_s\frac{\partial \bar{u}_1}{\partial \xi}\right], \\
N_{\xi\eta} &= \frac{Eh}{2(1 + v_s)}\left[\frac{\partial \bar{u}_1}{\partial \eta} + \frac{\partial \bar{u}_2}{\partial \xi}\right],
\end{aligned}
\tag{2.25}
$$

and the out-of-plane (flexural) behavior of the plate can be written as

$$
\begin{aligned}
M_{\xi\xi} &= \frac{EI}{(1 - v_s^2)}\left[\frac{\partial^2 \bar{u}_3}{\partial \xi^2} + v_s\frac{\partial^2 \bar{u}_3}{\partial \eta^2}\right], \\
M_{\eta\eta} &= \frac{EI}{(1 - v_s^2)}\left[\frac{\partial^2 \bar{u}_3}{\partial \eta^2} + v_s\frac{\partial^2 \bar{u}_3}{\partial \xi^2}\right], \\
M_{\xi\eta} &= \frac{EI}{(1 + v_s)}\frac{\partial^2 \bar{u}_3}{\partial \eta\partial \xi}.
\end{aligned}
\tag{2.26}
$$

In these expressions, h is the thickness of the plate, $I = h^3/12$ is the area moment of inertia of the cross section, $\bar{u}_i$ is again the displacement measured in the local coordinate system for which ξ and η are the two tangential coordinates, N_{ij} and M_{ij} are respectively the resultant forces and moments acting on the cross section.

The large-displacement and small-strain deformation in the structural solver is handled using the corotational scheme. That is, a local coordinate system is envisioned as moving with each discrete element, and, relative to this coordinate system, the element behaves linearly as described in previous paragraphs. Consequently, the nonlinearities of the problem are results of the coordinate transformation. The tangent stiffness of an

38

element, $[k_T]$, is the combination of the elastic stiffness and the geometric stiffness,

$$[k_T] = [k_E] + [k_G].$$ (2.27)

The dynamical system representing the structural vibration is obtained by assembling the equations for all the elements,

$$[M]\{\ddot{u}\} + [C]\{\dot{u}\} + [K]\{u\} = \{P\},$$ (2.28)

where $\{P\}$ is the external force vector incorporating the forces from the fluid in contact with the structure. The time stepping is achieved using the Newmark scheme.

The description of the FEM approach used in NONSTAD and the instruction of the software usage are provided in several publications (Doyle, 1991, 2001, 2008).

2.3 Flow–structure coupling

The incompressible Navier–Stokes equation is combined with the structural dynamics through the boundary conditions including the no-slip, no-penetration, and traction conditions. In the code implementation, the FEM code is coupled with the immersed-boundary flow solver, and the communications between the two codes are coordinated through the Message Passing Interface (MPI) library. With the MPI, the two solvers are running in parallel as independent processes on a computer, and only minimal modifications of the two existing stand-alone softwares are needed in order to couple them together.

39
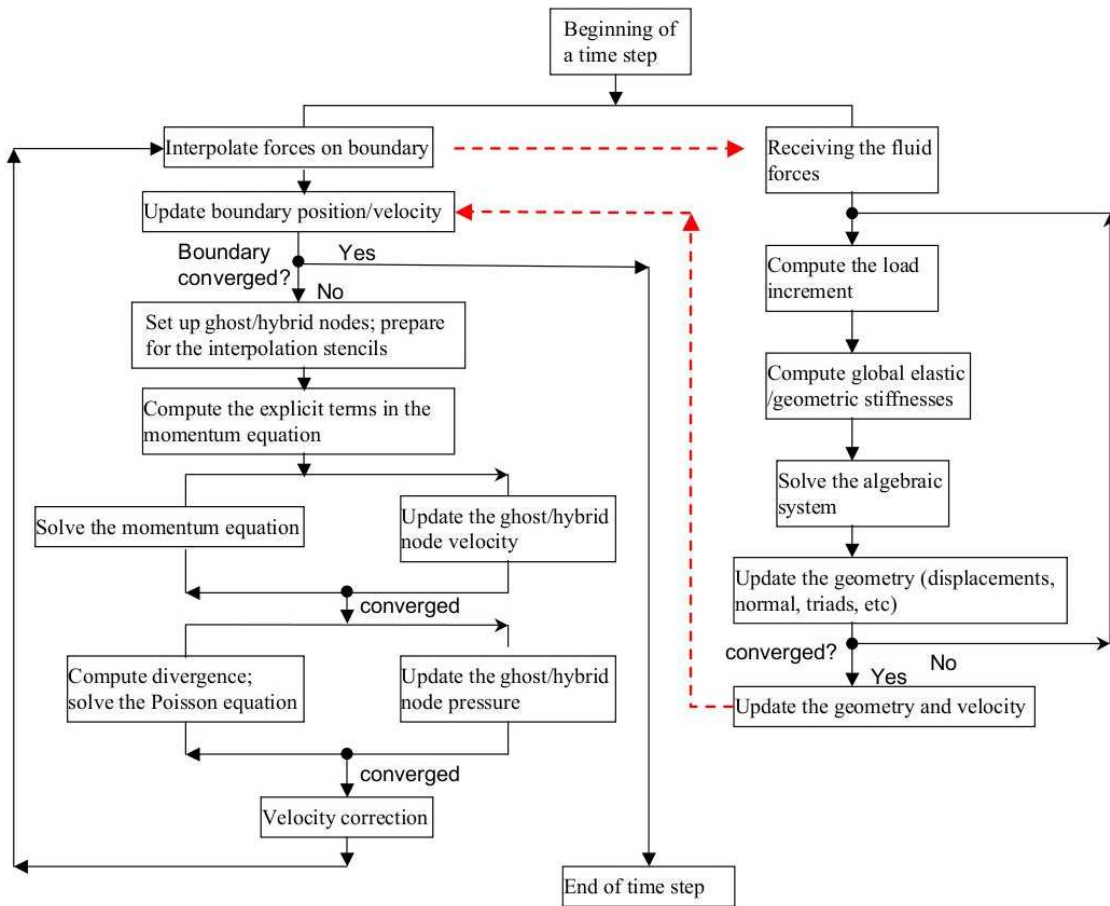
Figure 2.7: Flow chart of the flow–structure iteration during a complete time step. The left and right panels represent the flow and structural solvers, respectively, and the dashed lines represent the data transfer between the two solvers.

Furthermore, the flow solver and structural solver share the triangular mesh on the wetted surface of the solid, which makes the interpretation of the boundary displacement and surface force between the two solvers straightforward. To achieve the implicit coupling, the flow and structure are solved in an iterative manner. The algorithm for a complete time step is summarized by the flow chart in Fig. 2.7.

2.4   Code validation and demo cases

This section includes several simulations performed to validate current code and numerical algorithms and to demonstrate the capability as well. Problem descriptions and setups are given in details, and the results are compared with previous numerical or experimental studies.

2.4.1   Grid convergence study

The interpolation schemes adopted here for flow reconstruction near the immersed boundary, including both the ghost nodes and the hybrid nodes, have a second-order accuracy, which is consistent to the accuracy of the spatial discretization of the bulk field. The mixed reconstruction–differentiation approach at the hybrid nodes is expected to preserve the accuracy of the overall numerical method. The grid convergence test is performed using the flow past a circular cylinder. The Reynolds number $Re = Ud/\nu$ is 100 where d is the cylinder diameter, U is the free stream velocity. A small domain of $2d \times 2d$ is used here with the cylinder placed at the center of the domain. A zero normal derivative is applied for the velocity at the outer boundaries except the upstream side. In all simulations presented in this work, the homogeneous Neumann condition for the pressure is applied at the outer boundaries. Simulations are run on uniform grids with a series of resolutions, 40×40, 80×80, 160×160, 320×320, and 640×640. The cylinder surface is discretized so that the length of the surface segments is smaller than one third of the Cartesian cell size. A total number of 1000 time steps are run with the step size equal to $0.0001d/U$. The flow fields at the end of the simulations are used for
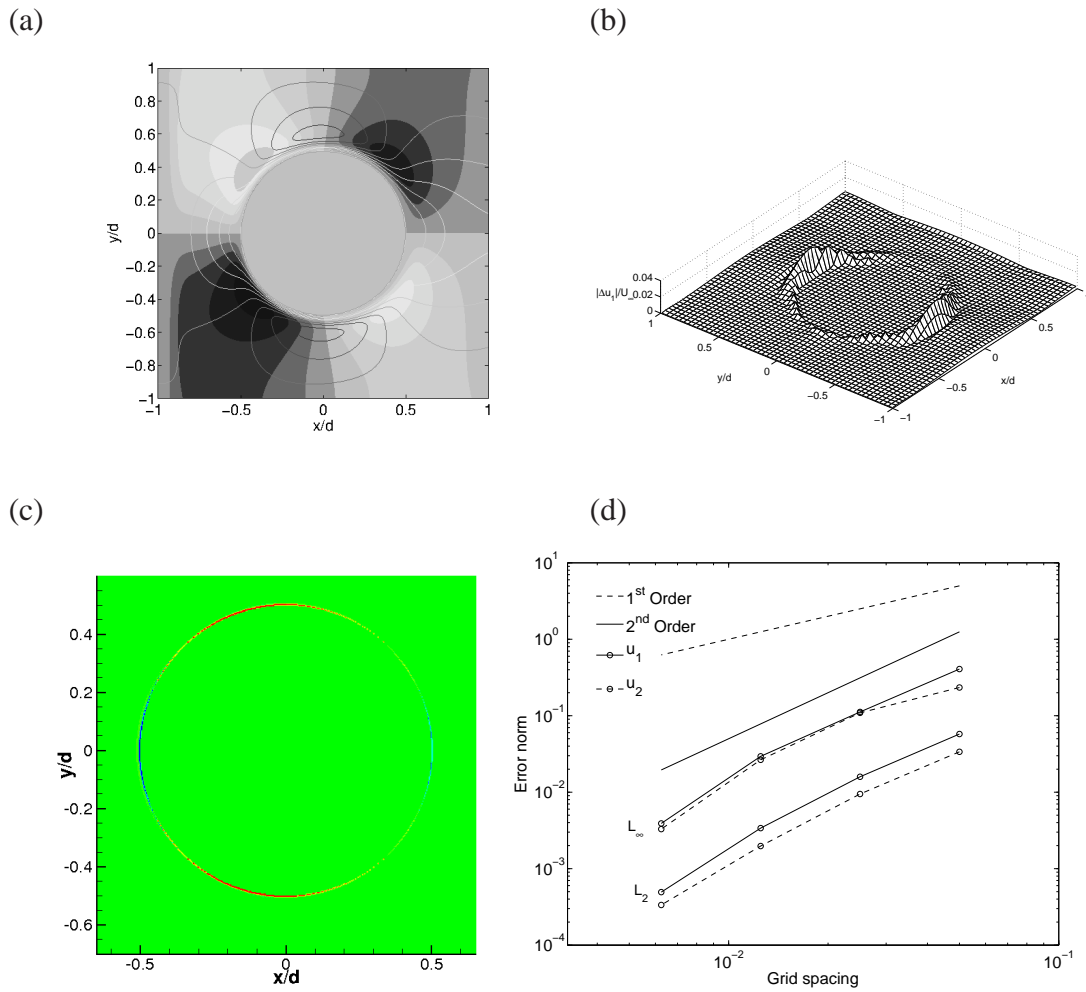
Figure 2.8: Grid convergence study using the problem of flow past a 2D stationary cylinder. (a) Contours of u_1 (lines) and u_2 (grey scale) for the solution using the 640×640 grid. (b) Distribution of the numerical error in the u_1 component from the 160×160 grid (only one every three mesh points in both x and y directions is shown). (c) Contours of the divergence. (d) L_2 and L_∞ error norms of the u_1 and u_2 velocities for different resolutions.

the study. To compute the error, we used the solution on the finest grid as the reference and compare the results from the other resolutions with this reference. Fig. 2.8(a) shows the contours of the two velocity components computed on the finest grid, and Fig. 2.8(b) shows the distribution of error magnitude in the u_1 velocity obtained on the 160×160 grid. The numerical error of the divergence field is plotted in Fig. 2.8(c). Note that the errors are concentrated in the region near the immersed boundary, which is a

typical phenomenon for the immersed-boundary methods in the literature (e.g., Yang & Balaras (2006); Mittal *et al.* (2008)).

The L_2 and L_∞ norms of the error for the velocity components are shown in Fig. 2.8(d) for the coarser grids. Both error norms confirm that the present numerical method has an overall second-order accuracy.

2.4.2   Flow past a stationary cylinder

The 2D flow past a stationary cylinder is computed to assess the fidelity of the present immersed-boundary solver. Here we run the simulations for $Re =$ 40, 100, 300 and 1000 on a 400×320 nonuniform grid, where $Re = Ud/\nu$ with U as the freestream velocity and d as the cylinder diameter. The domain size is $40d \times 50d$, and the grid near the cylinder is refined so that the smallest spacing is $\Delta x = \Delta y = 0.01d$. A zero normal derivative is applied for the velocity at the outer boundaries except the upstream side.

Fig. 2.9(a,b) shows the temporal variations of the drag and lift coefficients defined by $C_D = F_D/(\frac{1}{2}\rho U^2 d)$ and $C_L = F_L/(\frac{1}{2}\rho U^2 d)$, where F_D and F_L are the drag and lift on the cylinder per unit span. To promote flow instability and shorten the simulation time, small artificial disturbances are added to the flow initially to induce the asymmetry. When the flow reaches a stationary state marked by periodic vortex shedding behind the cylinder, the drag coefficient oscillates at a frequency twice of the frequency in the lift coefficient. Fig. 2.9(c) shows the vortex contours for $Re = 300$ in which the unsteady vortices in the wake of the cylinder are well captured.

Strouhal number is defined by $St = fd/U$ where f is the frequency of the lift coefficient and is equal to the vortex shedding frequency. The drag, lift, and the Strouhal number are tabulated
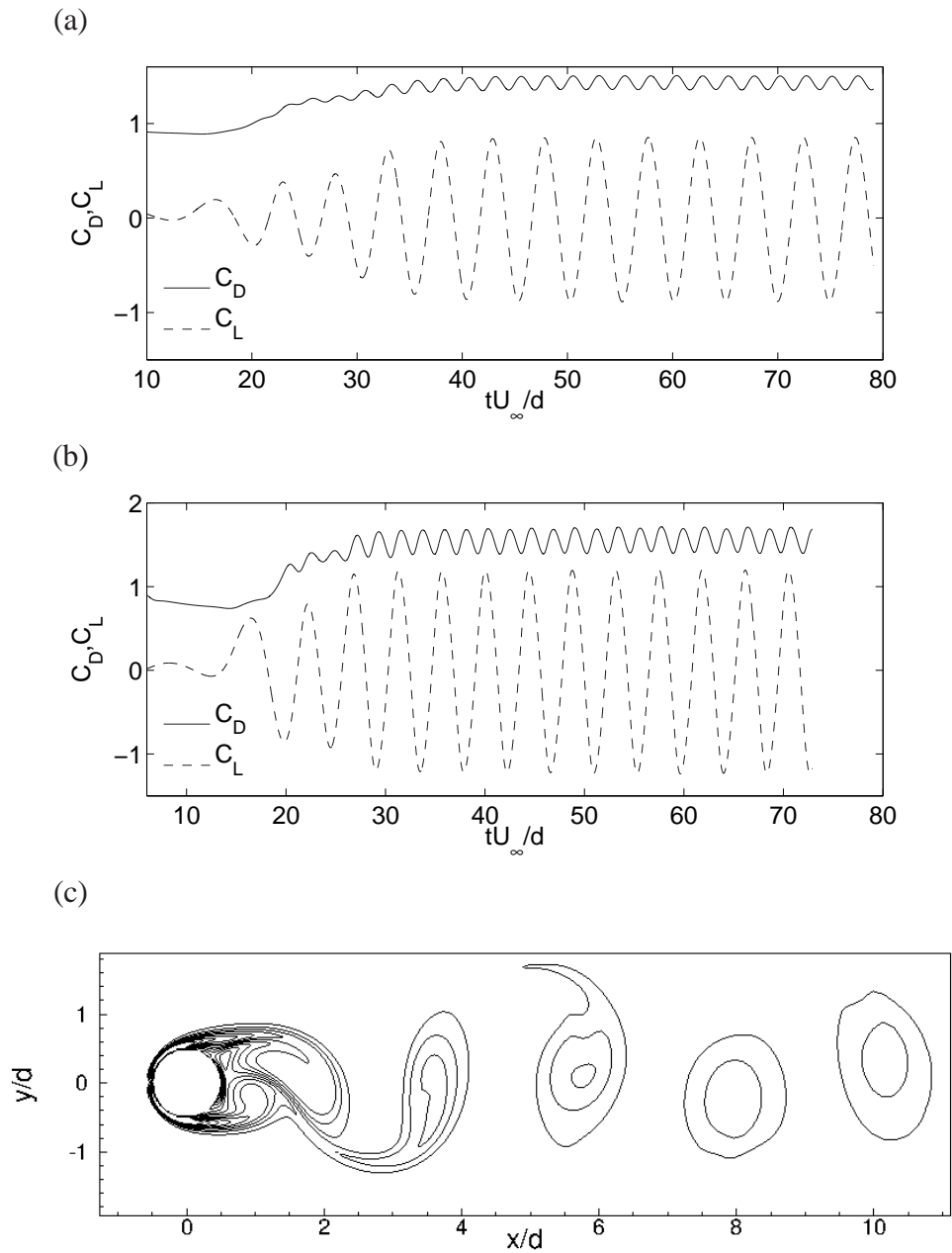
Figure 2.9: Flow past a 2D stationary cylinder. (a,b) Drag and lift coefficients for $Re = 300$ (a) and $Re = 1000$ (b). (c) Instantaneous contours of the spanwise vorticity for $Re = 300$.

in Table 2.1 for the Reynolds numbers considered here. The results from several sources are

also listed for comparison. Among the previous results, the data from Williamson (Williamson,

1992) was obtained from experiments, and the rest are from numerical simulations, including the

spectral-element method (Henderson, 1995) and the immersed-boundary method (Marella *et al.*,

Re	40		100		300		1000	
	C_D	St	C_D	St	C_D	St	C_D	St
Present	1.53	–	1.35	0.159	1.43	0.196	1.56	0.235
Mittal *et al.* (2008)	1.53	–	1.35	0.165	1.36	0.210	1.45	0.230
Henderson (1995)	1.54	–	1.35	–	1.37	–	1.51	–
Marella *et al.* (2005)	1.52	–	1.36	–	1.28	–	–	–
Williamson (1992)	–	–	–	0.157	–	0.203	–	0.206

Table 2.1: Laminar flow past a 2D stationary cylinder. Comparisons of the drag coefficient and Strouhal number with previous results.

2005; Mittal *et al.*, 2008). The comparison shows a very good agreement between our results and the previous data. Note that for $Re = 1000$, the flow in a real situation has become essentially three-dimensional, which explains the considerable difference in the Strouhal number between the experimental result and numerical data.

2.4.3   Flow past a sphere

Flow past a stationary sphere is a canonical problem that allows us to test the 3D implementation of the immersed-boundary treatment. The problem at low Reynolds numbers has been studied extensively using both experimental (Clift *et al.*, 1978; Ormieres & Provansal, 1999; Sakamoto & Haniu, 1995) and numerical approaches (Johnson & Patel, 1999; Mittal, 1999; Mittal *et al.*, 2002, 2008). Depending on the Reynolds number $Re = Ud/\nu$, the flow has three distinct regimes. Below $Re = 210$, the flow past a sphere is axisymmetric and steady (Natarajan & Acrivos, 1993). Between $Re = 210$ and around 280, the flow is steady but loses axisymmetry. Above $Re = 280$, the flow is neither steady nor axisymmetric.

In the present study we performed simulations of the flow with the Reynolds number ranging from 100 to 350. Both qualitative and quantitative comparisons were made with available results in the literature. For all Reynolds numbers studied, we employed a $192 \times 120 \times 120$ nonuniform grid with grid clustering around the sphere and in the near-field wake. The domain size used in

Table 2.2: Comparison of the current results for flow past a sphere with existing experimental and computational studies.

	$Re = 100$			$Re = 150$			$Re = 300$	$Re = 350$
	x_c/d	y_c/d	L_b/d	x_c/d	y_c/d	L_b/d	St	St
Mittal (1999)	-	-	0.87	-	-	-	-	0.14
Bagchi et al. (2001)	-	-	0.87	-	-	-	-	0.135
Johnson & Patel (1999)	0.75	0.29	0.88	0.82	0.29	1.2	0.137	-
Taneda (1956)	0.745	0.28	0.8	0.82	0.29	1.2	-	-
Marella et al. (2005)	-	-	0.88	-	-	1.19	0.133	-
Mittal et al. (2008)	0.742	0.278	0.84	0.81	0.3	1.17	0.135	0.142
Present results	0.762	0.298	0.913	0.830	0.338	1.229	0.125	0.152

all the simulations is $16d \times 15d \times 15d$. These parameters were chosen so that a direct comparison could be made with the results in Mittal et al. (2008). A zero normal derivative is applied for the velocity at the outer boundaries except the upstream side.

For $Re = 100$ and 150, the computed flow is steady and axisymmetric. Therefore, the center coordinates (x_c, y_c) of the flow recirculation bubbles in the wake of the sphere can be accurately determined. The length of the recirculation zones, defined as the distance from the back of the sphere to the farthest point in the streamwise direction, denoted by L_b, can also be calculated. The values of these variables for $Re = 100$ and 150 are compared with previous studies in Table 2.2 and are found to be in excellent agreement with those studies.

For $Re = 300$ and 350, the flow is strongly unsteady. It is well established that for this Reynolds number regime the wake is dominated by vortex loops that are interlocked together (Sakamoto & Haniu, 1995; Ormieres & Provansal, 1999; Mittal, 1999). The 3D vortex features were well captured in our simulations. Here we present the Strouhal number, St, which represents the nondimensional frequency of the vortex shedding from the sphere. Note that the simulations were run for long enough time so that a stationary state was reached during which the statistical quantities such as the Strouhal number and force coefficients were taken. The computed Strouhal number is tabulated in Table 2.2 and shows good agreement with previous studies. In Fig. 2.10, a comparison is made between the computed mean drag coefficient from
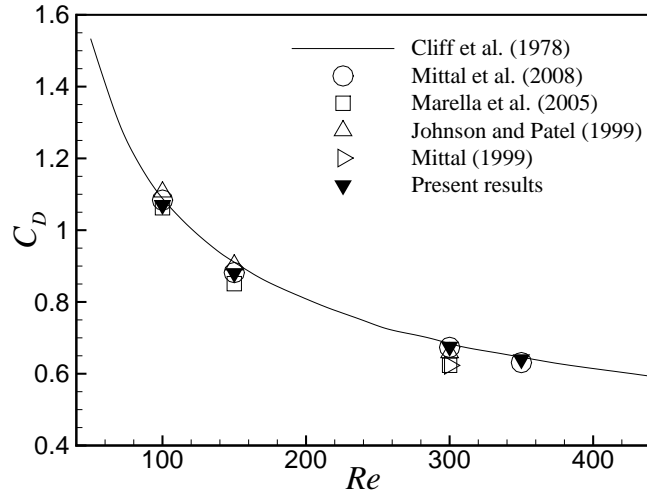
Figure 2.10: Comparison of the computed mean drag coefficient with experimental and numerical data. The solid line is the correlation data from Clift *et al.* (1978).

the present simulations and the results from a number of previous experimental and numerical studies. The current result is once again in excellent agreement with those results.

2.4.4   Flow past an in-line oscillating cylinder

After successfully validated the present formulation for stationary-boundary problems, we proceed to perform numerical tests for moving boundaries. The first problem we consider is a cylinder of diameter d oscillating in a channel flow as shown Fig. 2.11. The channel has the dimension of $4d \times 4d$, and the inlet velocity has a parabolic profile with the maximum value U. The no-slip and no-penetration conditions are applied at the channel walls, and a zero normal derivative is applied for the outlet. Although the channel is too short to exclude the effect of the exit, the channel length does not affect the numerical oscillation related to the moving boundary. The cylinder oscillates symmetrically along the centerline of the channel, and its prescribed velocity is given by $u_c \sin(2\pi f t)$, where u_c is the maximum translational velocity and f is the frequency. We set $u_c/U = 0.1\pi$ and $fd/U = 0.2$ so that the stroke distance of the cylinder is $0.5d$. The Reynolds number in the test is $Re = Ud/\nu = 100$. A uniform grid of either

47
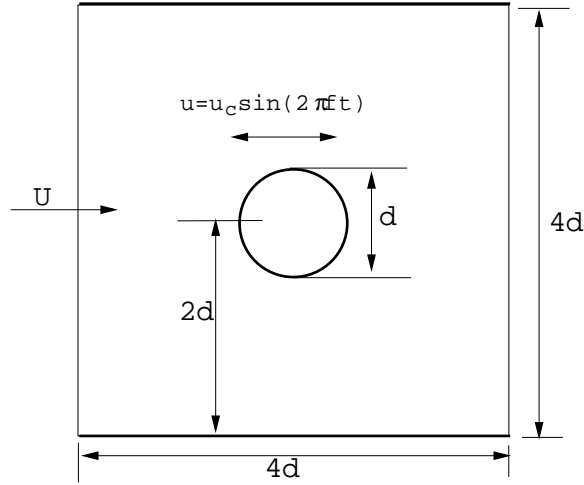
Figure 2.11: Schematic of an in-line oscillating cylinder in a channel.

64×64 or 128×128 points is used to discretize the domain. In addition, three different time steps, $\Delta t U/d = 0.005$, 0.01, and 0.02, are used to study the effect of Δt.

To show the effect of the current formulation on the force oscillation, we also performed the simulations without the mixed stencil at the hybrid nodes. In those simulations, we simply set the weight of the interpolation stencil, $\alpha = 1$, in Eqns. (2.15) and (2.22). That is, the flow variables at the hybrid nodes are obtained completely from interpolation. To facilitate the discussion, here we refer to the second approach as the "reconstruction-only" method.

Figure 2.12 shows the drag history of the cylinder, normalized by $\frac{1}{2}\rho U^2$, for several combinations of the spatial and temporal resolutions. In Fig. 2.12(a) where the the reconstruction-only method is used with 64×64 points and $\Delta t U/d = 0.01$, the drag displays substantial oscillations. On the other hand, the drag in Fig. 2.12(b), which is computed using the present hybrid formulation with the same simulation set up, contains only moderate fluctuations. In these two tests, the maximum CFL number, defined as $\Delta t(u_1/\Delta x + u_2/\Delta y)$, is around 0.35.

In the next set of simulations, the 128×128 grid is employed, and the maximum CFL is kept at 0.35, i.e., the time step is $\Delta t U/d = 0.005$. The drag histories are shown in Figs. 2.12(c) and (d), respectively, for the reconstruction-only method and the hybrid method. It can be seen that

(a)   (b)

(c)   (d)

(e)   (f)

(g)   (h)
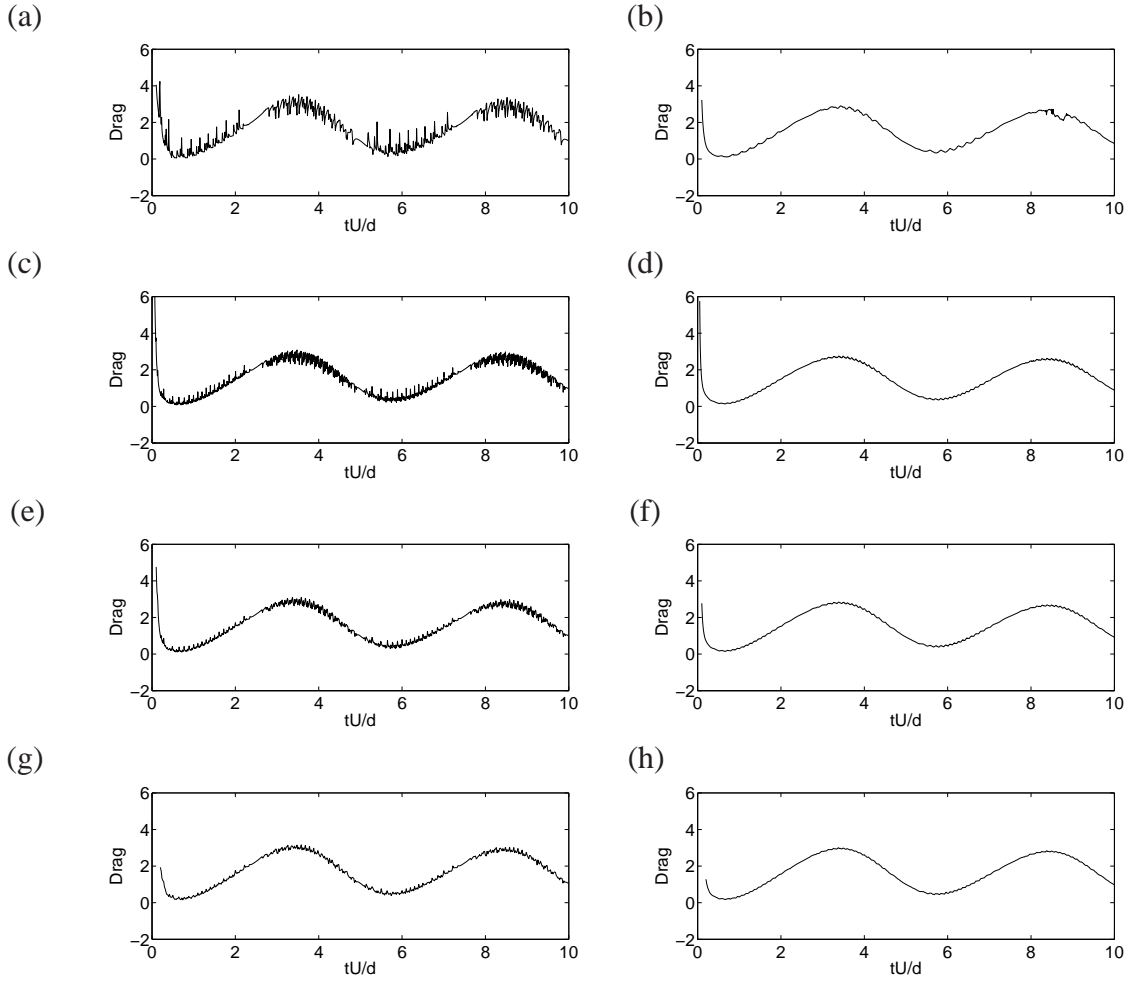
Figure 2.12: The normalized drag of an in-line oscillating cylinder in a 2D channel. Left: the reconstruction-only immersed-boundary formulation; right: the present hybrid formulation. The resolution is 64×64 in (a) and (b), and 128×128 in the other panels, and the maximum CFL in the four rows is 0.35, 0.35, 0.7, and 1.4, respectively.

the magnitude of the numerical oscillation is reduced in (c) due to the grid refinement but is still significant. In comparison, the hybrid method only produces slight high-frequency fluctuations.

Then we use the 128×128 grid and increase the time-step size so that the maximum CFL is either 0.7 or 1.4 (i.e., $\Delta tU/d = 0.01$ or 0.02). The results are shown in Fig. 2.12(e) to (h) for both immersed-boundary formulations. For the reconstruction-only method, the magnitude of the oscillation is reduced proportionally as Δt is increased, as seen in Figs. 2.12(c,e,g). The observation is consistent to the qualitative analysis in Section 2.2. For the hybrid method,

49
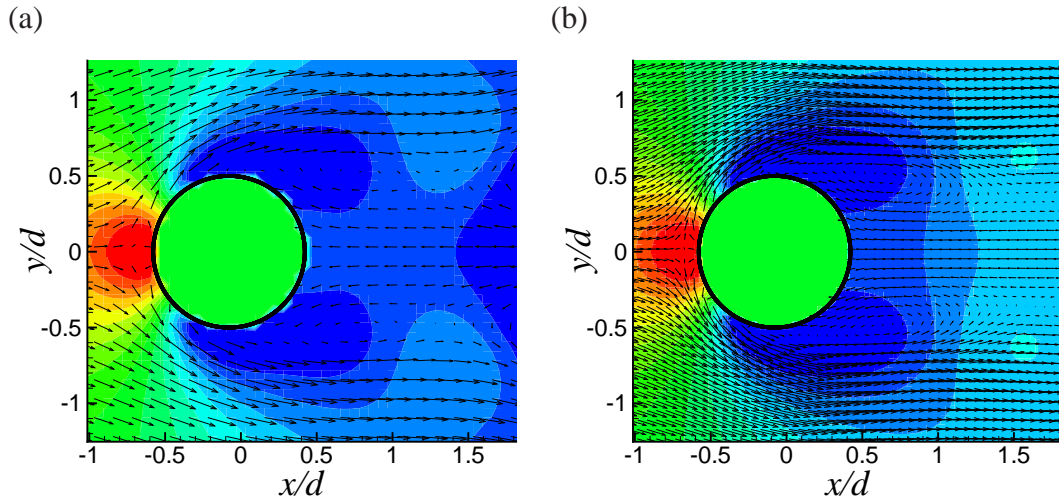
Figure 2.13: The velocity field and pressure contours at $tU/d = 9$ for an in-line oscillating cylinder in a channel using the (a) 64×64 and (b) 128×128 grid.

Figs. 2.12(d,f,h) show that the numerical oscillation in the drag is suppressed for these time-step sizes and there is no significant error. Slight oscillations are still visible because different interpolation stencils are involved when the boundary moves across the grid.

The flow field for the hybrid formulation is shown in Fig. 2.13 for the two resolutions at $tU/d = 9$. For the 64×64 grid, there are only 16 points across the cylinder, and thus the flow around the immersed boundary is barely resolved. Nevertheless, the corresponding velocity field in Fig. 2.13(a) is reasonably accurate. In Fig. 2.13(b) where the finer resolution is used, the flow field around the cylinder is captured with a much better accuracy.

In order to evaluate the effect of the Strouhal number, we varied the translational frequency of the cylinder but kept the stroke distance the same. In addition, we studied the effect of the characteristic flow around the solid body by moving the cylinder in the transverse direction. In both studies, the performances of the present reconstruction-only method and the hybrid method are not affected significantly. In conclusion, the hybrid method presented here is effective in suppressing the numerical oscillation caused by the moving boundaries.
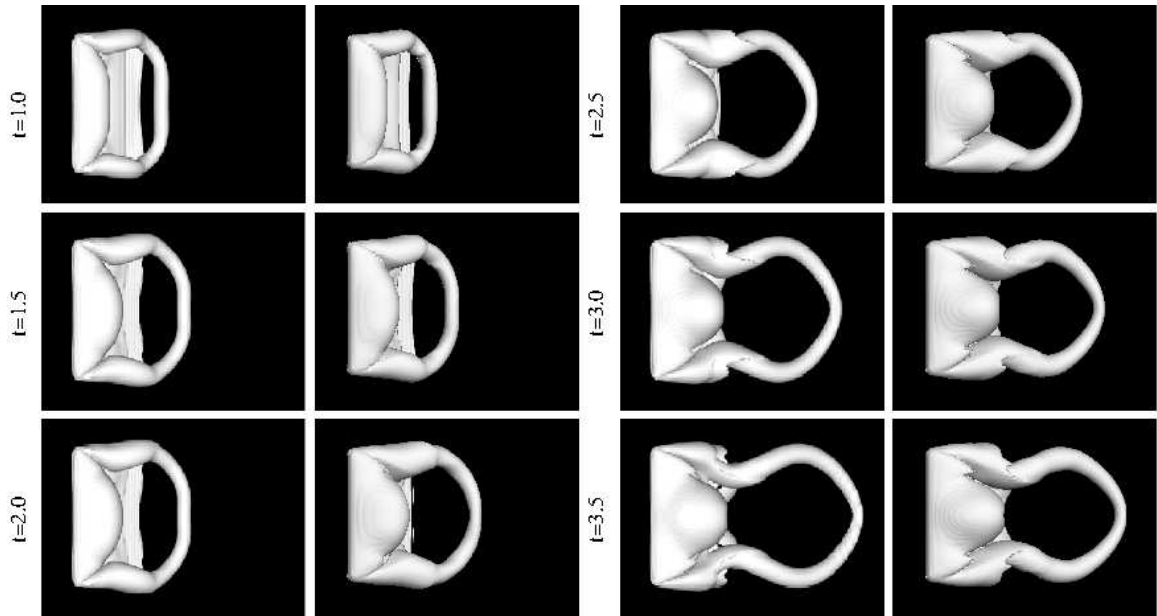
Figure 2.14: Top view of wake development behind a stationary rectangular plate at an angle of attack of 40°. The 1st and 3rd columns are from Taira & Colonius (2009), and the 2nd and 4th columns from the current simulation. The time is normalized by c/U.

2.4.5 A suddenly started plate

This problem concerns an impulsive flow over a rigid rectangular plate, which was studied numerically by Taira & Colonius (2009). The stationary plate has a rectangular shape and has an aspect ratio of 2. The angle of attack of the plate is fixed at 40°, and the Reynolds number based on the freestream velocity U and the chord length c is $Re = 500$. The 3D simulation is done in a $10c \times 10c \times 6c$ (in the streamwise, transverse, and spanwise directions) domain and on a $211 \times 121 \times 141$ grid. In figure 2.14 we present the wake development by showing the isosurface of the vorticity magnitude equal to $5U/c$ at different time instants in a top view. The corresponding flow field from Taira & Colonius (2009) is shown for comparison. It can be seen that the instantaneous vortex structures from the two simulations agree with each other very well.
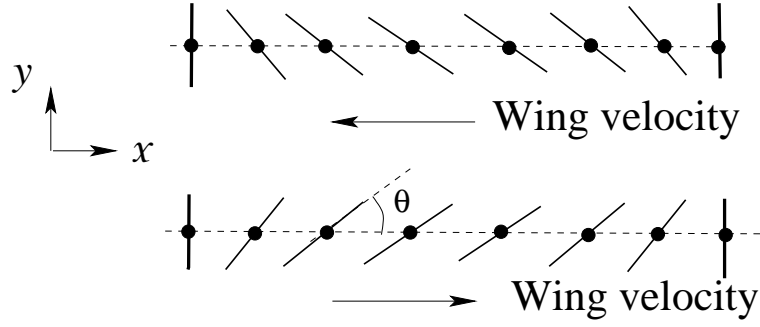
Figure 2.15: Schematic of a 2D hovering wing showing the forward and backward strokes.

2.4.6   Flow induced by a 2D hovering wing

In this moving-boundary test, we consider a rigid plate of infinite span undergoing combined oscillatory translation and rotation as shown in Fig. 2.15. This configuration has been extensively used for modeling the hovering flight in animals such as insects (Wang *et al.*, 2004; Eldredge, 2007), where the plate represents a slice of the wing. The kinematics of the wing section is described by a sinusoidal translation and a rotation around the wing center according to the following equations

$$x_0(t) \quad = \quad \frac{A}{2}\cos(2\pi ft) \tag{2.29}$$

$$\theta(t) \quad = \quad \frac{\pi}{2} + \theta_m \sin(2\pi ft + \phi) \tag{2.30}$$

where $x_0(t)$ is the stroke position, $\theta(t)$ is the angle between the wing and the horizontal axis (measured in the counterclockwise direction), A is the stroke distance of the wing, θ_m is the angle amplitude, f is the flapping frequency, and ϕ is the phase difference between the wing translation and rotation. The vanishing phase lag, $\phi = 0$, is studied here.

The simulation is performed in a rectangular domain of size $20c \times 20c$, where c is the chord length of the wing section, and 320×256 nonuniformly distributed grid points are used. Around
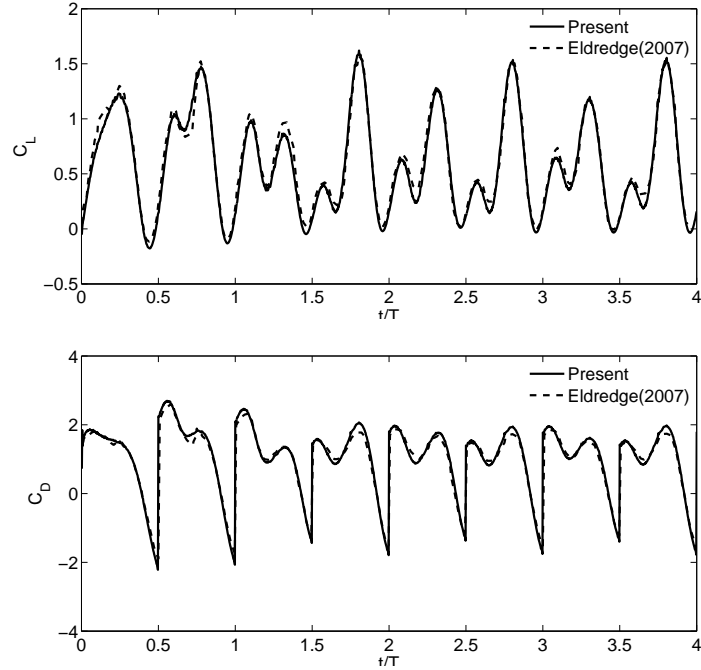
Figure 2.16: The drag and lift coefficients of a 2D hovering wing.

the wing, the grid spacing is around $0.023c$. The kinematic parameters are $A/c = 2.8$, $\theta_m = \pi/4$.

The Reynolds number defined as $Re = U_{\max}c/\nu$ is 75, where $U_{\max} = \pi A f$ is the maximum

translational velocity of the wing. One complete cycle is resolved by 400 time steps. The

instantaneous drag and lift coefficients are defined as

$$
C_D = \frac{\text{sign}(\dot{x}_0(t))F_D}{\frac{1}{2}\rho U_{\max}^2 c}, \qquad C_L = \frac{F_L}{\frac{1}{2}\rho U_{\max}^2 c}, \tag{2.31}
$$

where F_D and F_L are total instantaneous horizontal and vertical forces, respectively. Previous

results of this problem obtained using a vortex particle method by Eldredge (2007) are com-

pared. The coefficients are plotted in Fig. 2.16 where the first four flapping cycles are shown.

The flow is initially quiescent and approaches a nearly periodic state after two cycles.

An ellipsis-shaped wing with the aspect ratio of 10 was used by Eldredge (2007). In our

case, the cross section is uniform except at the two rounded wing edges due to the approach of

introducing an artificial thickness. In the present simulation, the wing thickness is about 7% of the chord length. Despite the differences in the wing geometry, both the drag and lift coefficients in the two simulations exhibit only slight discrepancy. In both the forward and backward strokes, C_L contains two peaks, one after the stroke reversal and the other approximately at the midway of the stroke when the wing has the maximum translational velocity. The first peak can be explained by the wake capture mechanism where the wing interacts with the leading-edge vortex generated prior to the stroke reversal (Wang *et al.*, 2004). The drag, defined to always point against the wing translation, also contains two peaks in each half stroke, which take place prior to and shortly after the wing reversal due to the large angle of attack at the moment. The drag becomes negative during the reversal. These features are well captured in the present simulation and the force history shows no significant oscillation, which shows the effectiveness of the present immersed-boundary method.

2.4.7   Simulating a robotic fruit fly

This is a three dimensional moving-boundary problem. We simulate the flow around two robotic fruit fly wings, replicating the experiment in Dickinson *et al.* (1999). The wings are models of *Drosophila melanogaster* and have a span of $R = 0.25$ m. The area of each wing is $S = 0.0167$ m^2 and the average chord is $\bar{c} = 8.79$ cm. The wing shape used is similar to the one reproduced in Bai *et al.* (2009). In the experiment of Dickinson *et al.* (1999), one flapping period is composed of two half-strokes and the flapping frequency is $f = 0.145$ Hz. The wings sweep in the horizontal plane and rotate at the end of each stroke. The wing rotation occurs symmetrically with respect to the stroke reversal and lasts 16% of the flapping period. The stroke amplitude is 160°, and the angle of attack at mid-stroke is 40°. The Reynolds number is $Re = U\bar{c}/\nu = 164$, where $U = 0.215$ m/s is the mean translational velocity at the wing tip and $\nu = 115$ cSt is the
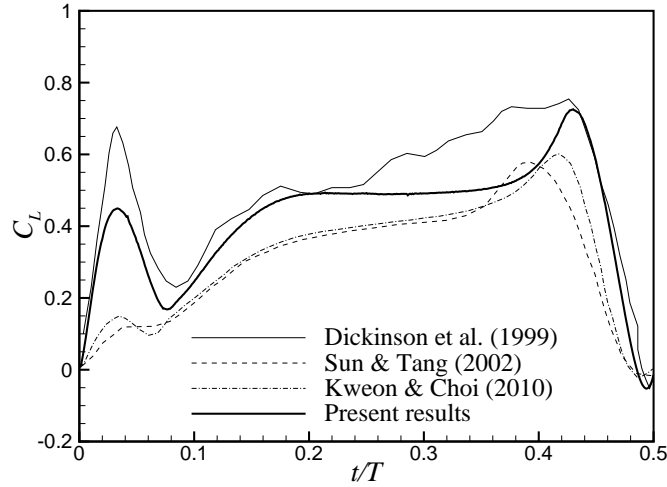
Figure 2.17: Instantaneous lift coefficient for a robotic fly.

kinematic viscosity of the fluid. The total lift force F_L is defined in the direction perpendicular to the stroke plane, and the total lift coefficient is defined as $C_L = 2F_L/(\rho U^2 S)$.

A nonuniform grid of $251 \times 251 \times 181$ is used. The size of the computational domain is equivalent to that of the oil tank in the experiment. Dirichlet boundary conditions for the velocity are imposed on the side walls, and open boundary conditions are imposed on the top and bottom boundaries. The simulation is conducted for five flapping cycles. The temporal variation of the lift coefficient during each stroke is virtually identical after the third cycle. Figure 2.17 shows the time history of the lift coefficient from the 4th cycle for the case with symmetrical rotation, together with the experimental (Dickinson *et al.*, 1999) and two numerical results (Sun & Tang, 2002*b*; Kweon & Choi, 2010). As we can see, our simulation captures the two lift peaks produced near the beginning and end of the half-stroke. Furthermore, our result compares better with the experimental data than the other two numerical results. It should be stressed that the numerical results from Sun & Tang (2002*b*) and Kweon & Choi (2010) were obtained from simulations of only one single wing, while both the current simulation and the experiment have a pair of wings.
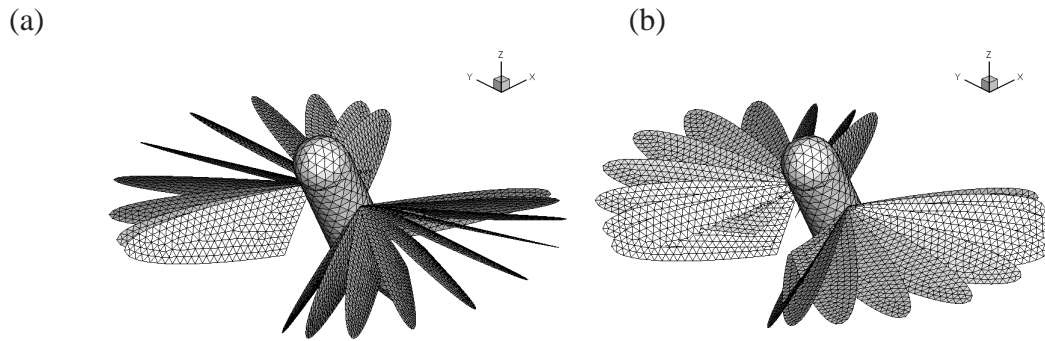
Figure 2.18: The 3D geometry and hovering kinematics of the hummingbird model. (a) Downstroke (forward stroke) and (b) upstroke (backward stroke). The leading edge of the wing sweeps in a horizontal (*xy*) plane.

2.4.8 Simulating a hummingbird

In the last case study, we consider aerodynamics of the hummingbird hovering flight. The simplified hummingbird body and wing anatomy is based on images of a Rufous Hummingbird (*Selasphorus rufus*). Each wing is represented here by a half ellipsis with an aspect ratio of 3:1. The shoulder corner of the wing is used as the pivot point. The surface mesh for the hummingbird model consists of 814 triangular elements for the body and 372 triangular elements for each wing.

The size of the computational domain is $17.5c \times 19c \times 14c$, where c is the chord length equal to the length of the short axis of the ellipsis. A 300×360×160 nonuniform grid is used, which provides clustered points around the hummingbird body and wings. The detailed kinematics of the Rufous Hummingbird are available in Tobalske *et al.* (2007). In the present simulation, a simple representation of the wing kinematics was chosen, as shown in Fig. 2.18. The leading edge, defined as the line through the pivot point and lying in the wing surface, rotates sinusoidally in the stroke plane with an amplitude of 112°, and meanwhile each wing surface rotates sinusoidally around the leading edge with an amplitude of 134° and a 10° delay with respect to the flapping angle. The distribution of the angle of attack of the wing is asymmetric: the

56

minimum angle is 27° during the downstroke and 19° during the upstroke. Here the angle of attack is defined as the acute angle between the wing surface and the stroke plane. The Reynolds number, $Re = \overline{U}_{\text{tip}}c/\nu$, is 1570, where $\overline{U}_{\text{tip}}$ is the average wing-tip velocity. Equivalently, the Reynolds number is 2465 in terms of the maximum wing-tip velocity. Note that the Reynolds number of the real hummingbird may be above 5000 (Altshuler *et al.*, 2004). A lower *Re* is used here to reduce the computational load that would be required for direct numerical simulation of the turbulent flow.

Figure 2.19 shows the flow structures generated by the hummingbird model at three different stages during downstroke. In the simulation, $t = 0$ is the beginning of downstroke. The figure shows the isosurfaces of Λ, the maximum imaginary part of the three complex eigenvalues of the velocity gradient tensor (Soria & Cantwell, 1994). Both the 3D view and the top view of the flow field are shown. Figures 2.19(a) and (d) shows the early stage of downstroke, where the leading-edge vortex (Ellington *et al.*, 1996) on the top surface of the wings is being formed. As the wings accelerate downward, depicted in Figs. 2.19(b) and (e), the leading-edge vortex remains attached to the wing surface. At the same time, a trailing-edge vortex is being shed and its outboard portion is merging with the tip vortex. As the wings decelerate and the angle of attack increases at the end of downstroke, a large region of separated flow is generated behind each wing and near the wing tip, as depicted in Figs. 2.19(c) and (f). Throughout the flapping cycle, the flow is dominated by small-scale, randomly oriented vortex filaments, which illustrates the complexity of the flow behavior even at the moderate Reynolds number.

Figure 2.20 shows the time-varying force coefficients averaged between the two wings during first three flapping cycles. The force coefficients, C_x, C_y, and C_z, are defined as the force components on a single wing normalized by $0.5\rho\overline{U}_{\text{tip}}^2c^2$. The lift coefficient, C_z, is characterized by a large peak during each half stroke, which roughly occurs during the mid-stroke when the
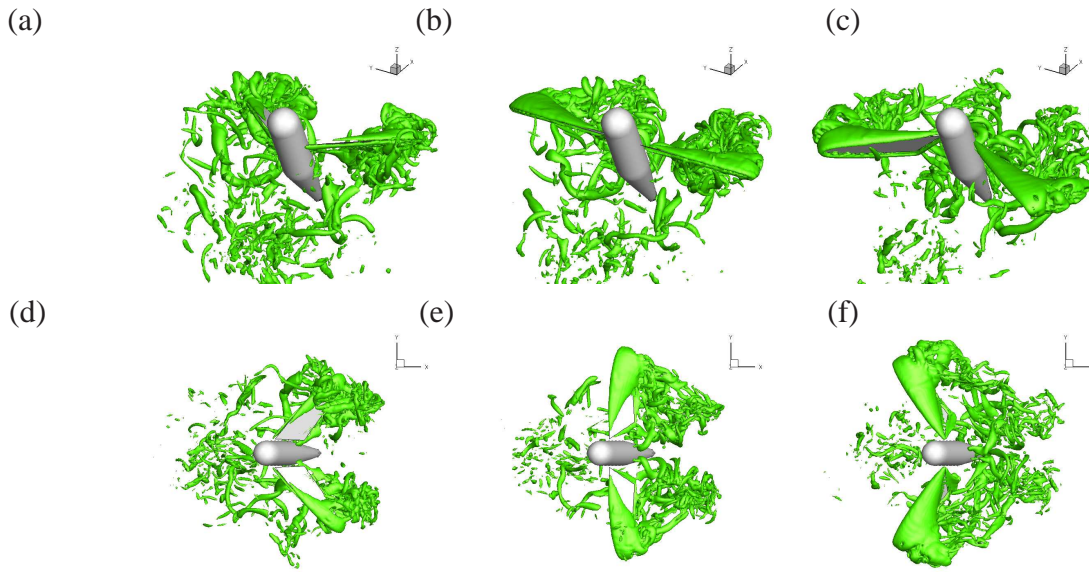
Figure 2.19: Vortex structures at three stages in downstroke of a modeled hummingbird in hovering flight. The time stamp is $t = 3.2T$ for (a,d), $3.3T$ for (b,e), and $3.4T$ for (c,f), where T is the period of a full flapping cycle.

wings undergo the maximum flapping velocity. The drag coefficient, C_x, during downstroke is comparable to C_z, but its peak is slightly delayed. During upstroke, C_x has a reverse sign and is significantly lower in magnitude compared to downstroke. The lateral force, C_y, is nearly zero since the two wings flap symmetrically and the y-forces cancel each other. In the present setup, the stroke plane is parallel to the horizontal plane, and thus the lift coefficient during upstroke is close to that during downstroke. In Tobalske *et al.* (2007), the stroke plane angle is around $\beta = 15°$ when the hummingbird is hovering. To incorporate this effect, we may simply transform the coordinate system and re-compute the lift coefficient according to $C_L = C_z \cos \beta + C_x \sin \beta$. The result is also plotted in Fig. 2.20, which shows that the lift during upstroke is significantly lower than that during downstroke. This is in line with the result from Warrick *et al.* (2009), who performed a particle image velocimetry (PIV) study of the hummingbird flight. In their experiment, the average circulation around the wing during downstroke is about twice of the average circulation during upstroke, which indicates a higher lift during downstroke.
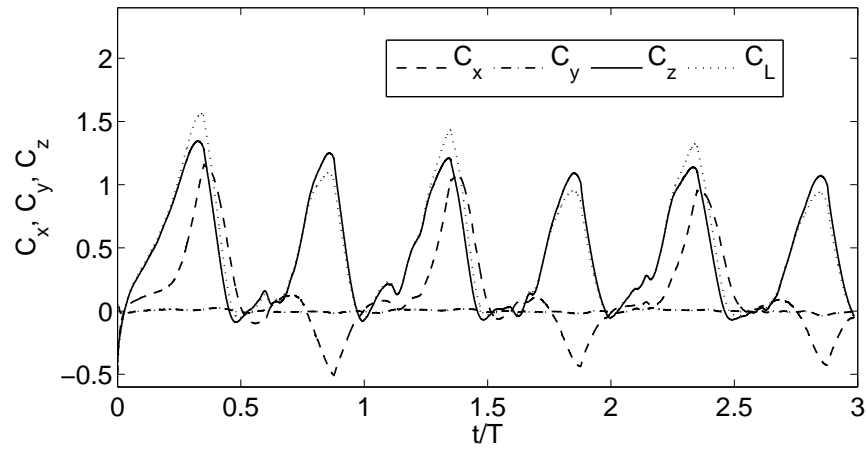
Figure 2.20: Time histories of the normalized force components, C_x, C_y, C_z during the first three flapping cycles. The simulation starts from the beginning of the downstroke. C_L is the lift coefficient when the stroke plane is tilted forward by 15°.

CHAPTER III

HYDRODYNAMIC PERFORMANCE OF A FLEXIBLE LOW-ASPECT-RATIO

PITCHING PLATE

3.1   Background

A pitching/heaving foil in an incoming flow is a reasonable approximation of the caudal fin of a fish and can be used to study the thrust production. Substantial work has been done on the hydrodynamics of rigid foils. Early experimental studies of a foil in a steady stream were done by Koochesfahani (1989); Triantafyllou *et al.* (1991, 1993); Anderson *et al.* (1998). The averaged wake behind the foil was found to be like a jet flow, and vortices closely resemble the von Kármán vortex street behind bluff objects but have reversed rotation. In addition, the thrust efficiency is largely dependent on the Strouhal number. A review of these work can be found in Triantafyllou *et al.* (2004). More recently, (Schnipper *et al.*, 2009) investigated the effect of the oscillation frequency and amplitude on the wake structures produced by a pitching foil in a soap film flow. Buchholz & Smits (2006, 2008) studied a rigid panel of low $\mathcal{AR}$ pitching around its leading edge in a free stream. They found that the thrust coefficient depends on both the Strouhal number and the aspect ratio and that the propulsive efficiency is sensitive to the aspect ratio when the span-to-chord ratio is less than 0.83. Dong *et al.* (2006) numerically studied a pitching/heaving foil of elliptic shape and investigated the three-dimensional topology of the wake.

In comparison to rigid foils, existing studies on flexible foils are mainly limited to foils of large span-to-chord ratios and two-dimensional flows. For example, Heathcote *et al.* (2004);

Heathcote & Gursul (2007*b*) investigated the effect of chordwise deformation on thrust generation and power consumption of an elastic foil in water tank. Moderate flexibility was found to increase the thrust efficiency compared to the rigid foil and an optimal flexibility may exist for given heaving frequency and amplitude. Zhu (2007) assumed an inviscid flow and utilized a boundary-element method to study the problem. In the inertia-driven case, he found that the chordwise flexibility reduces both the thrust and the propulsion efficiency; in the fluid-driven case, the chordwise flexibility increases the efficiency, which is consistent to the experiment result in Heathcote & Gursul (2007*b*). In another work, Michelin & Llewellyn Smith (2009) studied the effect of structural resonance on the thrust performance of a heaving foil. More recently, Ferreira de Sousa & Allen (2011) performed a two-dimensional viscous flow simulation of a pitching plate and obtained similar conclusion as the previous research.

For insects and fish, the span-to-chord ratio of their wings and fins is typically less than 10 (Dong *et al.*, 2006). Thus, the wake of the biological propulsors is highly three-dimensional. Currently it is still not clear how the structural deformation will affect the 3D vortices in the wake and how the result has to do with the performance of the propulsor. A computational study that addresses the fluid–structure interaction and resolves the 3D flow pattern will help answer these questions.

In this chapter, we consider a flexible plate of low aspect ratio pitching around its own leading edge in a free stream. The three-dimensional fluid–structure interaction is simulated. We systematically vary the pitching amplitude, frequency, as well as the rigidity of the plate and investigate the thrust and power efficiency. The effect of the elasticity on the performance of the propulsor and the vortex structures in the wake will be discussed. The problem is formulated in §3.2, a grid study is given in §3.3, the results and discussions are provided in §3.4 to §3.6; final conclusion is given in §3.7.
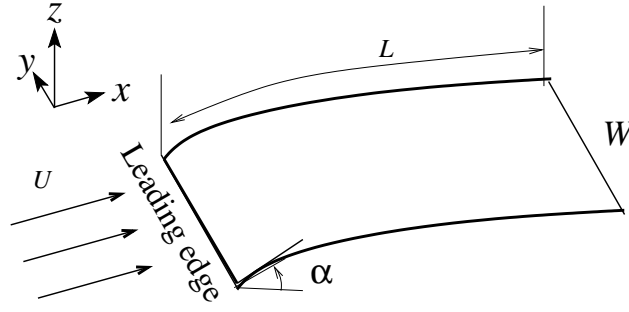
Figure 3.1: Schematic of the elastic panel pitching in a free stream.

3.2 Problem specification

We consider a thin, flexible rectangular panel that rotates around its leading edge harmonically as illustrated in Fig.3.1. The pitching angle is specified as $\alpha = \alpha \sin(2\pi f_0 t)$, where f_0 is the oscillation frequency, α is the maximum angle of attack. The uniform free stream velocity is U, and the domain is unbounded. The panel is considered to be sufficiently thin such that its thickness h has no significant effect on the flow. The homogeneous and isotropic panel has length L, width W, density ρ_s, Young's modulus E, and Poisson's ratio ν_s. The panel is assumed to be nearly inextensible but may bend under the hydrodynamic force. The displacement of the panel is arbitrarily large, but the strain is assumed to be small so that the material still obeys the constitutive law of linear elasticity, which in the local coordinates $(\bar{x}, \bar{y})$ states

$$EI\nabla^4 w_d = f_n(\bar{x}, \bar{y}) \tag{3.1}$$

where $I = h^3/12$ is the area moment of inertia of the cross section per unit span, w_d is the deflection of the plate, and f_n is the normal stress on the plate surface which in the present problem, includes both inertial and hydrodynamic forces. The operator ∇^4 is biharmonic operator in the $(\bar{x}, \bar{y})$ coordinates.

The nondimensional parameters governing the problems are the aspect ratio W/L, pitch-

ing amplitude α, reduced frequency $f = f_0L/U$, Reynolds number $Re = UL/\nu$, mass ratio $\rho_s h/(\rho_f L)$, reduced stiffness $K = EI/(\rho U^2 L^3)$. Mass ratio is set to 0.1 for all, backed by real data of fish fins. The Poisson's ratio of the plate is set at $\nu_s = 0.25$, the aspect ratio $W/L = 0.54$, and the Reynolds number is $Re = 640$, for all the simulations. These parameters are chosen to match those in the experiment by Buchholz & Smits (2008).

To evaluate the performance of propulsion, we define the thrust coefficient C_T and power coefficient as

$$C_T = -\frac{F_x}{\frac{1}{2}\rho U^2 WL}, \qquad C_P = -\frac{P}{\frac{1}{2}\rho U^3 WL}, \tag{3.2}$$

where F_x is the total force on the plate in the x-direction, and P is the total power spent for propulsion and is calculated by $P = -\oint \mathbf{f} \cdot \mathbf{v} dS$. The propulsive efficiency η is then defined to be the ratio between the thrust and power coefficients $\eta = \frac{C_T}{C_P}$.

3.3   Convergence study

A grid convergence study is performed for $f = 1$, $\alpha = 12°$, and $K = 5$ using three grids: the coarse grid with $238 \times 116 \times 168$ points and minimum spacing of $0.025L$ in each direction, the normal grid with $330 \times 142 \times 222$ points and minimum spacing of $0.016L$, and the fine grid with $420 \times 164 \times 272$ points and minimum spacing of $0.0125L$. Figure 3.2 shows the time histories of the tail excursion and C_T computed on these three grids. Based on the results, the normal grid is deemed satisfactory and is used for most of the simulations.
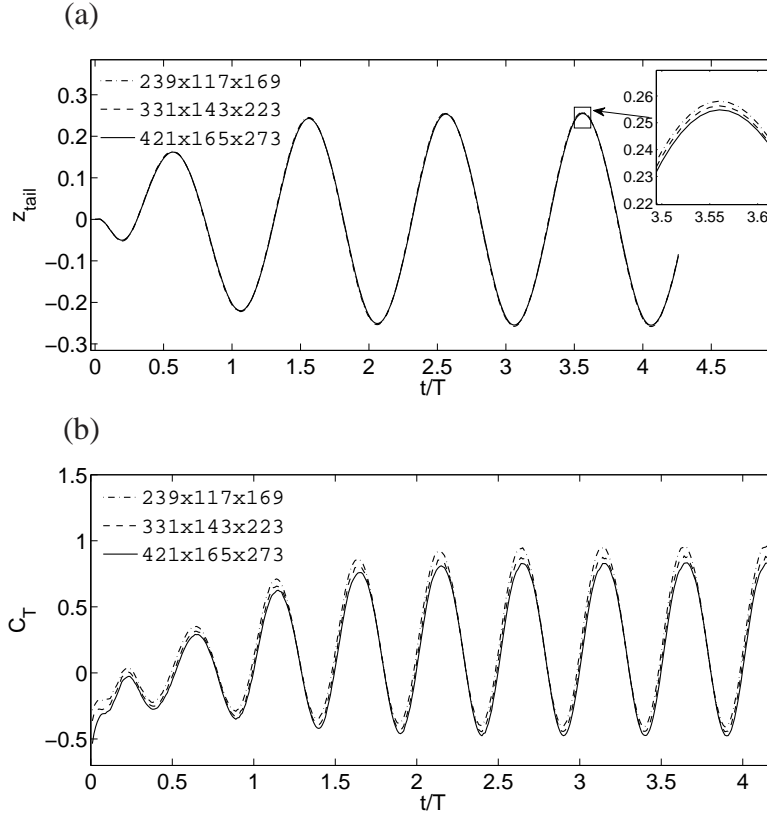
Figure 3.2: Histories of (a) the tail excursion, z_{tail}, and (b) the thrust coefficient computed on three grids for $f = 1$, $\alpha = 12°$ and $K = 5$. The inset in (a) shows a zoom view.

3.4   Structural response

Nondimensional bending rigidity is defined as $K = EI/(\rho_f U^2 L^3)$. Since the spanwise variation of deformation is very small as we observed in all our simulated cases, we examine the deformation at the midspan of the plate only. All the plates deform well-periodically and in a nearly sinusoidal history pattern. Simulations are first run for a series of bending stiffnesses at $\alpha = 12°$, $f = 1$ or 2. Fig. 3.3 shows the normalized peak-to-peak excursion amplitude at the trailing edge, A/L, and the phase delay between the trailing edge and the pitch angle of the leading edge, ϕ. It can be seen from Fig. 3.3(a) that at a particular value of K that depends on f, the excursion amplitude is maximized. For $f = 1$ this critical stiffness is near $K = 2.5$, and for $f = 2$ it is near $K = 10$. The result thus indicates that system resonance has taken place. Note
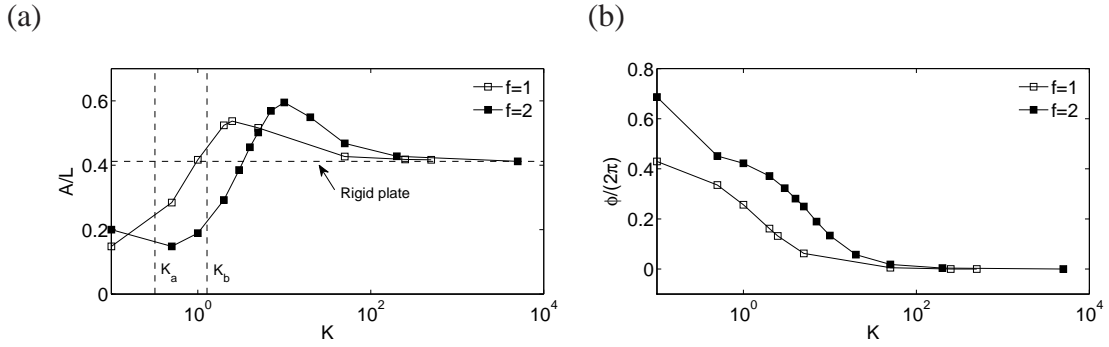
Figure 3.3: The normalized tail excursion (a) and the phase delay between the trailing edge and the leading edge (b) for $\alpha = 12°$. The value of K corresponding to resonance of the plate free-vibrating in vacuum is marked by K_a for $f = 1$ and K_b for $f = 2$.

that the system resonance here is different from the resonance of the free plate vibrating in vacuum. In Fig. 3.3(b) we have marked the values of K that would lead to the first natural vibration mode of the plate, $K_a = 0.32$ for $f = 1$ and $K_b = 1.28$ for $f = 2$. The values of K that would lead to the second natural mode are much lower (less than 0.033). Fig. 3.3(b) shows that the trailing edge exhibits a significant phase delay and it increases as the bending rigidity is reduced. These results are consistent with the 2D analysis of Michelin & Llewellyn Smith Michelin & Llewellyn Smith (2009) for a flexible plate with small heaving amplitude. Note that the bending rigidity here needs to be further reduced in order to achieve the second resonant mode as seen in Michelin & Llewellyn Smith Michelin & Llewellyn Smith (2009), where they studied the higher deformation modes by reducing the plate stiffness by several orders of magnitude. Nevertheless, the possible trend of the second resonance can be seen in Fig. 3.3(a) for the case of $f = 2$, where the tail excursion starts to increase as K is reduced to 0.1. By comparing their numerical model with a linear analysis for the fluid-solid system, Michelin & Llewellyn Smith Michelin & Llewellyn Smith (2009) found that the resonant frequencies can be well predicted by linear theory. In the present case, the resonance takes place near $K = 2.5$ for $f = 1$ and near $K = 10$ for $f = 2$. Therefore, the resonant frequency here scales roughly with $\sqrt{EI}$, i.e., similar to the vibration in vacuum, although the present system includes a surrounding fluid.
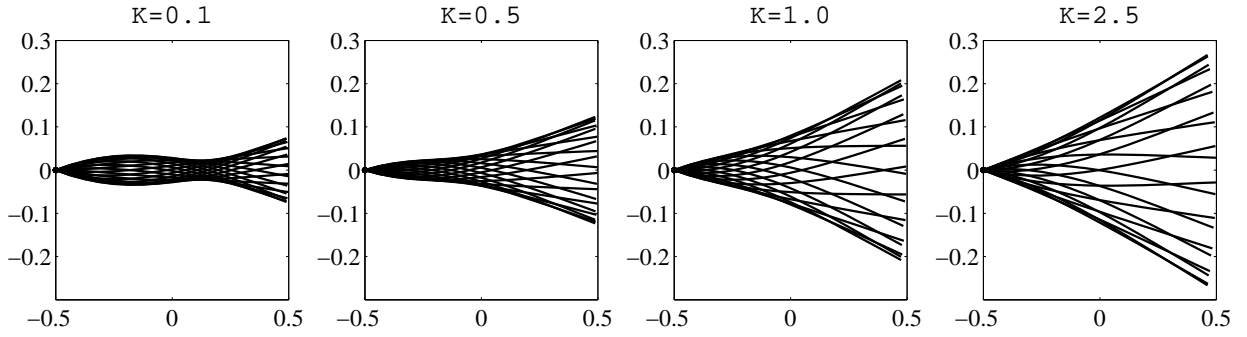
Figure 3.4: Deformation patterns of the plate for $\alpha = 12°$ and $f = 1$.

The deformation pattern of the plate is shown in Fig. 3.4 for $f = 1$ and $K = 0.1, 0.5, 1.0,$ 2.5. For $f = 1$, the plate behaves essentially as a rigid one when K is larger than 100, and significant deformations can be seen when K is less than 10. In Michelin & Llewellyn Smith (2009), they characterized the vibration modes according to the number of necks in the enclosing envelope of the superimposed instantaneous plate shapes. Here we define neck as the portion of the envelope narrower than both its upstream and downstream sides. Following this notion, the vibration pattern shown here for $K = 1.0$ and 2.5 would correspond to the first mode, or the no-neck mode. The pattern for $K = 0.1$ would correspond to the second mode, or the one-neck mode. In the case of $K = 0.5$, the enclosing envelope has a section that is nearly level but can still be grouped into the first mode. It should be pointed out that the present characterization of the deformation modes is different from that of the eigenmodes at which the plate resonates. For the current pitching plate, the second deformation mode can take place either when the plate rigidity is very low or when the pitching amplitude/velocity is very large.

In this work, we mainly focus on the first-mode deformation, which has much higher thrust and propulsive efficiency than the other modes (Michelin & Llewellyn Smith, 2009). As pointed out in Michelin & Llewellyn Smith (2009), this mode does not appear for a passive flag whose flapping motion is induced by system instability. Therefore, rather than extracting energy from the flow, this mode would require energy from an external mechanism.
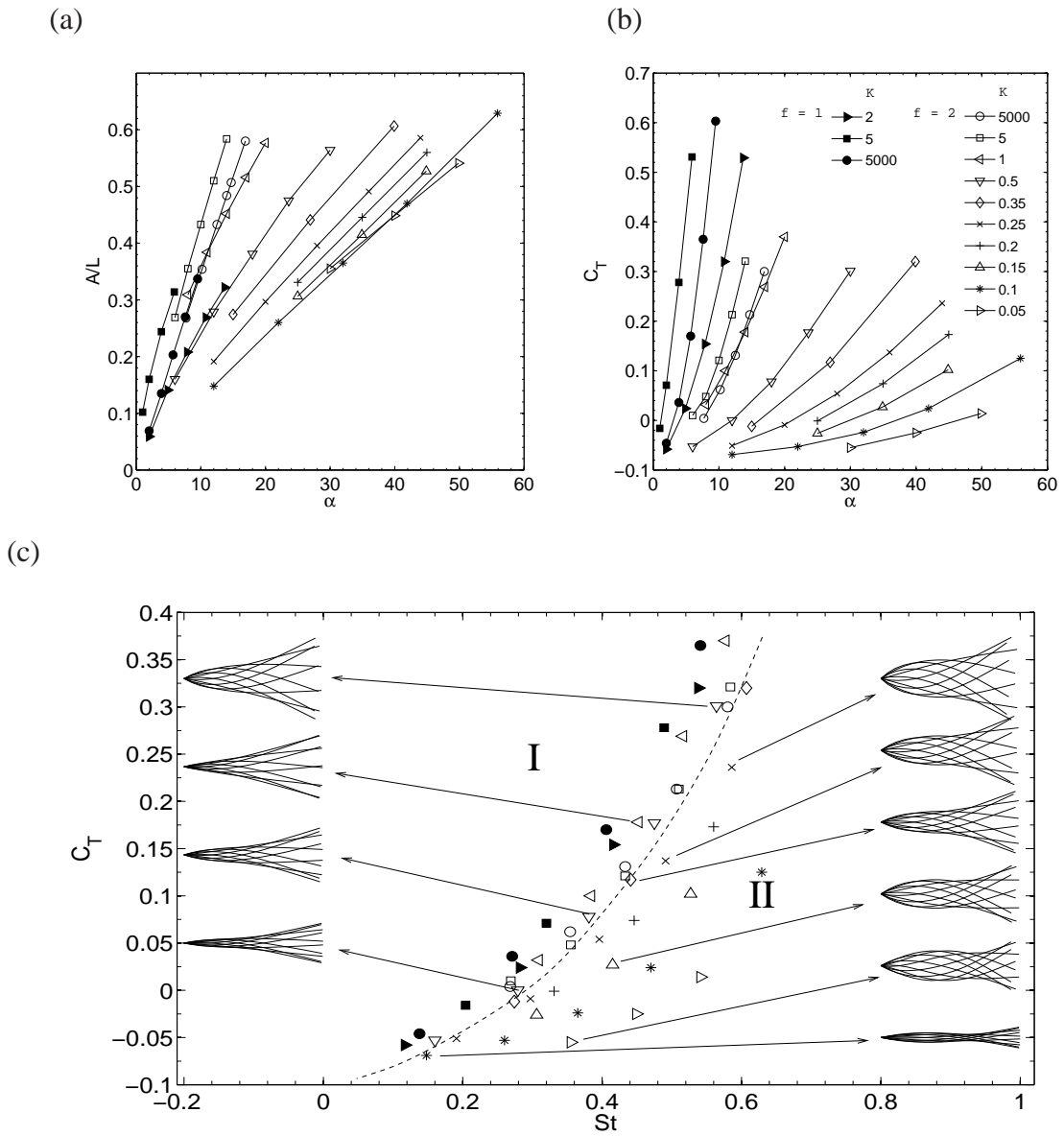
Figure 3.5: The tail excursion (a) and thrust coefficient (b) of the plate for a range of pitching amplitudes and bending stiffnesses. (c) The thrust coefficient re-plotted against the Strouhal number St defined using the tail excursion.

3.5   Thrust production and power efficiency

More series of simulations were run for a range of values of K and α. The nondimensional frequency remains at $f = 1$ or $f = 2$. The results of these cases are plotted in Fig. 3.5, where the data belonging to the same K values have been grouped using the same symbol. Fig. 3.5(a)

shows that for all the cases considered here, the tail excursion increases monotonically as α is raised. Meanwhile, the thrust produced by the plate, as shown in Fig. 3.5(b), grows as well due to the increased flapping amplitude. For most cases, the tail excursion of the flexible plate is significantly lower than that of the rigid plate (represented by $K = 5000$) when α is fixed. For some cases where the plate oscillates near the system's resonant frequency, e.g., $K = 5$, the tail excursion exceeds that of the rigid plate, and correspondingly, the flexible plate produces higher thrust than its rigid counterpart.

For a flexible wing, we define the Strouhal number as $St = \frac{fA}{U}$, where the peak-to-peak excursion A in used. Such a definition has been used extensively to scale the thrust performance of a rigid pitching wing Triantafyllou *et al.* (2004), and here the same definition will allow us to compare the flexible wing with the rigid wing that has an equivalent flapping amplitude.

In Fig. 3.5(c), we plot the thrust coefficient against the Strouhal number, which is in the range between 0.1 and 0.7. The deformation patterns of some typical cases are shown in this figure to aid the analysis. We draw an approximate boundary to separate the cases where the plate has the second-mode pattern from the cases with the first-mode pattern, and we use I and II to mark the two regions as shown. It can be seen that in Region I where the rigid cases and the first-mode cases lie, the data roughly collapse onto the same curve regardless various combinations of f, K, and α in these cases. The result implies that despite the wing deformation, the propulsive force of the present wing depends almost exclusively on the Strouhal number as long as the wing deformation is of the first mode. On the other hand, in Region II where the second-mode cases lie, the data are scattered and do not appear to follow a general curve. In addition, these cases have lower thrust compared to those cases in Region I at the same Strouhal number. We point out that the boundary between the two regions should not be viewed as a sharp line but represents instead a transition zone. As the intermediate cases with $f = 1$ and K
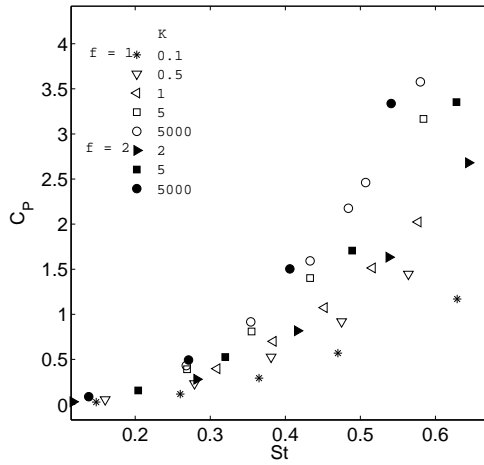
(a)   (b)
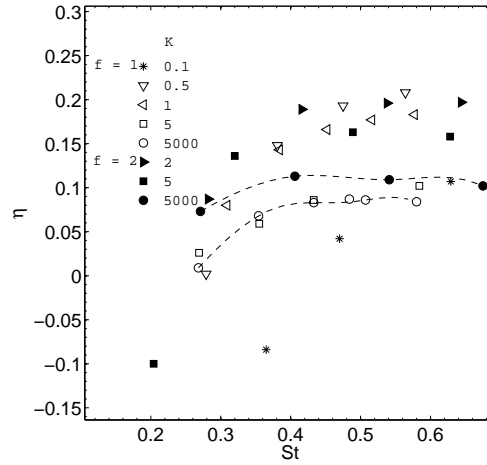
Figure 3.6: The power coefficient C_P (a) and power efficiency η (b) versus the Strouhal number. The rigid-wing cases have been marked with dashed lines in (b).

varying from 0.2 to 0.5 indicate, the appearance of the second mode is in a gradual rather than drastic manner.

In a recent experimental study by Bohl & Koochesfahani (2009), a rigid NACA-0012 airfoil pitching sinusoidally at small amplitude and high reduced frequencies was used to study the flow field and to obtain the scaling law of the thrust versus the Strouhal number for $St < 0.25$. In their study, a control volume analysis that takes into account the streamwise velocity fluctuations and the pressure term was adopted to estimate the mean thrust. Although the Reynolds number in that study is much higher (on order of 10^4), the scaled thrust in Bohl & Koochesfahani (2009)(see Fig. 15) shows a similar trend and magnitude as in our study.

The plots of the thrust and power coefficients versus the plate stiffness would show that at the system resonance, both the thrust and power consumption reach their respective peak values like the reduced excursion A/L shown in Fig 3.3(a). In addition, the optimal efficiency would take place at a lower value of K than that for the resonance. These results are consistent with the 2D analysis in Michelin & Llewellyn Smith (2009) and are thus not further discussed in the present

69

work. Here we plot the power coefficient against the Strouhal number in Fig. 3.6(a), where some cases with intermediate values of K have been excluded to avoid data clustering. It can be seen that unlike the thrust coefficient, the power coefficient does not collapse onto a generalized curve. Overall, the power coefficient increases as St is raised. At a constant St, especially when $St > 0.3$, the flexible cases typically have a lower power coefficient than the rigid case. Therefore, by deforming passively and storing/releasing energy at different phases, the flexible plate may require less power input while still producing the same amount of thrust compared to the rigid plate with the equivalent oscillating frequency and magnitude of excursion.

The power efficiency is plotted versus the Strouhal number in Fig. 3.6(b). It can be seen that for the rigid plate, the best performance is found for St near 0.4. Below $St = 0.2$, the efficiency would drop quickly and it may become negative with the thrust turning into drag. Beyond $St = 0.4$, the efficiency is not particularly sensitive to the Strouhal number. Compared to the rigid plate, the flexible plate shows a similar trend as St is varied, but its peak efficiency typically occurs at a higher range of Strouhal numbers, e.g., between 0.4 and 0.6. Consistent with the power analysis, the flexible plate in most cases has higher efficiency than the corresponding rigid plate when St is fixed. Exceptions are found in those cases with low plate rigidity, e.g., $K = 0.1$ and $f = 1$, where the plate has exceedingly large deformation and exhibits the second-mode pattern.

3.6   Wake structure

The vortices in the wake are visualized by plotting the isosurface of an invariant of the velocity gradient tensor as defined in Mittal & Balachandar (1995). Fig. 3.7 shows the wake structure for the plate pitching with $\alpha = 12°$, $f = 1$, and $K = 0.1, 0.5$, or 2.5. The Strouhal numbers in these three cases are $St = 0.15, 0.28$, and 0.47, respectively. As discussed in Buch-
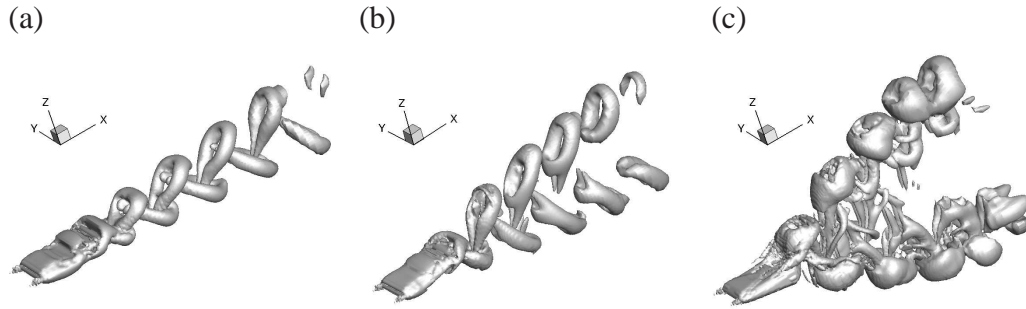
Figure 3.7: The wake structure for $\alpha = 12°$, $f = 1$, and (a) $K = 0.1$ ($St = 0.15$), (b) $K = 0.5$ ($St = 0.28$), and (c) $K = 2.5$ ($St = 0.47$).

holz & Smits (2006), wake transitions are found when increasing the Strouhal number for the rigid plate. Such transitions are also observed here for the flexible plate by varying K. We point out that the specific Strouhal numbers for the transitions in our simulations are lower compared to those in Buchholz & Smits (2006), possibly because we have varied the excursion amplitude, rather than the pitching frequency, when changing the Strouhal number. In Fig. 3.7(a) where $St = 0.15$, a chain of horseshoe-shape vortices are developed, and they are interlocked together, forming a reverse von Kármán vortex street behind the plate. When the Strouhal number is increased to 0.28 (Fig. 3.7(b)), the horseshoe vortices turn into vortex rings which form two separate trains, and the rings are mostly oriented in the streamwise direction. Hairpin-like legs can be seen connecting the two vortex trains. As the Strouhal number is further increased to 0.47 (Fig. 3.7(c)), the vortex rings in the wake become more oriented in the transverse direction, and they develop more complex hairpin legs. Because of their orientation and the self-induced motion, these vortices also travel transversely and thus make the wake become wider. More details of the similar vortex topology have been discussed in Buchholz & Smits (2006, 2008) for the rigid plate.

The wake topology of the flexible plate was also examined against the corresponding rigid plate at the same Strouhal number. An example of this comparison is shown in Fig. 3.8, where

71

(a)   (b)   (c)

(d)   (e)   (f)
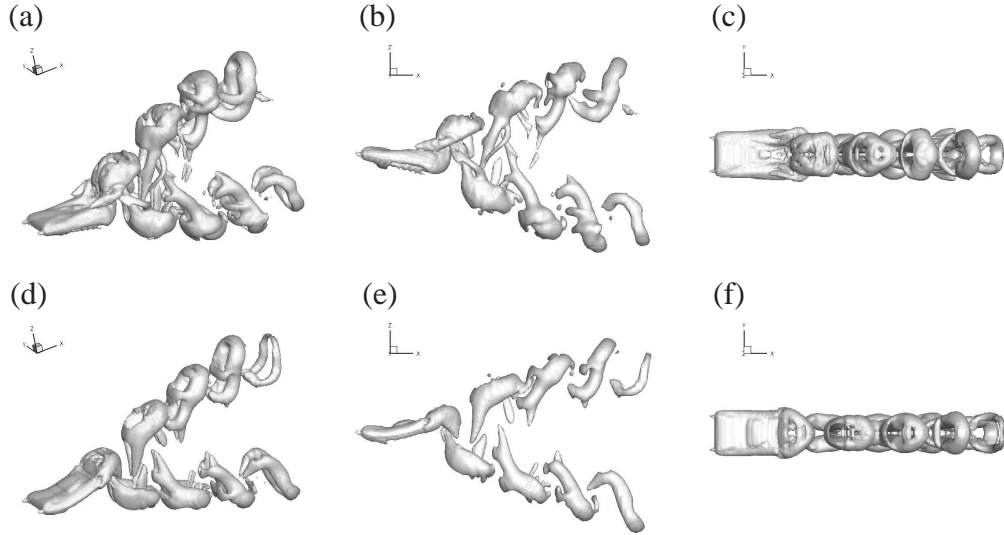
Figure 3.8: Wake structures of the rigid plate at $\alpha = 14°$ (a,b,c) and the flexible plate at $K = 0.5$ and $\alpha = 24°$ (d,e,f). In both cases, $f = 1$ and $St = 0.48$. The 3D view, side view, and top view are shown.

$f = 1$ and $St = 0.48$. For the flexible case, $K = 0.5$ and $\alpha = 24°$ have been used in the simulation, and for the rigid case, $\alpha = 14°$ is used to achieve the same Strouhal number. As shown in Fig. 3.5(c), the thrust coefficients of these two cases are very close to each other and both are around $C_T = 0.18$. From Fig. 3.8, we note that the wake patterns are similar between the two cases, e.g., the shape and orientation of the vortex rings, the branches of the vortex trains, and the angle between the two trains. In a recent experimental study by Dewey *et al.* (2012), the bifurcation distance of the vortex branches behind an oscillating batoid fin scales with the Strouhal number, which is also defined using the magnitude of excursion. Therefore, our result appears to be consistent with theirs in that regard. From Fig. 3.8 we can see that there are some slight differences between the rigid and the flexible cases. For example, the wake of the rigid plate has the multiple complex-shaped hairpin legs that connects the two vortex trains, while many of those legs have diminished in the wake of the flexible plate. In addition, the vortex rings of the flexible plate also appear to be thinner, and the wake is more compressed in the spanwise direction compared to the wake of the rigid plate. These results indicate that the

wing deformation has somewhat simplified the wake structure.

3.7 Conclusion

A three-dimensional fluid–structure interaction of a flexible pitching plate at a low aspect ratio and a low Reynolds number is studied numerically. The pitching amplitude, frequency, and bending stiffness of the plate are varied, and the propulsive performance is studied. It is found that the thrust coefficient scales reasonably well with the Strouhal number that is defined using the trailing edge excursion of the plate in the transverse direction, provided that the deformation pattern is the first mode as defined by the shape of its enclosing envelope. Under such a condition, the flexible plate would produce approximately the same amount of thrust as the rigid plate pitching at the same frequency and with an equivalent excursion, and furthermore, the flexible plate is more power-efficient compared to the rigid plate. The wake topologies are similar between the flexible and rigid plates with equal Strouhal number, although hairpin-like vortex structures may take a simpler form in the flexible case.

CHAPTER IV

DYNAMIC PITCHING OF AN ELASTIC RECTANGULAR WING IN HOVERING

MOTION

4.1   Background

A flapping wing is subject to an inertial force due to its own mass and also to the aerodynamic forces from the surrounding air. Previous studies suggest that both forces may be able to cause an insect wing to deform. For example, Ennos (1988*a*) measured the force manually applied on the wings of two species of flies, and he concluded that the aerodynamic forces experienced by the insect wings during flight would be sufficient to produced the observed values of wing twist and camber. In another study, Ennos (1988*b*) measured the mass distribution and determined the torsional axis of three species of flies, and the result shows that the inertial effect alone could develop the pitching velocity observed at stroke reversal. Combes & Daniel (2003*b*) compared vibrations of the excised hawkmoth wing in air and in helium (15% of the air density) and noticed that the deformation patterns in the two cases are close to each other. Their result suggests that the hawkmoth wing is mainly deformed by the wing inertia during stroke. Whether it is the wing inertia or the aerodynamic forces that cause the wing deformation may determine timing of the deformation. The reason is that there is a phase difference between the inertial force and the aerodynamic forces in a flapping cycle. Roughly speaking, the inertial force reaches its maximum around stroke reversal when the wing has the highest acceleration, while the aerodynamic forces peak around mid-stroke when the wing has the fastest translation. If the aerodynamic forces are strong enough, they may maintain the passive pitching caused by

the inertial effects at stroke reversal (Ennos, 1988*a*). Though these qualitative considerations make sense, a detailed study is needed to find out the exact timing and contribution of all the forces involved. Furthermore, it is necessary to include fluid–structure interaction in such a study and to simultaneously investigate the aerodynamic consequences of the wing deformation. Currently, the relative roles of the inertial and aerodynamic torques in the deformation and performance of flapping wings are still elusive.

Since the aerodynamic pressure scales with ρU^2, where ρ is the fluid density and U is the characteristic velocity of the wing, and the inertial force per unit area scales with $\rho_s h U^2 / \mathcal{L}$, where ρ_s is the density of the wing material, h is the membrane thickness (collectively, $\rho_s h$ is the surface density), and $\mathcal{L}$ is the characteristic length scale, the ratio between the inertial effect and the aerodynamic effect is thus represented by the mass ratio $\rho_s h / (\rho \mathcal{L})$, denoted by m^* here. In the current study, we choose the chord length c for the length scale. From the previously available insect data, Yin & Luo (2010) estimated that the mass ratio is around $m^* = 1$ for the dragonfly used in Chen *et al.* (2008) and around $m^* = 5$ for the hawkmoth used in Combes & Daniel (2003*b*). Using the mass distribution measured by Ennos (1988*b*), we estimate that the mass ratio of the hoverfly in his experiment is around $m^* = 0.5$ near the wing tip. These estimates give us a sense of relative importance of the inertial force in the wing deformation of these insects and will form the basis for the choice of the mass ratio in the current study.

In the study by Yin & Luo (2010) a numerical simulation of the fluid–structure interaction for a wing section was performed and the effect of the wing inertia in hovering flight was investigated. By comparing $m^* = 1$, 5, and 25, they found that the wing at low mass ratios can achieve much higher lift per unit power and it does so by yielding itself to the aerodynamic forces and reducing the drag force. In addition, significant phase difference in the deformation of the wing was found between the high mass ratio and the low mass ratio cases. In the present work, we use

75

a flexible rectangular plate at a low aspect ratio to model the effect of chordwise deformation in hovering flight. The plate revolves around a pivot point and meanwhile rotates around its rigid leading edge to mimic stroke and global pitching (active pitching at the wing root) of a real insect wing. The 3D fluid–structure interaction is solved by coupling an immersed-boundary flow solver and a nonlinear finite-element method for the structural dynamics. By systematically varying the wing stiffness, mass ratio, and phase of the global pitching, we hope to gain insight into the interplay among the inertial, aerodynamic, and elastic forces in the flapping flight. The paper is organized as follows. The problem statement is described in § 4.2; results are presented in § 4.3 to § 4.7 ; and finally conclusions are given in § 4.8.

4.2   Problem formulation

We consider a thin rectangular plate of aspect ratio 2 which rotates around the z-axis while pitching around its leading edge as shown in Figs. 4.1(a,b). The plate has a chord length c and a spanwise width of $L = 2c$. The leading edge is rigid, but the bulk surface of the plate is flexible and is both homogeneous and isotropic (Fig. 4.1(c)). The wing is activated by the torques at the pivot point so that the leading edge undergoes two degrees-of-freedom rotations described by

$$
\begin{aligned}
\phi &= \frac{A_\phi}{2} \sin(2\pi f t + \frac{\pi}{2}) \\
\alpha &= \frac{A_\alpha}{2} \sin(2\pi f t + \varphi),
\end{aligned}
\tag{4.1}
$$

where f is the frequency, ϕ is the stroke angle defined as the angle between the leading edge and the y-axis, α is the active pitching angle specified at the wing root, φ is the phase angle between wing stroke and the pitching motion with $\varphi = 0$ corresponding to symmetric pitching. A_ϕ and A_α are the amplitudes of stroke and pitching, respectively. The kinematics of the leading edge

76
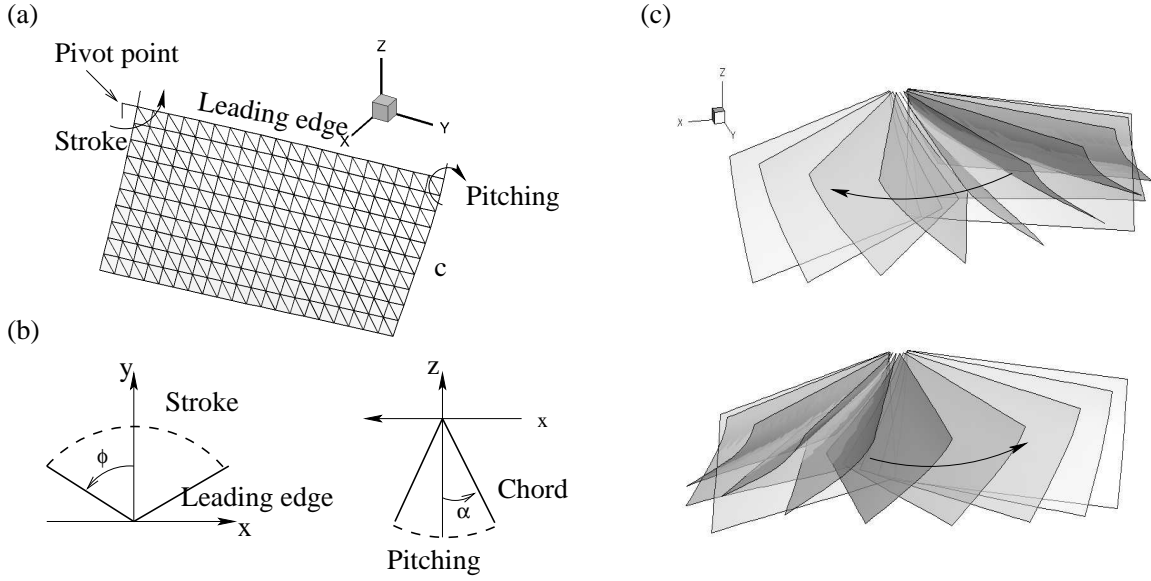
Figure 4.1: The wing model used in current study. (*a*) Configuration and mesh of a rectangular wing. (*b*) Sketch of the specified kinematics. (*c*) Instantaneous wing deformation during a stroke.

is shown in Figs. 4.1(a,b). The origin of the coordinate system is located at the pivot point, and

the length of the wing arm (from the pivot point to the inner edge of the plate) is equal to $0.1c$.

In current study, we choose $A_\phi = 2\pi/3$ and $A_\alpha = \pi/3$, which are in the range of real insect

data (e.g. Wang *et al.*, 2003; Hedrick *et al.*, 2009).

The plate is characterized by its surface density $\rho_s h$, where ρ_s is the density of the solid

and h is the thickness of the plate, Poisson's ratio v_p, and the flexural stiffness EI, where E is

Young's modulus and $I = h^3/12$ is the second moment of area of the cross section. Poisson's

ratio is assumed to be $v_p = 0.25$. In addition to the phase angle φ, the other non-dimensional

groups of the problem include the Reynolds number, mass ratio, and frequency ratio of the plate,

which are given by

$$Re = \frac{Uc}{\nu}, \qquad m^* = \frac{\rho_s h}{\rho c}, \qquad \omega^* = \frac{2\pi f}{\omega_n}, \qquad (4.2)$$

where U is the characteristic velocity, chosen to be the mean tip-velocity of the leading edge,

77

$U = 2A_\phi f(L + 0.1c) = 8.797cf$, ρ and ν are the fluid density and viscosity, respectively, and $\omega_n = \frac{1.8751^2}{c^2} \sqrt{\frac{EI}{\rho_s h}}$ is the first natural frequency of the plate using the classical Euler-Bernoulli beam theory. Note that when the other parameters are fixed, $\omega^* = 0$ corresponds to a rigid plate, and as ω^* is increased, the plate becomes more flexible. An alternative of normalizing the bending rigidity is to use the dynamic pressure, ρU^2 (e.g. Prempraneerach *et al.*, 2003). The approach in Eq. (4.2) is chosen here since it gives a direct measure of how close the flapping frequency is to the resonant frequency of the wing structure.

To evaluate the wing performance, we define the lift F_L as the z-component of the resultant fluid force, the drag F_D as the force component in the xy-plane and perpendicular to the leading edge. In each half-stroke, the drag is positive when it is against the translation of the leading edge. The aerodynamic power P is computed by integrating the dot product of the fluid force and local velocity of the wing over the entire wing surface. The lift and drag coefficients, C_L and C_D, are defined by normalizing the corresponding force with $\frac{1}{2}\rho U^2 cL$, and the power coefficient, C_P, is defined by normalizing P with $\frac{1}{2}\rho U^3 cL$.

4.3   Wing deformation

The wing deformation is dominated by the typical chordwise bending illustrated in Fig. 4.2. Since the bending is greater at the wing-tip than at the root due to the non-uniform load along the span, the entire wing surface is also warped. To quantify the amount of chordwise deformation, we define the local passive pitching angle, α_p, as the included angle between the deformed wing and its equilibrium position, measured in a plane perpendicular to the leading edge (see Fig. 4.2). The effective pitching angle, α_e, is then given by $\alpha_e = \alpha + \alpha_p$. The active pitching angle, passive pitching angle, and effective pitching angle at mid-span for $m^* = 5$ and $\omega^* = 0.36$ are shown in Fig. 4.3(a) for an established cycle. Passive angle α_p is overall in phase with α.
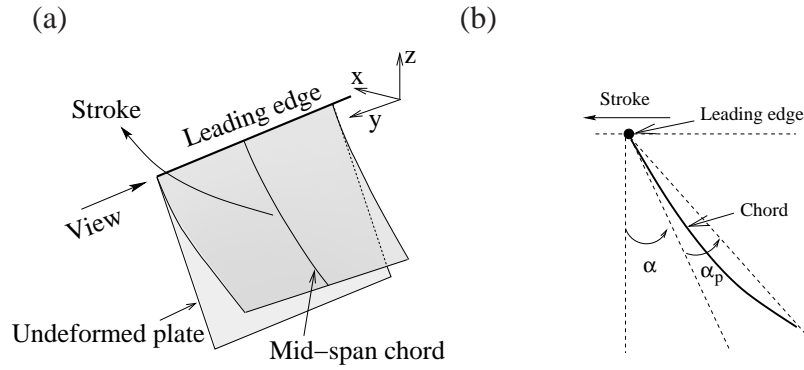
Figure 4.2: Illustrations of (a) the deformed wing and chord and (b) definition of the passive pitching angle, α_p.
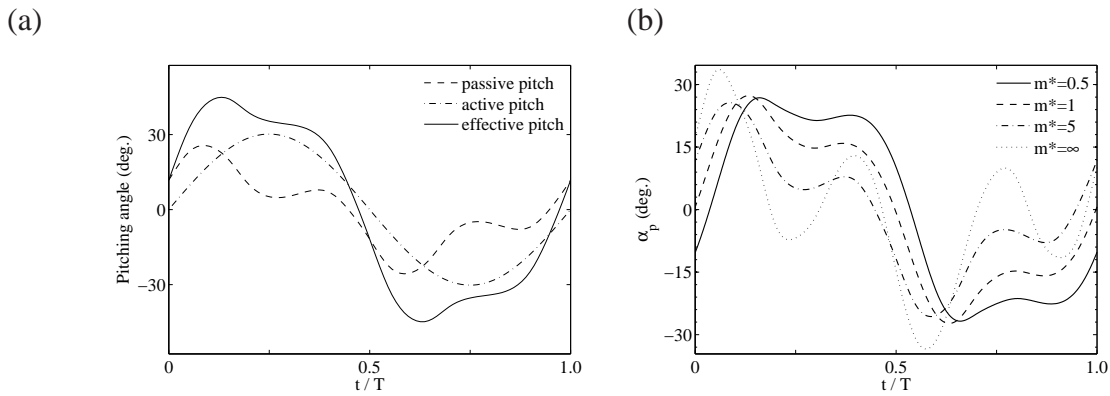
Figure 4.3: (a) Active, passive, and effective pitching angles at mid-span in a cycle for $m^* = 5$. (b) Passive pitching angle at mid-span for different mass ratios. In these cases, $\omega^* = 0.36$ and $\varphi = 0$.

The magnitude of α_p exhibits two distinct peaks during each half cycle, one taking place during the wing-acceleration stage and the other during the wing-deceleration stage. The temporal characteristics of the passive pitching angle can be explained by the combination of the wing inertia, the aerodynamic drag and lift, and the elastic force at different phases of a single stroke. The passive pitching angle at mid-span is plotted in Fig. 4.3(b) for different mass ratios. For all the cases, α_p has two peaks within each half cycle. The two peaks are more visible as m^* is increased, indicating the natural vibration of wing becomes more significant at higher

mass ratios. The natural vibration is most obvious for the $m^* = \infty$ case, where the aerodynamic forces are absent. In fact, since there is no external damping in this case, the wing deformation is significantly aperiodic, with the phases of the two peaks relatively consistent but the magnitudes varying randomly from cycle to cycle by approximately 30%. On the other hand, for the lowest mass ratio, $m^* = 0.5$, the two peaks are much less clear, indicating that the wing deformation is sustained by the aerodynamic forces during mid-stroke.

The instantaneous deformed wing shape is visualized in Fig. 4.4 for $m^* = 0.5, 5$ for a moderate rigidity (tip view). Surface warping(spanwise deformation) is characterized by showing both base and tip edges. For $m^* = 5$, large surface warping is observed during wing reversal when the wing experiences the greatest acceleration, and only small spanwise deformation is seen during mid-stroke. For $m^* = 0.5$, large spanwise deformation is observed during both wing reversal and mid-stroke, and its magnitude is much higher than that in the case of $m^* = 5$, especially during wing reversal. Chordwise deformation will be discussed later.

The two-peak oscillations in the pitching angle are also observed in real insect wings (Walker *et al.*, 2010, see Fig.4 in). In the present case, the first peak is caused by the inertia force and the second one has significant contribution from the flow. As seen from the plot of α_e in Fig. 4.3(a), the temporal behavior of the passive pitching causes the total pitching angle to deviate from the active pitching significantly. Such deviation has an important effect on the lift and drag forces and will be discussed later in § 4.4.

Pitching torques(the torque with respect to the leading edge) are checked to understand the temporal behavior of the wing deformation. The results are shown in Fig. 4.5 for the cases of $m^* = 0.5$, 1, and 5. These cases correspond to those in Fig. 4.3(b). For $m^* = 5$, the maximum inertial torque takes place soon after the start of the stroke or somewhere before one-forth of the half cycle. In comparison, the aerodynamic torque is much lower and is only comparable
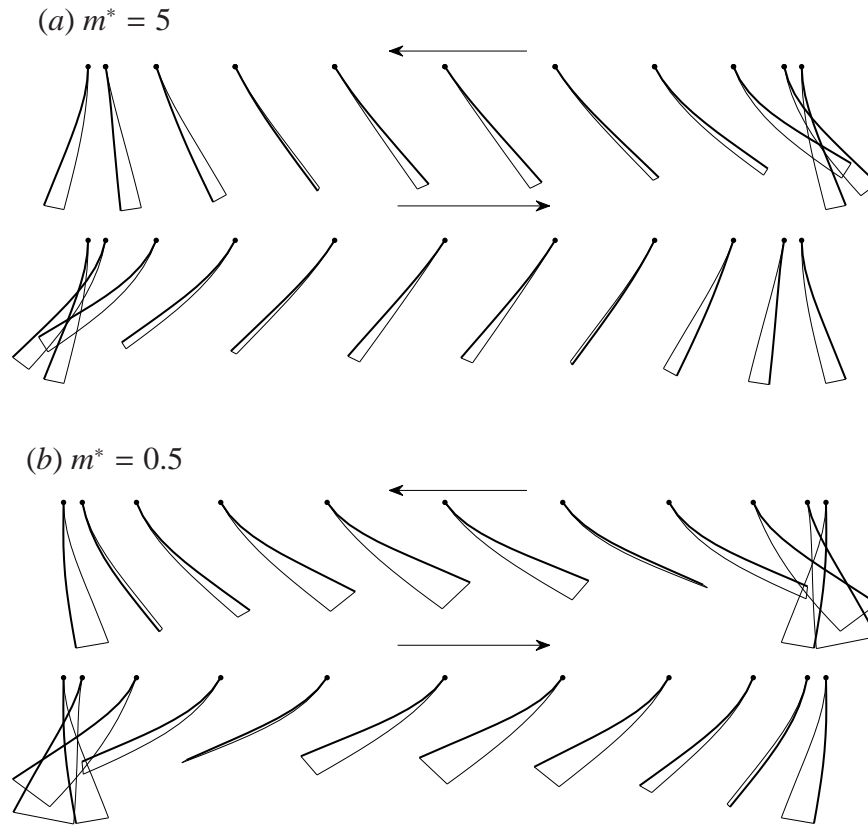
Figure 4.4: Wing deformation in one flapping cycle as viewed by following the leading edge and from the wing tip to base, where the thick line is the tip edge and the thin line is the base edge. The cases here are (a) $m^* = 5$ and (b) $m^* = 0.5$, $\omega^* = 0.36$, and $\varphi = 0$.
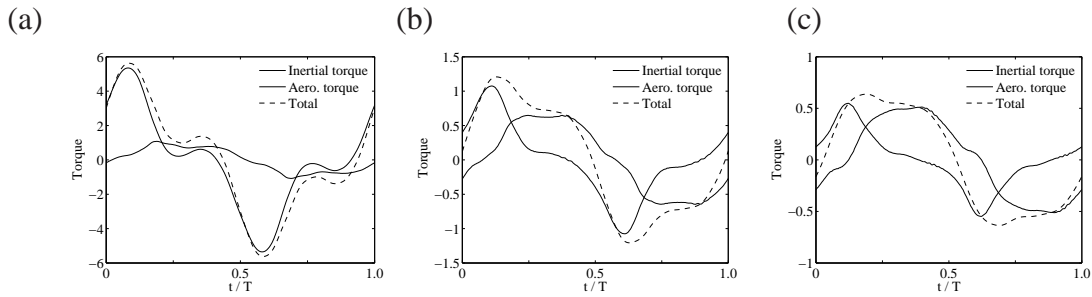
Figure 4.5: Instantaneous inertial and aerodynamic torques around the leading edge reduced by $\frac{1}{2}\rho U^2 c^2 L$ for (a) $m^* = 5$, (b) $m^* = 1$, and (c) $m^* = 0.5$ where $\omega^* = 0.36$ and $\varphi = 0$. Here the torques are normalized by $\frac{1}{2}\rho U^2 c^2 L$.

to the second peak of the inertial torque. As the mass ratio is reduced, the aerodynamic torque becomes more important relative to the inertial torque. The aerodynamic torque reaches its maximum level well after the inertial torque and has a much longer duration. In the cases of
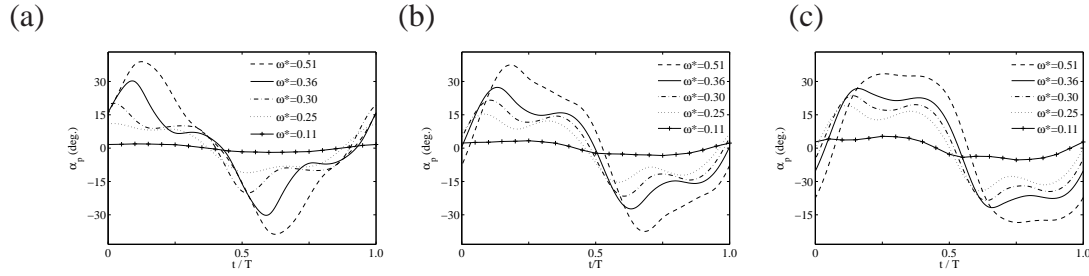
Figure 4.6: Passive pitch angle at mid-span in one cycle for cases of various frequency ratios for (*a*) $m^* = 5$, (*b*) $m^* = 1$ and (*c*) $m^* = 0.5$.

$m^* = 1$ and 0.5, the second peak of the inertial torque has disappeared due to the increased fluid damping.

From the torque plots, it is straightforward to explain the behavior of the passive pitching in Fig. 4.3(b). At mass ratio $m^* = 0.5$, the total torque is relatively constant during much of the half-stroke and has produced a similar pattern in the passive pitching angle. In addition, the opposite aerodynamic torque before and during stroke reversal works against the inertial torque for the low mass ratios, and thus the pitching rotation of the wing is delayed for $m^* = 0.5$ and 1.

The effect of wing rigidity on the passive pitching angle at mid-span is shown in Fig. 4.6 for mass ratios $m^* = 0.5$, 1, and 5. For all the mass ratios, the maximum value of the passive pitching angle is raised as the frequency ratio ω^* increases. This value varies between 11.5° and 38° for $m^* = 5$ as ω^* goes from 0.25 to 0.51. The range of variation decreases for lower mass ratios mainly due to raising of second peak. The figure also shows that in the most flexible case, $\omega^* = 0.51$, the two-peak pattern of α_p disappears and is replaced by a much wider single peak for all three mass ratios. For low mass ratios such as $m^* = 0.5$, the single peak of α_p at $\omega^* = 0.51$ has a nearly flat top and is apparently caused by the prolonged aerodynamic effect. In the cases of low mass ratios and high frequency ratios (e.g., $m^* = 0.5$ and $\omega^* = 0.51$), α_p has an opposite sign in the beginning of a half-stroke compared to the rest of the half-stroke. That is, α_p is negative at $t/T = 0$ and positive at $t/T = 0.5$, which means that the wing rotation at

82

stroke reversal is delayed. The situation is opposite for high mass ratios. In the case of $m^* = 5$, the wing rotation at stroke reversal is advanced.

4.4   Lift, drag and aerodynamic power

The instantaneous lift and drag coefficients are shown in Figs. 4.7(a-d), the corresponding effective pitching angle, α_e, is plotted in Fig. 4.7(e,f). All lift graphs display a single peak around or after the mid-stroke due to the sinusoidal kinematics. For low mass ratio, as the wing becomes more flexible the peak lift is reduced. There are two possible reasons for this reduction. First, the effective angle of attack, defined as the angle between straight line connecting leading and trailing edges of a chord and the direction of the stroke, is lower as the wing deforms more. According to Dickinson *et al.* (1999), the optimal angle of attack is around 45° for a rigid uncambered wing. The lowest angle of attack in the present case is near 25° for the most flexible case. Second, the deformed chord forms a reverse camber, as seen in Fig. 4.4, and is thus not beneficial for lift production.

For $m^* = 5$, the value and timing of the peak lift do not appear to have a consistent trend. Instead, the lift may peak either before, near, or after the mid-stroke. This can be explained by looking at the characteristics of wing deformation. For the wing at $\omega^* = 0.36$, the passive pitching angle history in Fig. 4.3(a) shows that α_p has a sharp drop after the first peak, which suggests that the wing is recovering its shape due to elastic rebound. Such a quick recovery counteracts the active pitching and leads a sudden drop in the effective pitching angle prior to mid-stroke as seen in Fig. 4.7(f). Thus, the trailing edge of the wing presses downward and produces extra lift, causing the total lift to peak before mid-stroke. This effect is not obvious for $m^* = 0.5$ where the aerodynamic forces act as a strong damping source delaying the wing recovery.
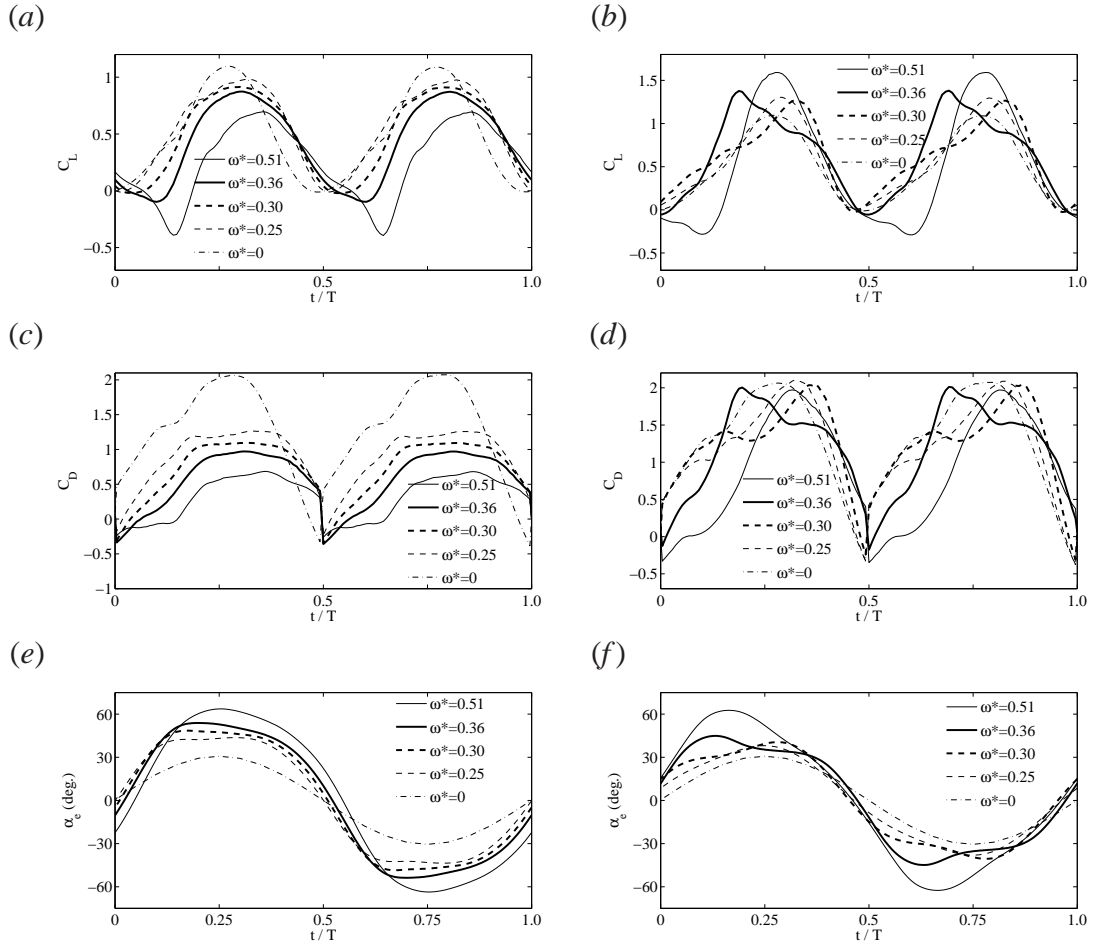
Figure 4.7: Lift (*a,b*), drag (*c,d*), and effective pitch (*e,f*) histories for $m^* = 0.5$(left column) and $m^* = 5$(right column). The phase $\varphi = 0$.

The drag histories plotted in Fig. 4.7(d) show that the drag produced by the flexible wing is comparable to that by the rigid wing. This result is in sharp contrast with that for $m^* = 0.5$. Generally the drag by higher mass ratio wings is much larger due to the elastic recovery, which does not only increase the frontal area of the wing but also cause the wing to move faster relative to the fluid.

From the histories of the aerodynamic forces and wing deformation, we see that the lift and drag of a flexible wing depends not only on the instantaneous pitching angle but also on the rate of pitch and camber of the wing. To compare the overall performance of the wings, we compute the mean force and power coefficients for all the cases. The averaged data are taken over several

established cycles. The results are shown in Fig. 4.8, from which we may see clearly the effect of wing flexibility and inertia.

The mean lift coefficient is plotted against the frequency ratio in Fig. 4.8(a) for the three mass ratios, $m^* = 0.5$, 1, and 5. Here the rigid wing is represented by the case $\omega^* = 0$, at which the wing inertia has no effect on the aerodynamics since the wing kinematics has been prescribed. For each mass ratio, we see that moderate wing flexibility increases the lift, but exceeding flexibility may not help with lift production and even leads to lift loss. As discussed earlier, the lift augmentation mechanisms for different mass ratios are not entirely the same. At high mass ratios, the lift enhancement is due to the passive rotation of the wing during elastic recovery, while at low mass ratios, the enhancement is more likely due to a combination of wing recovery and the prolonged favorable angle of attack during a stroke. Similar to the 2D study by Yin & Luo (2010), there exists an optimal ω^* at which the highest lift is produced, and this optimal point moves to a higher value as the mass ratio is raised. Figure. 4.8(a) shows that the optimal ω^* is around 0.2, 0.25, and 0.35 for the mass ratio $m^* = 0.5$, 1, and 5, respectively. Furthermore, the figure shows that the maximum lift is higher for the wing with larger mass ratios. This maximum value is $\bar{C}_L = 0.55$ for $m^* = 0.5$ and $\bar{C}_L = 0.65$ for $m^* = 5$.

Figure. 4.8(b) shows the mean drag coefficient for the three mass ratios and a range of wing flexibility. The overall trend is that the drag drops when the wing flexibility is increased. At the highest mass ratio, $m^* = 5$, the drag is only slightly lower than that of the rigid wing for most of the cases except for $\omega^* = 0.51$, where the drag is also significantly reduced. The lowest mass ratio, $m^* = 0.5$, has the lowest drag among the three mass ratios, which is understandable since the wing yields to the aerodynamic torque during wing translation and on average it has the least frontal area and the lowest rate of pitch. This result is consistent to the 2D study in Yin & Luo (2010).
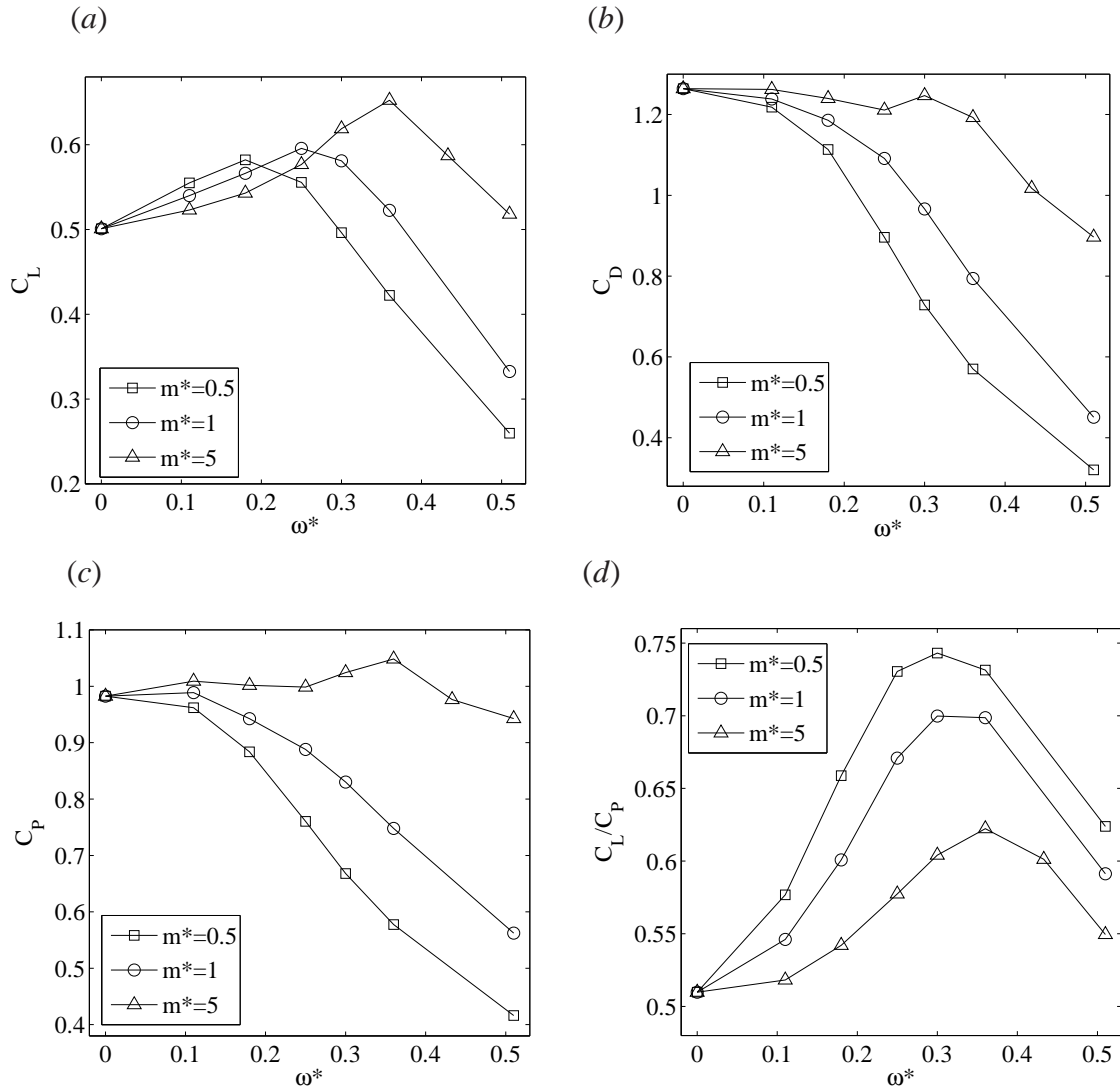
Figure 4.8: Mean lift (*a*), drag (*b*), power (*c*) coefficients and lift-to-power ratio (*d*) for the three mass ratios and $\varphi = 0$.

The elastic wing serves as an energy capacitor by temporarily storing energy in the forms of elastic potential and later releasing it in the forms of kinetic energy and work output done on the fluid. In Figs. 4.8(c,d) we plot the mean power coefficient and the aerodynamic efficiency. Unlike the 2D study of Yin & Luo (2010), here we exclude the inertial power and evaluate the power efficiency by calculating the net aerodynamic power only. The power coefficient in Fig. 4.8(c) displays a similar trend as the drag coefficient as ω^* and m^* are varied. This is because most of the energy has been consumed through the drag rather than through the lift.

For $m^* = 5$ the power coefficient does not change significantly as ω^* is varied. For the other two mass ratios, the power coefficient drops quickly as ω^* is increased. The efficiency plotted in Fig. 4.8(d) clearly shows the advantage of the wings with moderate flexibility. The optimal flexibility for all three mass ratios is around $\omega^* = 0.3$ to 0.35, where the peak efficiency is about $C_L/C_P = 0.62$ for $m^* = 5$, 0.70 for $m^* = 1$, and 0.74 for $m^* = 0.5$. These values are significantly higher than the efficiency in the rigid case, which has $C_L/C_P = 0.51$. At all frequency ratios except $\omega^* = 0$, the lift efficiency is increased as m^* is reduced. This result can be explained from the considerably low drag generated by the wing with a low mass ratio.

4.5 Advanced and delayed pitching

We have seen that in the present simulation, the chordwise flexibility increases the effective pitching angle of the wing. In addition, a high mass ratio leads to an advanced pitching motion with respect to the wing stroke, while a low mass ratio leads to a delayed pitching. Furthermore, we have shown that the timing of the passive pitching has an important effect on aerodynamic forces and power efficiency of the wing. These observations motivate us to vary the phase of the active pitching and then see if the wing deformation still has the similar effect, i.e., causing the pitching motion to be further advanced or delayed. This study is done by setting the phase angle in (4.1) to $\varphi = \pi/4$ for advanced pitching or $\varphi = -\pi/4$ for delayed pitching, which are typical values used in previous wing models (Wang *et al.*, 2004; Eldredge *et al.*, 2010).

The time-averaged lift, drag, power, and lift-to-power coefficients for both advanced and delayed pitching are plotted in Fig. 4.9 for mass ratios $m^* = 0.5$ and 5 and for a sequence of frequency ratios. Overall, advanced pitching leads to much higher lift, drag, and power than delayed pitching, and the symmetric pitching cases fall roughly between those for advanced and delayed pitching here. Moderate wing flexibility again significantly increase the lift regardless

87

the mass ratio. In addition, the wing flexibility at the low mass ratio leads to a much lower aerodynamic power than the rigid case, while the power consumption at the high mass ratio is comparable with that of the rigid case. As a result, all the flexible cases have higher lift-to-power efficiency than the corresponding rigid case, no matter the active pitching is delayed or advanced.

There are several common features among symmetric, delayed, and advanced pitching. First, the case of $m^* = 5$ has a little lower lift than the case of $m^* = 0.5$ at low frequency ratios but has a much higher lift at large frequency ratios. Second, the high mass ratio also corresponds to a higher drag and thus greater power requirement. Third, the net gain of $m^* = 5$ as measured by the lift-to-power ratio turns out to be lower than that of $m^* = 0.5$ for most of the cases. One exception is in Fig. 4.9(d), where for the case with $m^* = 5$ and delayed pitching, the power efficiency increases nearly monotonically as ω^* is raised and is even higher than that of $m^* = 0.5$ when $\omega^* = 0.51$. It can be found the passive pitching in this case has compensated the delayed active pitching, rendering an almost symmetric wing motion to generate larger lift. From our simulation results, symmetric pitching generally leads to the highest lift efficiency at constant mass and frequency ratios.
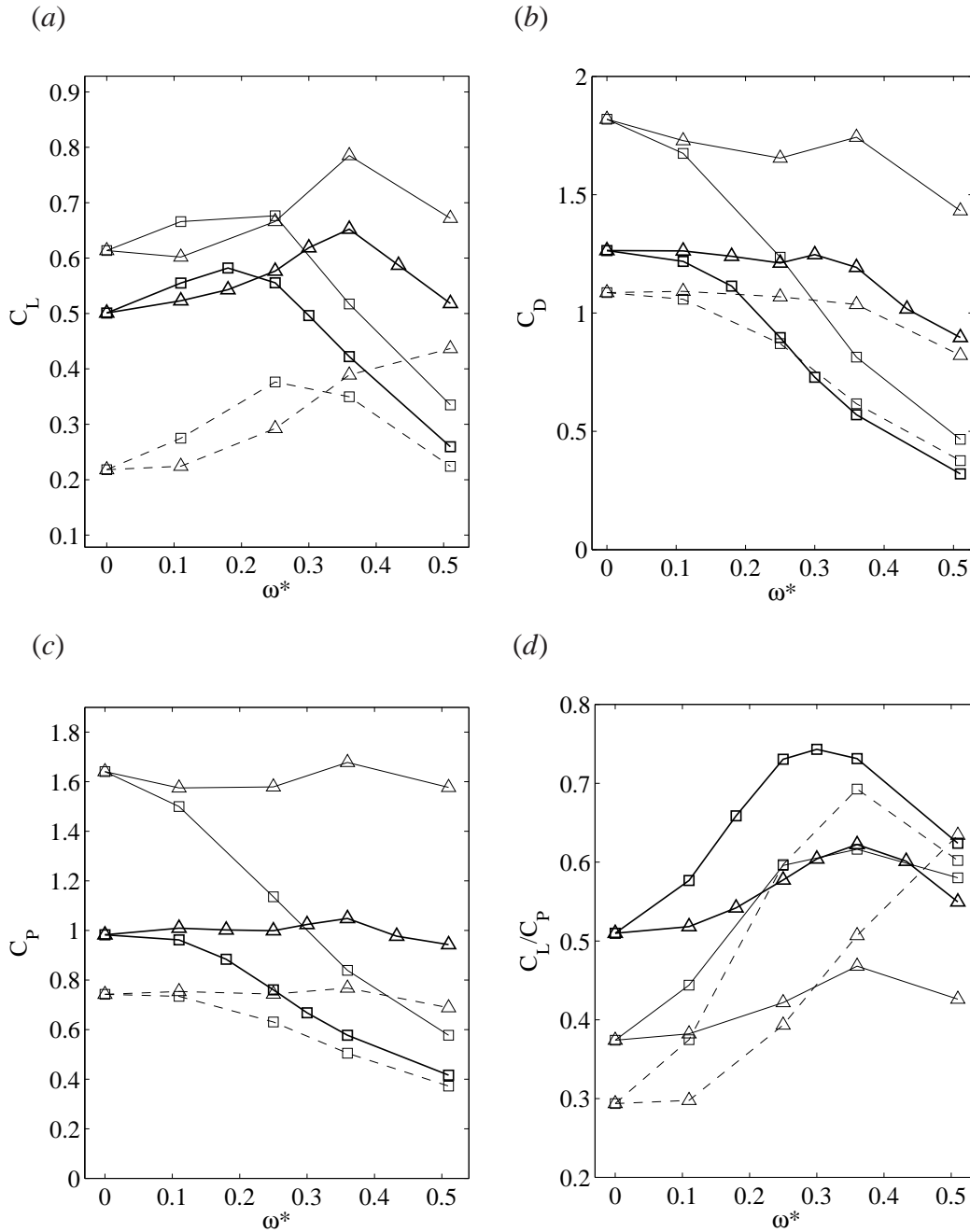
Figure 4.9: Mean lift (*a*), drag (*b*), power (c), and lift-to-power (d) coefficients for advanced (thin-solid lines) and delayed pitching (dashed lines) where $m^* = 0.5$ (squares) and $m^* = 5$ (triangles). The corresponding cases with symmetric pitching are re-plotted here as thick-solid lines for comparison.

4.6 Vortical structures

Vortex structures are visualized by plotting the isosurface of the maximal imaginary part of complex eigenvalues of the velocity gradient tensor, Λ_{max}. This quantity has been used previously to capture the topological flow patterns in a 3D flow field (e.g. Dong *et al.*, 2006). Figure. 4.10 shows the vortex evolution during a half cycle for the case of $m^* = 1$, $\omega^* = 0.36$, and $\varphi = 0$. From the flow field we can identify a few major vortical structures. First, the leading edge vortex(LEV) can be seen formed on the back side of the wing, and along the leading edge, it becomes stronger from the wing base to a location near the tip. The LEV is captured by the wing after the wing reversal and thus interacts with the wing. Second, a tip vortex (TV) is seen in the figure at, e.g., $t/T = 0.75$ and 0.85, which is formed at the tip edge of the wing and stretches into the wake as a long vortex filament. Third, a trailing edge vortex (TEV) is formed behind the wing and is connected to the trailing edge through a thin vortex sheet. In addition to these three major vortical structures, a vortex filament is formed around the base edge of the wing and also stretches into the wake; a semi-ring like vortex wraps around the tip vortex filament and is formed during wing reversal near the corner between the wing tip and the trailing edge. Termed BV and CV here, the last two vortical structures are largely affected by the particular choice of the rectangular wing shape in the current study. These vortices are connected to each other and form a vortex loop during wing translation. During wing reversal, these vortices would shed from the wing surface, except that a large portion of the LEV away from the tip would remain connected to the leading edge. Overall, the vortices pinched off from the wing travel in the negative z-direction along with the net downwash flow. The vortex loop seen here is a typical flow feature observed previously for low-aspect-ratio rigid flapping foils (e.g. Triantafyllou *et al.*, 2004; Taira & Colonius, 2009) (also see figure 2.14). One major difference in the present study is that the wing flaps by rotating around a pivot point, while

Figure 4.10: Vortical structures for $Re = 176$, $m^* = 1$, $\omega^* = 0.36$, and $\varphi = 0$ at $t/T = 0.5$ (stroke reversal), 0.6, 0.75 (mid-stroke), and 0.85. The contour level is $10U/c$.

in previous studies the wing motion is uniform along the span. As a result, the BV here is much weaker than the TV. Furthermore, since the present wing is perform a hovering motion and there is no freestream flow, the vortex loop is disrupted by the wing after reversal. For a pitching/heaving foil in a freestream, the vortex loops would be convected away from the foil, and those vortices from consecutive flapping cycles would be typically interconnected (e.g. Triantafyllou *et al.*, 2004).

In Fig. 4.11, we show the vortical structures in the flow for a rigid case and two flexible cases with $m^* = 0.5$, 5 and $\omega^* = 0.36$. Symmetric pitching is used in these cases. Both mid-stroke and wing reversal are shown. Overall, the major vortices in these three cases have a similar topology. Differences in the evolution and shedding of these vortices can be observed by inspecting the temporal series of the plots, and these differences are related to the dynamic deformation of the wing.

Fig. 4.12 shows the corresponding flow field in a horizontal plane and the spanwise velocity during mid-stroke for the rigid case and the case with $m^* = 0.5$ and $\omega^* = 0.36$. Comparing the two cases, we notice that for the rigid wing there is a consistent spanwise flow along much of the wingspan, while the spanwise flow is concentrated near the wing tip for the flexible wing. To explain the phenomenon, we point out that the warped surface of the flexible wing has an impedance effect on the spanwise flow. In addition, the larger deformation of the wing

91
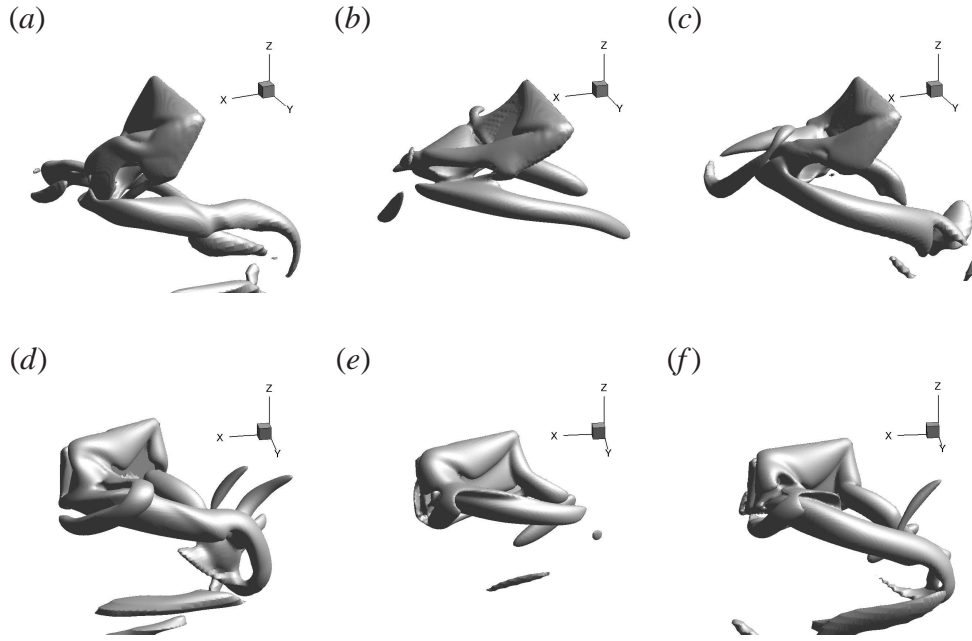
Figure 4.11: Vortical structures for (a,d) the rigid case, (b,e) $m^* = 0.5$ and $\omega^* = 0.36$, and (c,f) $m^* = 5$ and $\omega^* = 0.36$, $\varphi = 0$, and $Re = 176$ during (a-c) mid-stroke and (d-f) wing reversal. The contour level is $10U/c$.

tip reduces the difference in the actual velocity between the tip edge and the base edge. As a result, these is less need for the fluid to move toward the tip to compensate an otherwise void space created due to the wing displacement. To conclude, the 3D wing deformation may have a significant effect on the spanwise flow of a flapping wing.

4.7   Effect of the Reynolds number

To investigate the influence of the Reynolds number, we set $Re = 500$ and 1000 and run selected cases on the high-resolution grid discussed in the grid convergence test. At each Reynolds number, two simulations are run with $m^* = 1$ or 5 and $\omega^* = 0.36$. Figure. 4.13 shows the flow field for the case with $Re = 500$ and $m^* = 1$. In comparison with the low-Re cases presented earlier, this case contains a much more complex wake with randomly oriented vortices. Nevertheless, some major vortical structures such as the leading edge vortex and the long vortex
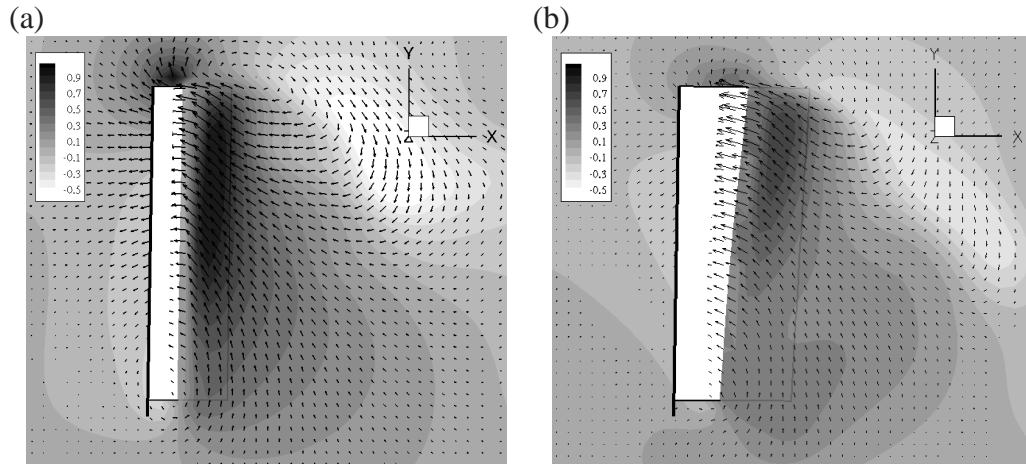
Figure 4.12: Top view of the velocity field in the plane $c/3$ below the leading edge (thick line) for (a) the rigid case and (b) $m^* = 0.5$ and $\omega^* = 0.36$, $\varphi = 0$, and $Re = 176$ during mid-stroke. Vectors at every three points are shown, and the contours represent the $y-$velocity component.
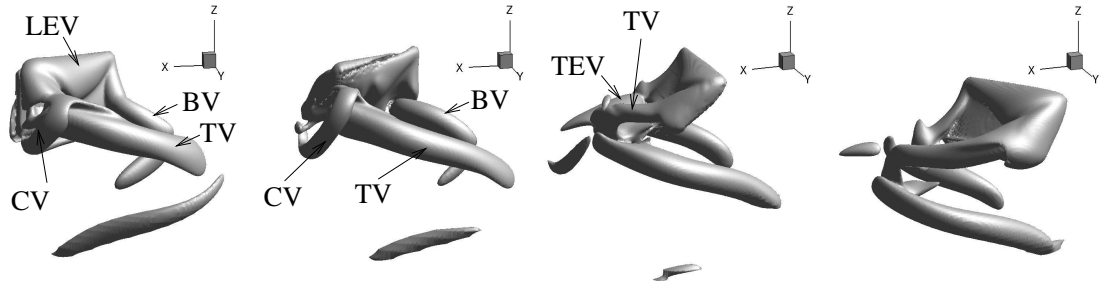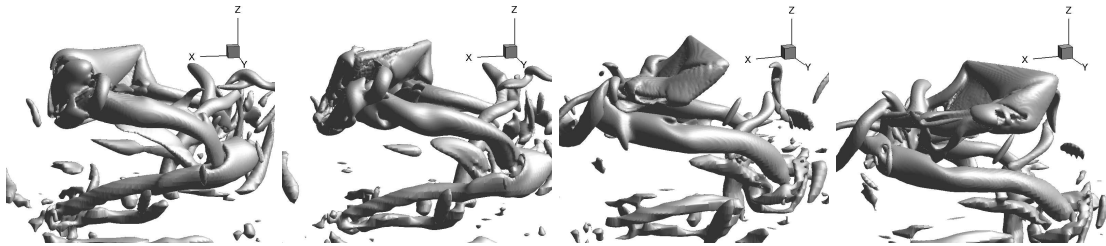

Figure 4.13: Vortical structures for $Re = 500$, $m^* = 1$, $\omega^* = 0.36$, and $\varphi = 0$ at $t/T = 0.5$ (stroke reversal), 0.6, 0.75 (mid-stroke), and 0.85. The contour level is $10U/c$.

filaments stretched from the tip vortex and the base vortex can be still clearly identified. The other major vortices develop finer-scale irregularities during their formation and once pinched off from the wing, they soon break up into smaller vortices spread in the wake. The effect of the Reynolds number on the wing deformation is found to be small. Especially for the high mass ratio, $m^* = 5$ the Reynolds number has only a slight effect on the dynamics of the wing due to the relatively low influence of the fluid forces.

The effect of the Reynolds number on the aerodynamic performance of the wing is summarized by the statistics in Table 4.1. Comparing the lift coefficient at the three Reynolds numbers

	Re	C_L	C_D	C_P	C_L/C_D	C_L/C_P
	176	0.54	0.83	0.78	0.64	0.69
$m^* = 1$	500	0.60	0.81	0.76	0.74	0.78
	1000	0.62	0.79	0.75	0.79	0.83
	176	0.66	1.23	1.07	0.54	0.62
$m^* = 5$	500	0.72	1.23	1.07	0.58	0.67
	1000	0.74	1.22	1.08	0.61	0.69

Table 4.1: Comparison of the aerodynamic performance at different Reynolds numbers, where $\omega^* = 0.36$ and $\varphi = 0$.

from $Re = 176$ to $Re = 1000$, we see that there is a 16% increase in C_L for $m^* = 1$ and 12% for $m^* = 5$. For the drag and power coefficients, varying the Reynolds number has only a slight effect on the data. As a result, both the lift-to-drag and the lift-to-power ratios have increased as Re is raised. Specifically, for $m^* = 1$, C_L/C_D and C_L/C_P have grown by 22% and 19%, respectively, as Re goes from 176 to 1000. while for $m^* = 5$, the increments are by 13% and 11%, respectively. Finally, we compare the two mass ratios at the same Reynolds number, and we notice that the $m^* = 5$ case has consistently higher lift and drag than the $m^* = 1$ case but meanwhile the former has lower aerodynamic efficiency.

4.8   Conclusion

Here we have performed a three-dimensional simulation of the fluid–structure interaction of a low-aspect-ratio rectangular wing performing a hovering-type of flapping motion. The wing surface is clamped to a rigid leading edge and is otherwise free to deform. The simulation shows that the chordwise deformation of the wing causes a dynamic pitching in addition to the active pitching applied at the wing root. The aerodynamic performance of the wing is affected not only by the increased pitching amplitude due to the deformation but also by the phase and rate of the passive pitch.

Other than the specified kinematics at the wing root and the stiffness of the wing, the dy-

namic pitching also largely depends on the mass ratio, which represents the relative importance of the wing inertia and aerodynamic forces in the wing deformation. At high mass ratios where the inertial torque is dominant, a phase advance is produced in the effective pitching angle during stroke reversal by the wing deformation, while at low mass ratios where the aerodynamic torque becomes equally important, a phase delay is produced during stroke reversal. During wing translation, the rate of passive pitch varies due to the combined inertial acceleration, elastic recovery, and in the case of low mass ratios, aerodynamic damping.

When $\omega/\omega_n \leq 0.3$, the wing deformation significantly enhances the lift production and also improves the lift efficiency although a disadvantageous camber is formed during wing stroke. In particular, when the inertial pitching torque near wing reversal is assisted by an aerodynamic torque of comparable magnitude during wing translation, the lift efficiency can be markedly improved. This result thus confirms the insightful hypothesis by Ennos (1988a). Furthermore, the performance of the flexible wing is found to be consistent for different phase angles of active pitching and Reynolds numbers.

In the present study the wing-root kinematics is fixed. In the real world, insects with different wing stiffness and mass ratios could achieve their best performance by optimizing the wing-root kinematics. The wing deformation in this study is also largely limited to chordwise bending since the leading edge is rigid.

CHAPTER V

AN INTEGRATED STUDY OF THE AERODYNAMICS AND AEROELASTICITY OF

THE CICADA FOREWING

5.1   Background

The membranous wings of insects are very thin structures (typically less than 100 μm in thickness). Nevertheless, these wings have to endure the forces of large magnitude which are generated during their high-frequency flapping motion. For example, blowflies are capable of producing up to 2 *g* of horizontal acceleration and 1 *g* of vertical acceleration in flight (Schilstra & Hateren, 1999), which means that the aerodynamic force on the wing can be twice as great as the body weight of the insect. Reinforced by a vein network and other structural features such as the surface corrugation and camber, the insect wings have an excellent design that provides the necessary stiffness and is meanwhile mass efficient. However, the insect wings are not meant to be as rigid as possible with given mass, as pointed out by Ennos (1988*a*). Allowing certain amount of deformability could reduce the impact load from environmental disturbances (e.g., running into a solid object or wing gust). In addition, the deformation could be beneficial to the aerodynamics of the wing as well. This function has been suggested by several previous studies (Walker *et al.*, 2010; Young *et al.*, 2009; Yin & Luo, 2010) and our own studies presented in previous chapters.

Identifying the structural mechanism and the physical effect that leads to the wing deformation is important for guiding modeling of the aeroelasticity of insect wings. First, wing deformation of an insect is passive, and it may be caused by either the inertial force of the wing,

the aerodynamic force from the surrounding air, or a combination of both. Several studies have addressed the cause to the deformation and its particular pattern. Ennos (1988*b*) measured the mass distribution of the wings of two species of flies and showed that the wing inertia alone could develop the angular velocity around the torsional axis of the wing that is observed at stroke reversal (assuming the torsional axis to be compliant enough to allow such a rotation). Ennos (1988*a*) then used a simple static analysis to study the mechanical behavior of a model insect wing consisting of a few veins branching from the leading edge, and he also subjected the wings of three species of flies to static point-force tests. Several important conclusions were made from his study. First, torsion of the leading edge spar would result in spanwise twist of the wing and also set up a camber automatically due to the corresponding rotational responses of the obliquely arranged vein branches. As for the conventional airplane wings, the camber formed by the wing deformation would be favorable for lift production. Second, he estimated that the aerodynamic forces produced during the wing strokes (assumed to be at the same magnitude as the body weight of the insect) will be sufficient to generate the observed torsion and camber, and to maintain the changes in pitch caused by inertial effects at stroke reversal. In another study, Combes & Daniel (2003*b*) compared vibrations of the excised hawkmoth wing in air and in helium (15% of the air density) and noticed that the deformation patterns in the two cases are close to each other. Their result suggests that the hawkmoth wing is mainly deformed by the wing inertia during stroke. For some other insects, however, evidences suggest that aerodynamic forces can be at least comparable, if not dominant, to the wing inertia, as discussed in our recent work (Yin & Luo, 2010; Dai. *et al.*, 2012). If the aerodynamics forces are significant in determining the wing dynamics, then a two-way fluid–structure interaction (FSI) has to be solved to capture the deformation of the wing in a computational study.

As the computing power and experimental techniques have advanced in recent years, further

97

studies are carried to investigate the effect of the wing deformation on the aerodynamic performance. These computational (Zhu, 2007; Michelin & Llewellyn Smith, 2009; Vanella *et al.*, 2009; Eldredge *et al.*, 2010; Yin & Luo, 2010; Dai. *et al.*, 2012) and experimental (Prempraneerach *et al.*, 2003; Heathcote *et al.*, 2004, 2008) studies typically use heaving and pitching foils as simplified wing models, and they have shown that that wing flexibility may lead to significant benefit to the aerodynamic force production and power efficiency. A study that uses a more realistic insect model is by Young *et al.* (2009), who performed a full-body numerical simulation of the forward flight of locusts by incorporating the wing kinematics reconstructed from high-speed imaging. For comparison, they also performed flight simulations based the modified wing kinematics by removing the camber and spanwise twist from the full-fidelity wing motion. One major limitation of this study is that the fluid–structure interaction is excluded from the study. Furthermore, the effect of the wing deformation is limited to static features such as camber and spanwise twist. For flapping wings, since the wing shape is time-varying, it is expected that the dynamic deformation may also play a role in the aerodynamics. In our previous work, Dai. *et al.* (2012) used a rectangular wing in hovering motion and showed that not only the amount of wing deformation, but also the rate and phase of the deformation, lead to marked differences in the aerodynamics of the wing.

Having discussed the causes of the wing deformation and the multiple manners in which the wing deformation affects the aerodynamics, we note that there have been very limited attempts to simulate the fluid–structure interaction using a realistic insect wing model that incorporates the inhomogeneous and anisotropic behavior of the wing. There are possibly two major reasons for this shortage of study. First, such a study would be very challenging due to the high cost associated with the moving boundary, large displacement, and iteration for solving the fluid and structure. Second, it remains an open question what kind of balance is appropriate between the

model complexity and the computational cost that one could afford. Note that the insect vein itself has a complex microstructure which strongly affects its macro properties (Ren & Wang, 2012). Furthermore the wing is not an ideal 2D planar surface but have complex corrugations. Including all these details into the wing structure obviously would not only require strenuous effort and but also render a model that is very difficult to compute. It is therefore our goal in the current work to address both these two issues.

As discussed in previous chapters, we have developed a three-dimensional numerical approach to simulate the interaction between a viscous unsteady flow and deformable thin structures. The in-house code features a flow solver based on the Cartesian grid immersed-boundary method and a finite-element solver that incorporates a variety of structural types such as frame, membrane, and plate elements. The program is particular suitable for modeling insect wings. In the current work, this numerical method will be integrated with an experimental approach to model the aerodynamic function of a full wing. More specifically, we use the cicada forewing as a case study. A nonlinear finite-element model is developed based on the experimental measurements of the mass and elastic properties of the structural elements, i.e., the membrane and veins. In addition, a high-speed camera is used to film the wing motion for the tethered insect. The wing-root kinematics is reconstructed from the video, and the deformation pattern observed from the video is used to validate the simulated wing dynamics from the FSI model. The work described here is the first attempt, at our best knowledge, that utilize such an integrated approach to develop a high-fidelity model for the aerodynamics and aeroelasticity of flapping wings in nature. We envision such a computational tool and the modeling methodology will become very useful for the future studies of insect flight and for the development of man-made biomimetic aerial vehicles.

5.2   Some discussions of the scaling parameters of the insect wing

Leaving out the details of the surface corrugation and the distribution and orientation of the veins, the bulk wing surface can be approximated as a homogeneous and isotropic plate. The basic dimensional parameters involved in the FSI problem include the density of the wing material, ρ_s, wing thickness, h, Young's modulus, E, a characteristic length such as the chord length, c, wing length L, fluid density, ρ_f, viscosity μ, and flapping frequency f or $\omega = 2\pi f$. Note that if the wing is approximated by an infinitely thin plate with equivalent mass and stiffness, the thickness ratio, h/c, does not have to show up in the dimensionless groups, as the surface density can be normalized as $m^* = \rho_s h/(\rho_f c)$, as in the previous chapters. The mass ratio is defined to roughly represent the relative importance of the inertial force of the wing per unit surface area with respect to the dynamic pressure. For flexible wings, $m^* \gg 1$ corresponds to the situation where the wing deformation is dominated by the wing's own inertia. On the other hand, $m^* \ll 1$ corresponds to the situation where the deformation is caused mainly by the fluid force. Experiments done in air (e.g. Ramananarivo *et al.*, 2011) typically falls in the former situation, while those in water (e.g, Heathcote *et al.*, 2008) is the later situation due to the much higher density of water.

In the context of insect flight, we can define the mass ratio as follows. A wing with a length of L flapping in an angular magnitude of Φ and frequency of f has a mean tip velocity $U = 2L\Phi f$, and a mean tip acceleration $a = 4\pi\Phi f^2 L$, then the ratio of the inertial force to the fluid force on a unit area at the wing tip, or the mass ratio, is expressed as

$$\frac{\rho_s h a}{\frac{1}{2}\rho_f U^2} = \frac{\rho_s h 4\pi\Phi f^2 L}{\frac{1}{2}\rho_f (2L\Phi f)^2} = \frac{2\pi\rho_s h}{\rho_f L\Phi} \tag{5.1}$$

To scale the flexural stiffness of the wing, either the dynamic pressure or the inertial force of the wing can be used, since the elastic force would balance these two external forces. In previous

chapter, we showed that for $m^* = 0.5$ such as fruitfly wings (Ennos, 1988b; Dai. *et al.*, 2012), the aerodynamic pitching torque is comparable in magnitude to the inertial torque of the wing, and for larger m^* like dragonflies (Chen *et al.*, 2008; Dai. *et al.*, 2012) and hawkmoths (Combes & Daniel, 2003b; Dai. *et al.*, 2012), the inertial torque is greater. Thus, it is appropriate to scale the bending stiffness, EI, $I = h^3/12$, using the inertial force, $\rho_s hU^2/c$, and a dimensionless group, $EI/(\rho_s hU^2 c^2)$, would be formed. If $U = cf$ is used and we take the inverse of the square root of this dimensionless parameter and then multiply it by a constant, we get the frequency ratio, $\omega^* = f/f_n$, where $f_n \propto 1/c^2 \sqrt{EI/(\rho_s h)}$ is the natural frequency of the first mode of the chordwise bending. In the context of insect wings, ω^* is between 0 and 1, where $\omega^* = 0$ corresponds to a rigid wing and $\omega^* = 1$ corresponds to the case in which the wing flaps at its resonant frequency to cause large deformation. It should be noted that several recent studies (Vanella *et al.*, 2009; Yin & Luo, 2010; Ramananarivo *et al.*, 2011) have suggested that insect wings should operate at significantly lower frequencies than the resonant frequency since the overly large deformation is not beneficial for force production.

The mechanics of the vein branches could be analyzed using simplified cylindric beam model. A beam element is characterized by the length, l, linear density, $\rho_s A$, where A is the area of the cross section, the bending stiffness, EI_{yy}, where I_{yy} is the second moment of area about the symmetry plane, and the torsional stiffness, GJ, where G is the shear modulus and J is the torsional constant. The frequency ratio $\omega^* = f/f_n$ can again be used to represent the normalized flexibility of the beam structure. The natural frequency of bending deformation is $f_n \propto 1/l^2 \sqrt{EI_{yy}/(\rho_s A)}$, and the natural frequency of torsional deformation is $f_n \propto 1/l \sqrt{GJ/(\rho_s I_{zz})}$, where I_{zz} is the polar moment of inertia of area of the cross section.
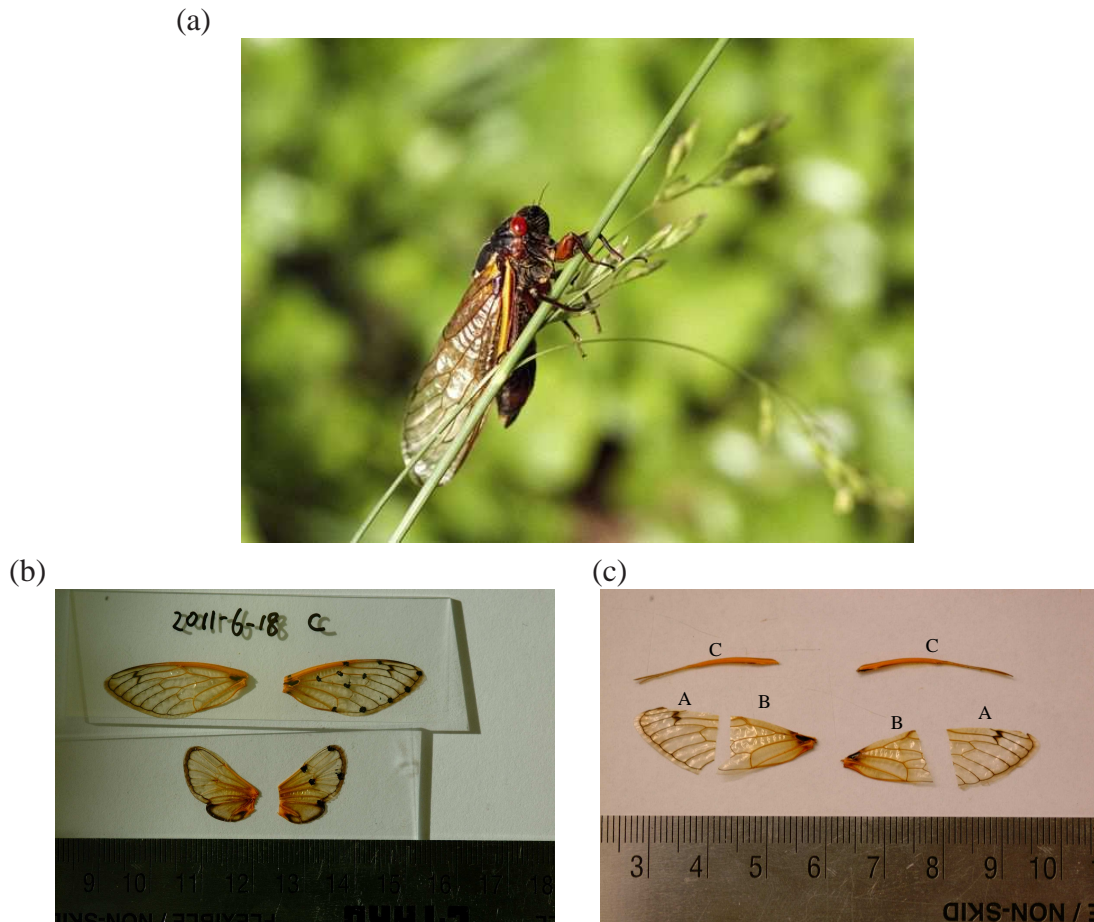
Figure 5.1: (a) The magicicada used in this study. (b) Forewings and hind wings removed from the cicada, where the markers are labeled for the imaging experiment. (c) The forewing is sliced into three parts for mass measurement.

Wing length (L)	Chord width (c)	Flapping frequency (f)	Stoke amplitude (Φ)
3 cm	0.76 cm	25 Hz	120°

Table 5.1: The characteristic geometric and kinematic data of the cicada forewing.

5.3 Measurement of the elastic properties of the cicada wing

The subjects used in this study are the periodic 13-year species of *Magicicada tredecassini* (Brood *XIX*) captured in the summer of 2011 when a large population of the species emerged in the middle Tennessee (Fig. 5.1(a)). The average body weight of Magicicada tredecassini is 185 mg based on a sample of around 50 individuals by a report from Ginger Rowell and

Wing portion	A	B	C	C (base)	C (tip)
Mass (mg)	1.28±0.11	2.60±0.33	3.04±0.68	1.7	0.35
Area/linear density	0.9	2.6	–	1.7	0.35

Table 5.2: Mass of each part from the cicada forewing. The unit of the area density is mg/cm^2, and the unit for the linear density is mg/cm.

Robert Grammer in Belmont College. The characteristic data of the insect's forewing are listed in Table 5.1. To obtain the mass distribution, each of the forewing samples is sliced into three parts: the distal half (A), the proximal half (B), and the leading-edge spar (C), as shown in Fig. 5.1(b). Each part is measure separately. The leading-edge spar is further split into two segments: a distal segment and a proximal segment, each segment being 1 cm long. The mass of each part is measured by an electronic balance with an accuracy of 0.1 mg. For the two leading-edge segments, 10 samples of each segment are measured together. Images of the two wing surface parts are taken and imported into Matlab, and their areas are calculated by tracing the boundary. The average mass of each part, the area density of parts A and B, and the linear density of the leading-edge segments are then calculated. The data are listed in Table 5.2. The mean chord length, $c = S/L$, where S is the total surface area, of a typical wing is 0.76 cm. Using Eq. (5.1), the mass ratio of the distal area is around 0.85. For the calcualtion, we have used $\Phi = 120°$, L=3 cm, and ρ_f=1.2 mg/cm^3. This mass ratio implies both the inertial and fluid forces are important in causing the wing deformation. Therefore, two-way coupling is necessary in the study of the fluid–structure interaction in this case.

The flexural stiffness of veins and membrane surface is measured on the samples excised from the wings. The samples are selected from various sites on the wing according the distribution and orientation of the veins. These samples are shown in Fig. 5.2(a), where 6 pieces from each forewing are taken and labeled as F1 to F6. All of them are sliced into roughly rectangular pieces with a length of approximately 5 mm. For each piece, a total of 5 samples are used for

measuring the bending stiffness, which is done through a sequence of static load tests. Note that specimen F6 is used for measuring the bending stiffness of the membrane, so the bending is applied in the perpendicular direction to the veins in the specimen. The samples are glued to a glass cover slip, as shown in 5.2(b). Then the cover slip is secured using a magnet on a horizontal beam attached to a micrometer stage that can translate vertically. The load is measured from the same electronic balance as used in the mass measurement. The experimental setup is shown in Fig. 5.3. The specimen on the cover slip is translated down by the micrometer stage so that it touches the support on the balance. Then the micrometer stage is further translated, each time by 0.2 mm, and the force reading on the balance is recorded. Each sample is measured from both ventral and dorsal sides to average out the directional difference. The beam equation is used to calculate the stiffness of each vein and the membrane. The data from the experimental tests are listed later in Table 5.3 along with the values chosen in the FEM model.

5.4   Creation of the finite-element model

In this study, only one forewing of the cicada is modeled, and the insect body is not included in the simulation. The finite-element model of the forewing is constructed with a thin membrane structure reinforced by a network of frame elements with which it shares mesh nodes. A similar modeling approach is seen in Wootton *et al.* (2003) who created finite-element models for the desert locust and sphingid moth wings. In the current model, the membrane is assumed to be homogeneous and isotropic. The veins are traced in Matlab from a stationary image of the wing, and they are grouped into seven levels, each with a different diameter, linear density, and bending stiffness. The cross section of the veins is assumed to be circular. Generally, the veins close to the wing root and the leading edge are larger in size, and the veins distributed around the trailing edge and near the tip are weaker structures and are thus subject to larger deformations.
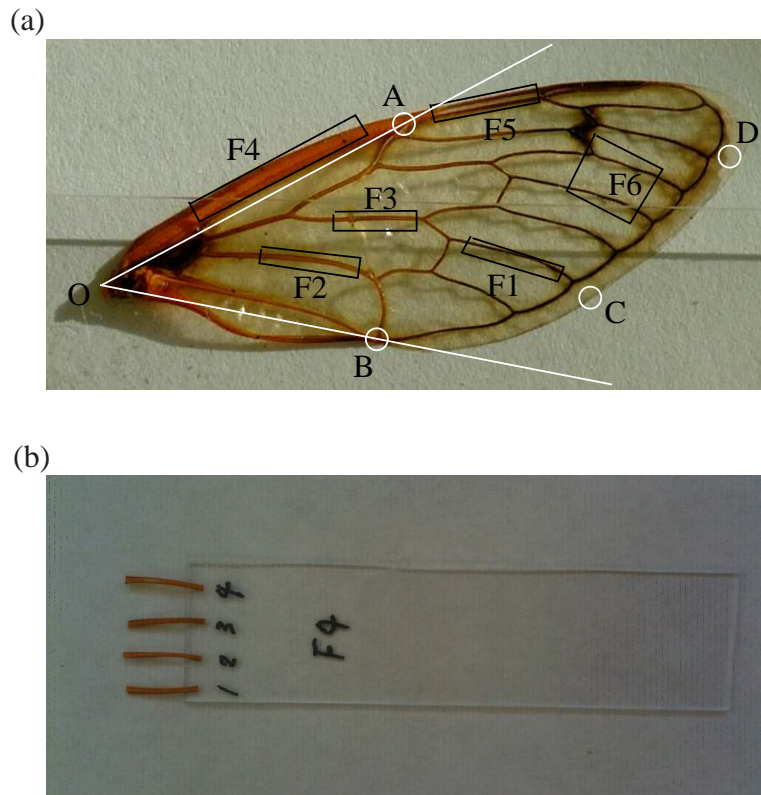
Figure 5.2: Measurement of the bending stiffness of the representative components from the cicada forewing. (a) Representative components chosen for measurement. Note that F6 will be used for measuring the bending stiffness of the membrane without the vein effect. (b) Attachment of the samples on a cover slip for the static load test. In (a) some points are marked with white circles, which include point A on the leading edge, point B at the trailing edge and closer to the root, point C on the trailing edge and closer to the tip, and point D at the wing tip. The pivot point is labeled as O. As discussed later, these points are used in description of the wing kinematics.

Fig. 5.4(*a*) illustrates the grouping of the veins for the current wing model.

Like many other insect wings, a pre-existing camber is clearly observed on the cicada forewing at rest. In the present model, we measured the maximum camber by placing the wing on a flat surface and probing the surface using the micrometer stage. Then distribution of the camber is prescribed according the characteristic feature of the wing. The contours of the camber is shown in Fig. 5.4(b), where the contours are assumed to be elliptical. The greatest camber occurs at the wing center with a height of around 10% of the chord length. The camber is concave on the ventral side.

Figure 5.3: The experimental setup for stiffness measurement.
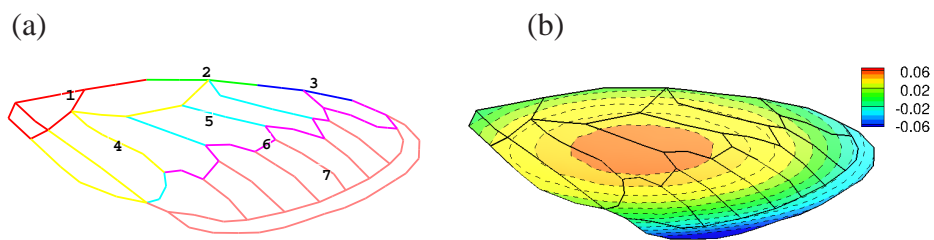
Figure 5.4: The FEM model of the cicada forewing. (a) The vein groups on the wing surface. (b) The contours of the pre-existing camber.

Table 5.3 lists the measured stiffness and the values chosen in the wing model for the vein groups and the wing membrane. Also listed are the assignment of the linear density of the vein groups and the surface density of the membrane. Assuming that the cross section of the veins is circular, the torsional stiffness can be simply calculated based on the bending stiffness.

Component groups	Experimental data	Value in the model		
	EI	EI	GJ	linear/surface density
Vein 1	-	5500	11000	1.33
Vein 2	275 ±104	275	550	0.46
Vein 3	21.7±12.1	22	44	0.29
Vein 4	10.5±5.5	10.5	21	0.29
Vein 5	4.3 ±2.8	4.3	8.6	0.17
Vein 6	-	0.5	1.0	0.11
Vein 7	0.37±0.15	0.37	0.74	0.023
Membrane	0.47±0.14	0.47	-	0.40
Total mass				6.4 mg

Table 5.3: Bending stiffness of the veins and membrane stiffness. (Unit: 10^4 mg·cm^3/s^2 for the vein stiffness, 10^4 mg·cm^2/s^2 for the membrane stiffness, mg/cm for the linear density of the vein and mg/cm^2 for the surface density of the membrane.)

Figure 5.5: The experimental setup for high-speed imaging of the wing motion.

5.5   High-speed imaging and reconstruction of the wing kinematics

For the high-speed imaging experiment, a cicada with the hindwings removed is glued on

a vertical pole and is stimulated to flap, and a high-speed camera from Dr. Jon Edd's Lab at
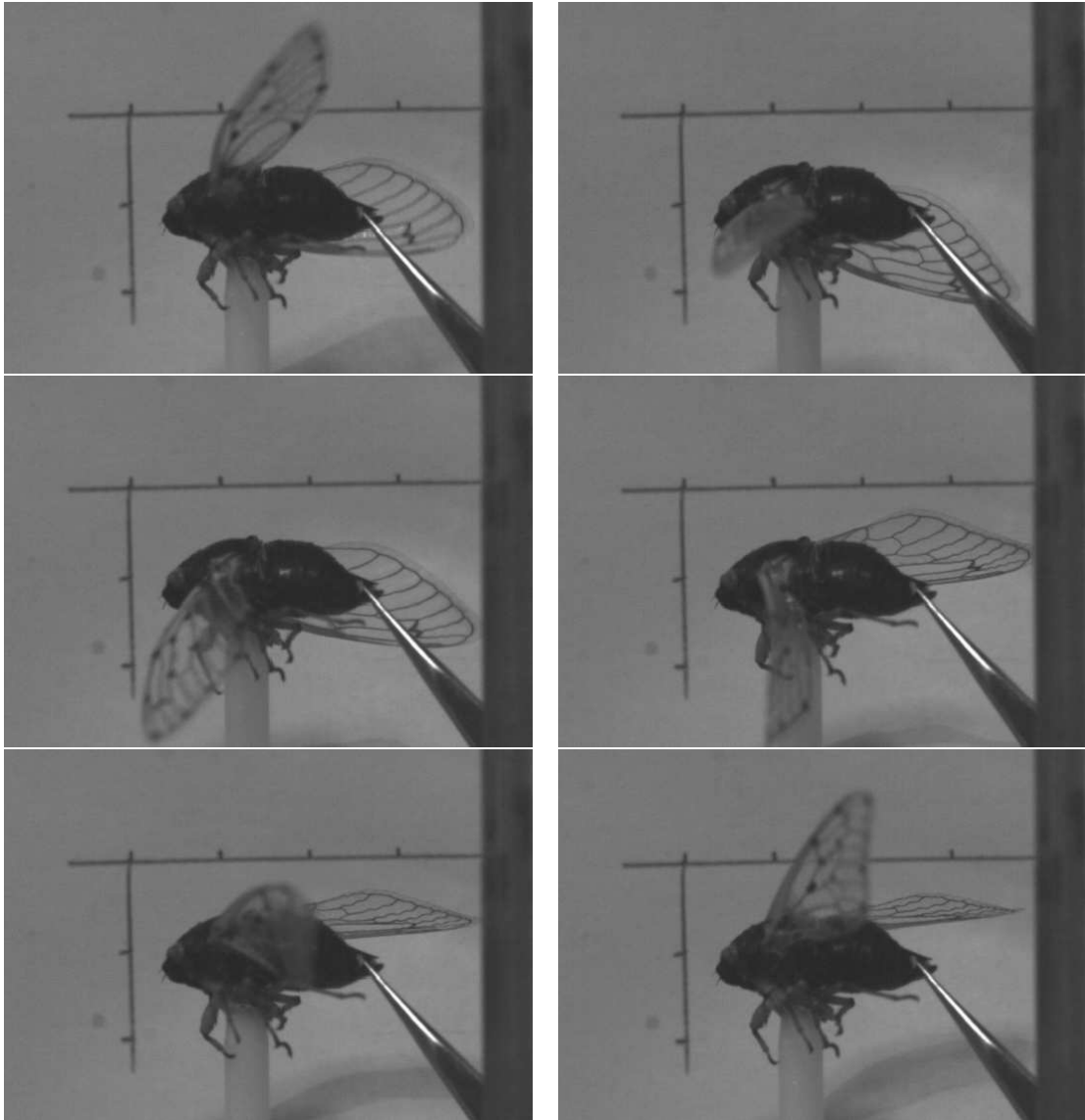
Figure 5.6: High-speed recording of the wing deformation pattern of a cicada tethered to a pole. The interval on the background scale represents 1 cm length. Significant spanwise twist can be observed during first half of upstroke.

Vanderbilt University is used to film the insect at 1000 frames per second from a side view. The

experimental setup is shown in Fig. 5.5. The wing being filmed is pre-labeled with markers.

Fig. 5.6 shows a typical sequence of the deformation pattern as the cicada flaps its wings.

Ideally, it is sufficient to use only one camera to reconstruct the motion of a rigid wing rotat-

ing in 3D space based on a 2D view and the known distance between any two points. However,

one camera is not enough to achieve full reconstruction of a deformable surface. The attempt of using only one camera to film from different views at different times for 3D reconstruction is unfruitful due to the cycle-to-cycle variations of the wing motion. The common technique to film and reconstruct a real insect wing is to set up multiple cameras to simultaneously take images, by which the 3D position of any visible point could be extracted accurately (Koehler *et al.*, 2012).

In the present work, we only need to reconstruct the actuation kinematics at the wing root, where the wing is much stiffer than the rest part of the wing and experiences little deformation. Therefore, one camera is sufficient. Once the high-speed videos are taken, the markers on the wing surface can be traced conveniently using the Matlab software developed by Dr. Tyson Hedrick at the University of North Carolina at Chapel Hill (Hedrick, 2008).

We track three points near the wing root (one at the root, one on the leading edge, and one on the trailing edge) as shown in Fig. 5.2. Assume this portion of the wing is rigid, and the distances among these three points are measured after the imaging experiment. The 3D positions of these points can be reconstructed from the 2D images as discussed later. The other points on the deformable portion of the wing surface cannot be reconstructed in 3D, but their 2D positions will be used to validate the fluid–structure simulations. Around 40 frames are obtained for each flapping cycle, which corresponds to a flapping frequency around 25 Hz (from 23 Hz to 28 Hz according to our measurements).

Fig. 5.7 shows the measured and reconstructed trajectories of the two points on the wing in a selected cycle from which the periodic motion is constructed for numerical simulations. In the reconstruction the wing is assumed to rotate around a pivot point, and the three Euler angles are calculated from the measured data. In Fig. 5.7, the reconstructed points match the experimental data very well.
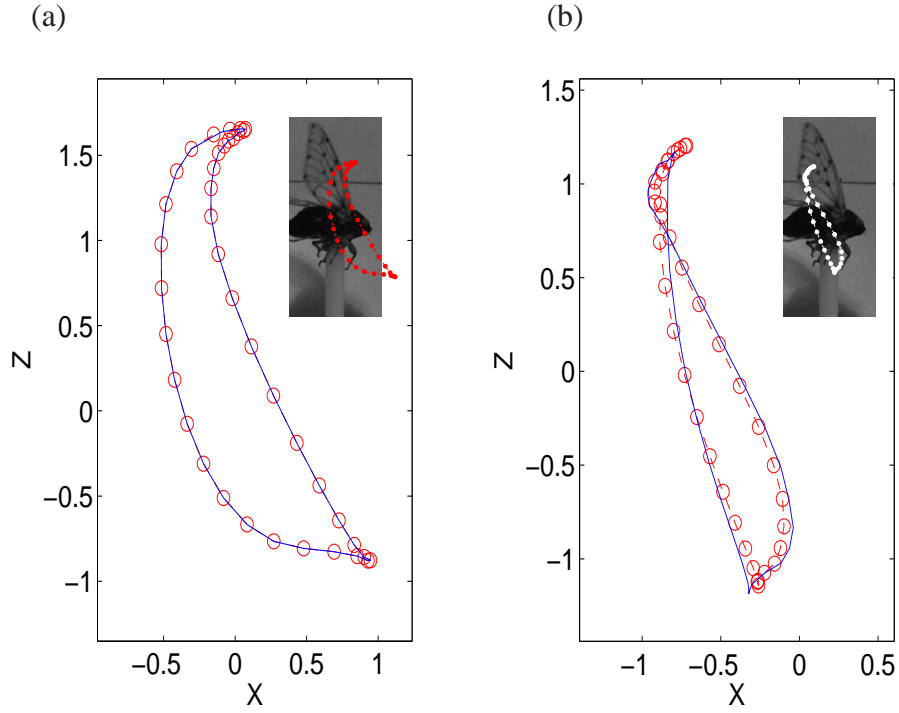
Figure 5.7: (a) Trajectory of point A as labeled in Fig. 5.2(a); (b) trajectory of point B as labeled in Fig. 5.2(a). The circles are the measured data. The blue curves are reconstructed trajectories.

The stroke plane is defined as the plane spanned by the highest and the lowest positions of the wing axis. As in the experiment, the insect body is fixed horizontally in the model. So the stroke plane is a slightly inclined backward. Once the 2D positions of point A or point B is obtained from the video, we use the actual distance of the point to the pivot point to calculate the corresponding 3D positions. As illustrated in Fig. 5.8(a), given two coordinates x and z (extracted from the 2D video), the third coordinate y of point A can be found if the actual distance to the root $AO = l$ is measured,

$$y = \sqrt{l^2 - x^2 - z^2}.$$

(5.2)

As long as the coordinates of point A and point B are known, the three angles, the stroke

110

angle, the deviation angle, and the pitch angle, can be calculated. As shown in Fig. 5.8(b) the stroke plane is defined by the two extreme positions of the leading edge, OH and OL. The position of the leading edge, OA, is first projected to OB in the stroke plane, where B is calculated by

$$\overrightarrow{OB} = \overrightarrow{OA} - (\overrightarrow{OA} \cdot \mathbf{n})\mathbf{n}, \tag{5.3}$$

where $\mathbf{n}$ is the surface normal of the stroke plane. Then the angle α between OB and OH, defined as the stroke angle, is calculated by

$$\cos\alpha = \overrightarrow{OB} \cdot \overrightarrow{OH}/(|OB||OH|), \tag{5.4}$$

and the angle θ between OB and OA, defined as the deviation angle, is found by

$$\cos\theta = \overrightarrow{OA} \cdot \overrightarrow{OB}/(|OA||OB|). \tag{5.5}$$

Finally, the pitch angle is introduced to specify the self-rotation of the wing around its leading edge using the convention that the wing surface perpendicular to the stroke plane gives a zero pitch angle. The histories of these angle reconstructed as discussed above are shown in Fig. 5.9 for a few flapping cycles. The average stroke amplitude is roughly $120°$. There is a $50°$ maximum deviation angle indicating the wing moves behind the stroke plane during upstroke. The pitch angle can reach $100°$. One typical cycle of these angle histories is selected as the periodic input for the numerical simulation.
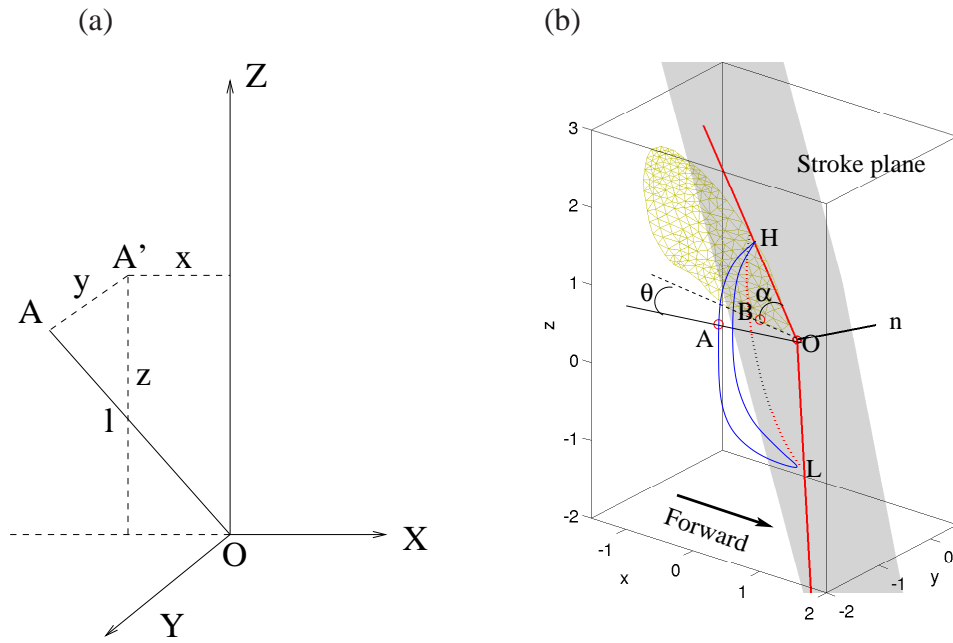
Figure 5.8: (a) Calculation of the 3D coordinates from 2D images used for the reconstruction of the wing-root actuation. (b) Definition of the angles used to describe the wing actuation kinematics.
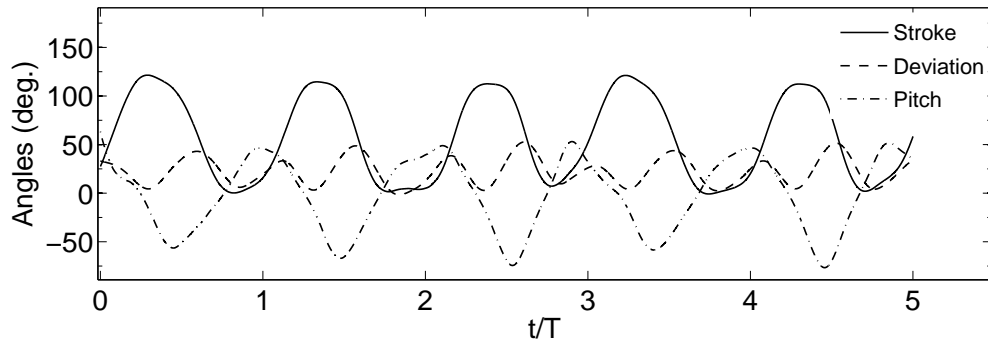
Figure 5.9: The stroke angle, the deviation angle, and the pitch angles as reconstructed from the high-speed imaging data for five flapping cycles.

5.6   Simulation results and discussions

5.6.1   Eigenmodes of the cicada forewing

The single wing simulations are run in a flow domain of $21c \times 18c \times 22c$ where c is the average chord length of wing, using a grid of $136 \times 128 \times 158$ (2.8M) points. The finite-element wing model is first analyzed numerically by computing its natural modes. The first mode takes

112
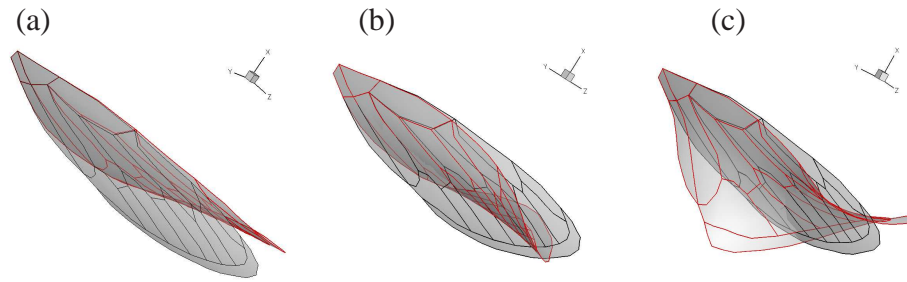
Figure 5.10: The first three eigenmodes calculated from the cicada forewing model. The rest configuration is drawn in black together with the eigenmode shown in red. The eigenfrequencies are 192, 306 and 466 Hz, respectively.

place at 192 Hz, and as shown in Fig. 5.10(a), the mode displays a spanwise twist that mainly

happens at the distal half of the wing. This mode is qualitatively similar to the deformation

mode seen in the high-speed video. The second mode shows chordwise bending deformation

and takes place at 306 Hz. The third mode has a higher-order warping pattern and takes place at

466 Hz. Note all of these modes have much higher frequencies than the flapping frequency of

the wing (25 Hz). Therefore, we can conclude the structural resonance is not dictating the wing

deformation.

5.6.2   Validation of the FSI simulation

A few cycles of the FSI simulation are performed. We first discuss the validation of the

present computational model. For the validation, we compare the simulated trajectory of a point

on the wing with that obtained quantitatively from the high-speed imaging data. Fig. 5.11(a,b)

shows the trajectories of point C and point D labeled on the wing. As indicated in Fig. 5.2(a),

point C is located on the trailing edge, while point D is located at the wing tip. The trajec-

tories in Fig. 5.11(a,b) are in a 2D view (since only 2D images were taken from the imaging

experiment). In Fig. 5.11(a,b), we see that the simulated trajectories match the measured trajec-

113
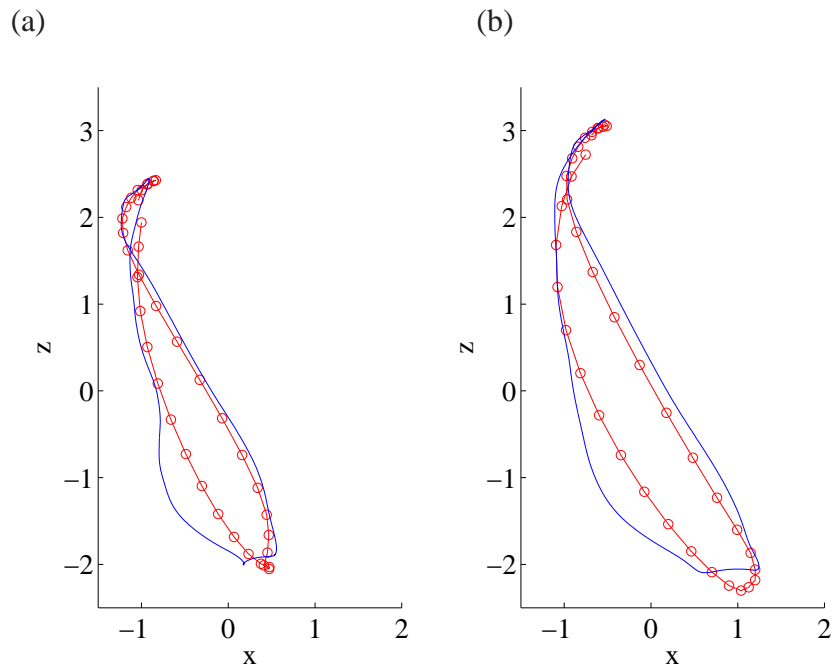
Figure 5.11: Comparison of the simulated and the measured wing trajectories. The 2D trajectory is plotted for (a) point C and (b) point D, which are labeled in Fig. 5.2(a). Red lines are the data points from the imaging experiment, and the blue lines are the simulation data.
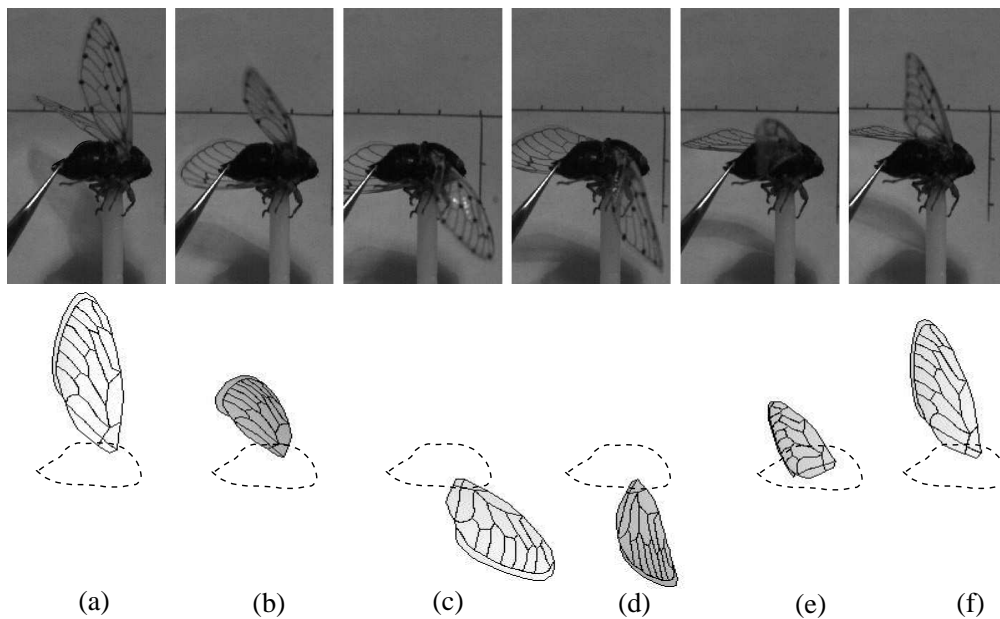
Figure 5.12: A comparison between the simulated and the filmed wing shapes. The time stamps are t/T =1/38, 13/38, 22/38, 26/38, 34/38, and 37/38 from left to right.

tories well during downstroke. However, significant discrepancy can be seen during the early upstroke, where the simulated trajectories deviate somewhat from the measured data. Next, we will compare the deformation pattern at different phases.

The wing shapes at a few time moments are compared qualitatively in Fig. 5.12. These images from the imaging experiment show that during downstroke (a-c), the wing deformation is not very clear. However, during upstroke (d-e), the wing experiences significant bending and twisting deformations. These essential features have been captured by the numerical simulation. There are still some notable differences between the simulation and the images. For example, in Fig. 5.12(d) the real wing exhibits some chordwise bending so that the dorsal surface is concave. This feature is not present in the simulated deformation. Another place is in Fig. 5.12(f), the wing-tip area in the simulation has nearly recovered from its deformation, but the the trailing edge of the real wing near the tip still shows some twisting. Several factors could have contributed to these differences. First, the distal half of the wing is assumed to be rigid during the wing-root reconstruction. However, point B in Fig. 5.2 is seen to experience some deformation during upstroke in the video, and thus the area is not completely rigid. Second, only a few veins are measured in the experiment to obtain the stiffness, and the results are averaged over several insect samples. Therefore, the exact elastic properties of the particular subject used in the video are not necessarily accurately represented in the model. Despite these differences, the simulated wing deformation pattern still overall exhibits the significant spanwise twisting during upstroke, which resembles what is happening for the real insect.

5.6.3 Analysis of the wing deformation pattern

The rigid wing and the simulated flexible wing are plotted together for a few time instances in Fig. 5.13(a) for both downstroke and upstroke. The comparison allows us to examine the

115
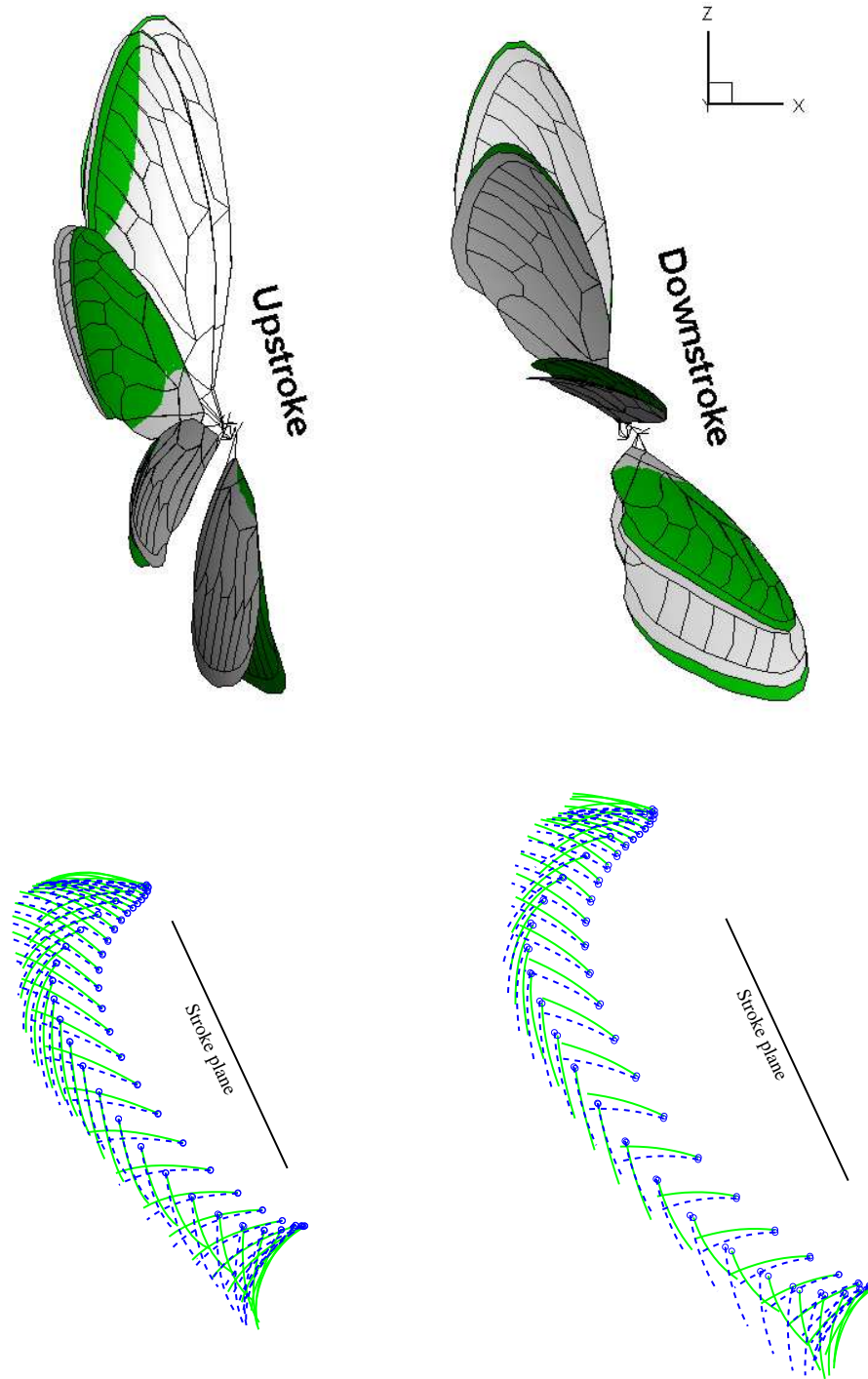
Figure 5.13: Comparison of the simulated flexible wing against the rigid wing. (a) The flexible wing from the FSI simulation (green) along with the rigid wing (grey) at evenly distributed time intervals within one cycle. (b) The 2D wing chord at 1/2 wingspan and 3/4 wingspan from the root, where the blue dashed lines represent the rigid wing.

deformation pattern in 3D. It can be seen that during downstroke, the flexible wing is somewhat twisted with the trailing edge lagging behind the leading edge. During early upstroke, a substantial first-mode type deformation occurs at a large distal portion of the wing. During remaining upstroke, the wing recovers most of its shape and the deformation appears to be small. The 2D view of the wing chord at the 1/2 and 3/4 wingspan are drawn in Fig. 5.13(b) to show the chordwise deformation. From this figure, it can be clearly seen that the deformation causes the change of the angle of attack (AoA), which is defined as the angle between the chord and the stroke plane. The change of the AoA is more pronounced at the 3/4 wingspan than at the 1/2 wingspan, which is a result due to the spanwise twist of the wing.

The simulated displacement of the wing tip measured at point D (see Fig. 5.2(a)) in the 3D space is plotted in Fig. 5.14(a), where a peak value over 0.4 cm occurs during early upstroke. This peak displacement is almost twice of the maximum displacement during the entire downstroke, which is consistent to the asymmetric deformation pattern as observed in the high-speed video. As shown earlier, the passive deformation causes an additional pitching motion to a wing chord. In Fig. 5.14(b), we plot the effective pitch angle of the wing chord at the 1/2 and 3/4 wingspan. Note that the pitch angle is the complementary angle of the AoA. The figure shows that the pitch angle is increased due to the wing deformation. Substracting the active pitch angle of the wing chord from the effective pitch angle, we obtain the passive pitch angle, which is plotted in Fig. 5.14(c). At the 3/4 wingspan, the passive pitch angle reaches a peak value of $25°$ after the suppination due to the large wing deformation at the moment. For the 1/2 wingspan, the peak value is around $15°$. During downstroke, the passive pitch angle is only less than $10°$.

All of these figures have shown significant asymmetry in the wing deformation between downstroke and upstroke. In particular, the greatest deformation takes place shortly after the suppination. Overall, the deformation characteristics can be explained from the wing kinemat-

117

(a)

(b)

(c)
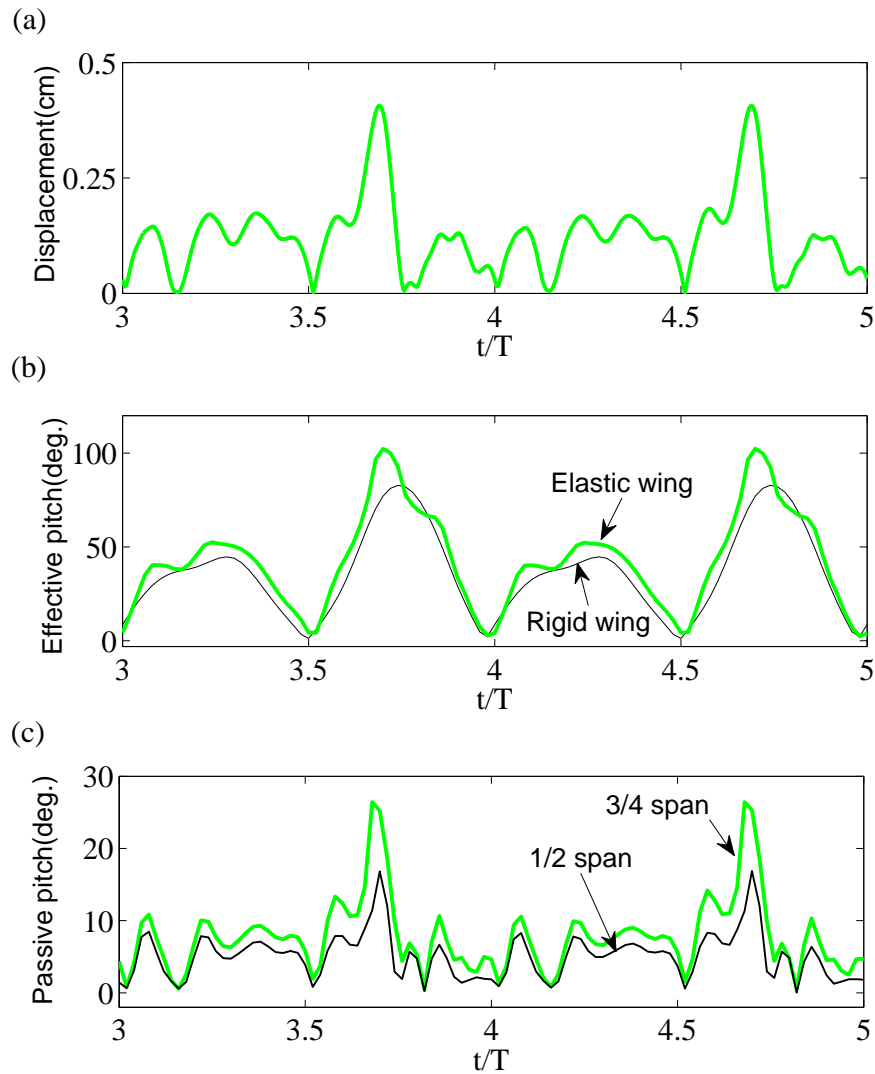
Figure 5.14: Dynamic pitching motion due to the wing deformation. (a) The history of the total displacement at the wing tip (measured at point D marked in Fig. 5.2(a)). The total displacement is calculated with respect to the rigid wing in 3D from the FSI simulation. (b) The history of the effective pitch angle at the 3/4 wingspan for the flexible wing and the rigid wing. (c) The passive pitch angle at the 1/2 and 3/4 wingspan. In all the figures of this chapter, the first half period represents downstroke and the second half represents upstroke, unless otherwise noted.

ics, the wing inertial force, and the aerodynamic force from the flow. Qualitatively speaking, the inertial force becomes greatest during suppination and pronation, when the wing experiences largest acceleration and deceleration, and the aerodynamic force becomes greatest during

118

the mid stroke when the wing has fastest translational velocity. However, the situation is complicated by the details of the wing kinematics. For example, the wing has a greater angle of attack during downstroke than during upstroke. Therefore, the aerodynamic force is greater during downstroke as well. During pronation, the inertial force causes the wing to pitch and perform some level of passive pronation. Then during downstroke, this passive deformation is sustained by the great aerodynamic force during this period. Correspondingly, the passive pitch angle is relatively flat during downstroke, as shown in Fig. 5.14(c).

During suppination, the wing again experiences a great inertial force. What makes the suppination different from the pronation is that during suppination, the wing also moves backward while moving upward. Therefore, the inertial torque on the wing becomes even greater during suppination. Furthermore, the wing is undergoing elastic recovery from the deformation sustained during the downstroke. As a result, the combined inertial force and elastic overshoot causes the wing to have large deformation shortly after the suppination. Finally, the pre-existing camber makes the wing to be structurally asymmetric and also contributes to the asymmetric deformation pattern. This effect will be discussed later.

5.6.4 Lift, thrust, and power of the flexible wing

The averaged lift, thrust, and aerodynamic power for the flexible wing (one single wing) and the rigid wing are listed in Table 5.4. Also listed are the data for the flexible wing with the pre-exisitng camber removed, which will be discussed later. To compare the wing performance, we also compute the total aerodynamic force as the resultant force of the lift and thrust. Since it is tethered in the experiment, the cicada may want to produce largest force to escape. Therefore, the force vector may be directed more in the horizontal direction so that it does not have to counteract the gravity. As seen in the table, the thrust is higher than the lift for both the flexible

	F_T (10 mg)	F_L (10 mg)	F (10 mg)	P (10^{-4} W)	F/P (N/W)	F_T/P (N/W)
Flexible wing	7.2	5.4	9.0	29.1	0.31	0.25
Rigid wing	6.6	6.0	8.9	33.4	0.27	0.20
Uncambered wing	7.9	3.7	8.7	25.0	0.35	0.32

Table 5.4: Thrust (F_T), lift (F_L), lift-trust-combined (F), and power (P) of the cicada forewing from the numerical simulation, which are averaged over a few flapping cycles. The power economy is calculated by dividing the power by either F or F_T. Note that the force data are shown for one single wing only.

wing and the rigid wing. In addition, since the hindwings are removed from the insect, the total force produced by two forewings is only close to the body weight of the insect.

Comparing the flexible and the rigid wings, we find that the flexible wing produces 9.1% higher thrust, but the lift is approximately 10% lower. The total force of the flexible wing is about the same as the rigid wing. Looking at the power consumption, we see that the flexible wing consumes 29.1×10^{-4} W on average, which is 13% lowered than the 33.4×10^{-4} W by the rigid wing. As a result, the power economy, defined by the total force F per unit power, is $F/P = 0.31$ N/W for the flexible wing, which is 15% higher compared to 0.27 N/W by the rigid wing. Consider that the cicada is tethered in the experiment and the horizontal thrust may be mainly the useful force for the insect as discussed earlier, we alternatively use F_T/P as the efficiency measure. According to this criterion, the power economy of the flexible wing is 0.25 N/W and is 25% higher than the rigid wing.

The instantaneous lift, thrust, and power are shown in Fig. 5.15 for the flexible wing and the rigid wing. Note that lift and thrust are defined here in the global coordinate system. That is, the lift is in the opposite direction of the gravity, and the thrust is in the horizontal direction. Since the wing stroke is along the stroke plane, aerodynamic lift and drag can be defined using the convention of airfoil theory. That is, the aerodynamic lift is perpendicular to the stroke plane, while the aerodynamic drag is parallel to the stroke plane and opposite to the wing stroke. For

the cicada tethered in the experiment, the stroke plane angle is about 85°. Therefore, the aerodynamic lift contributes to the physiological lift and thrust; the aerodynamic drag contributes to the physioloigcal lift only during downstroke and to the physiological thrust only during upstroke. During other times, the aerodynamic drag has negative contributions to the physioloigcal lift or thrust. With this understanding in mind, we may make connection between the instantaneous wing posture and the force production.

Fig. 5.15(a) shows that the flexible wing produces somewhat less lift during downstroke than the rigid wing but also generates less negative lift during upstroke. The reduced lift during downstroke has to do with the passive wing twist that leads to less projected wing area in the horizontal plane. Fig. 5.15(b) shows that the flexible wing produces slightly greater thrust than the rigid wing during downstroke and significantly higher thrust during upstroke. The thrust increase during upstroke has to do with the large wing deformation during early upstroke, where the wing is moving upward and backward and it has more projected area in the vertical plane due to the twisting deformation. Fig. 5.15(c) shows that the flexible wing requires significantly lower power during downstroke than the rigid wing and but a similar amount of power during upstroke. For both the flexible and the rigid wings, more power is required during downstroke.

5.6.5   Wing deformation in vacuum

Have quantified the passive deformation of the flexible wing in air, we now examine the wing deformation in vacuum, which is done by simply runing the solid-dynamics solver only. This study will allows us to compare the deformation pattern with that in air and to better undertand the cause of the wing deformation. Fig. 5.16(a,b) shows the wing chord at the 1/2 and 3/4 wingspan locations for both the in-vacuum and the in-flow wing patterns that are obtained from the numerical simulations. The corresponding instantaneous passive pitch angle for both

121
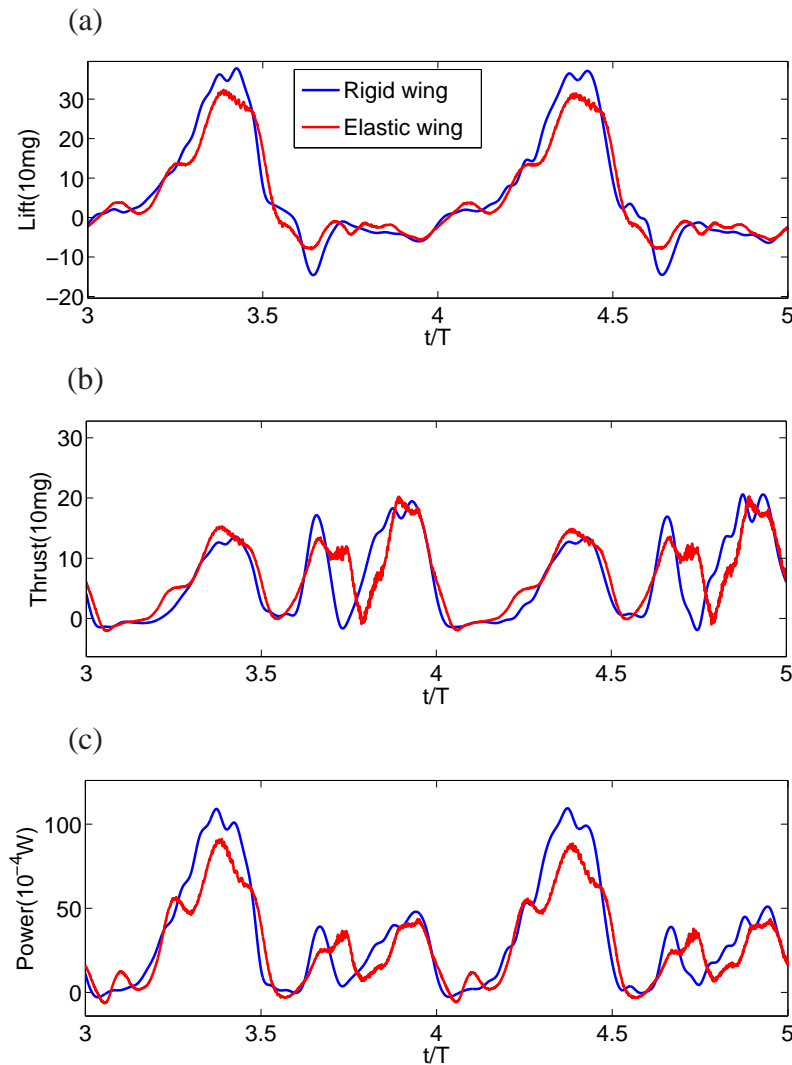
Figure 5.15: Lift, thrust, power comparison between the flexible wing and the rigid wing, where the history of the lift (a), thrust (b) and aerodynamic power (c) are shown for two flapping cycles. Note that the data are shown for one single wing.

wings is shown in Fig. 5.16(c,d) at the same spanwise locations.

First of all, we see that during wing reversals, the wing in flow has the same amount of deformation as the wing in vacuum, but the deformation is somwhat delayed in flow. Second, during downstroke the deformation of the wing in vacuum is much less than that of the wing in flow. This is because the wing in vacuum does not have the aerodynamic force to sustain its deformation. Third, during early upstroke, the wing in flow shows greater deformation than

the wing in vacuum, especially at the 3/4 wingspan where the aerodynamic force is large. At the 1/2 wingspan, the wing in flow has greater deformation in general during early upstroke, but the peak deformation is similar to that of the wing in vacuum. From these observations, we can conclude that the aerodynamic force indeed has significant contributions to the deformation pattern of the wing, especially at the distal area where the mass ratio is low as discussed before.

Finally, Fig. 5.16(c,d) shows that there are more oscillations seen in the histories of the wing chords for the wing in vacuum. These oscillations are caused by the free vibration of the wing in the absence of the surrounding fluid.

Since the first natural mode has a frequency more than seven times higher than the flapping frequency, the oscillations of the wing in vacuum is due to the natural vibration of the wing structure. In the presence of the fluid, these oscillations are largely dampened out by the fluid forces.

5.6.6   Effect of the pre-existing camber

A particular question we would like to address in this work is the effect of the pre-existing camber on the wing deformation and on the aerodynamic performance of the flexible wing. As seen in Fig. 5.1(a) for the cicada, many insect wings have a pre-existing camber that is convex on the dorsal side but concave on the ventral side. It is expected such a curvature would enhance the spanwise stiffness of the wing. Such spanwise stiffness is much needed as the wings bear most of their load in the form of the moment about the longitudinal axis of the body. However, the camber also introduce dorsal-ventral asymmetry to the wing structure, and its effect on the aerodynamics and on the wing deformation is not yet clear.

We first perform a static-load test to examine the effect of camber on the stiffness symmetry of the wing. Using the finite-element model, we apply a constant force on a chosen point on the
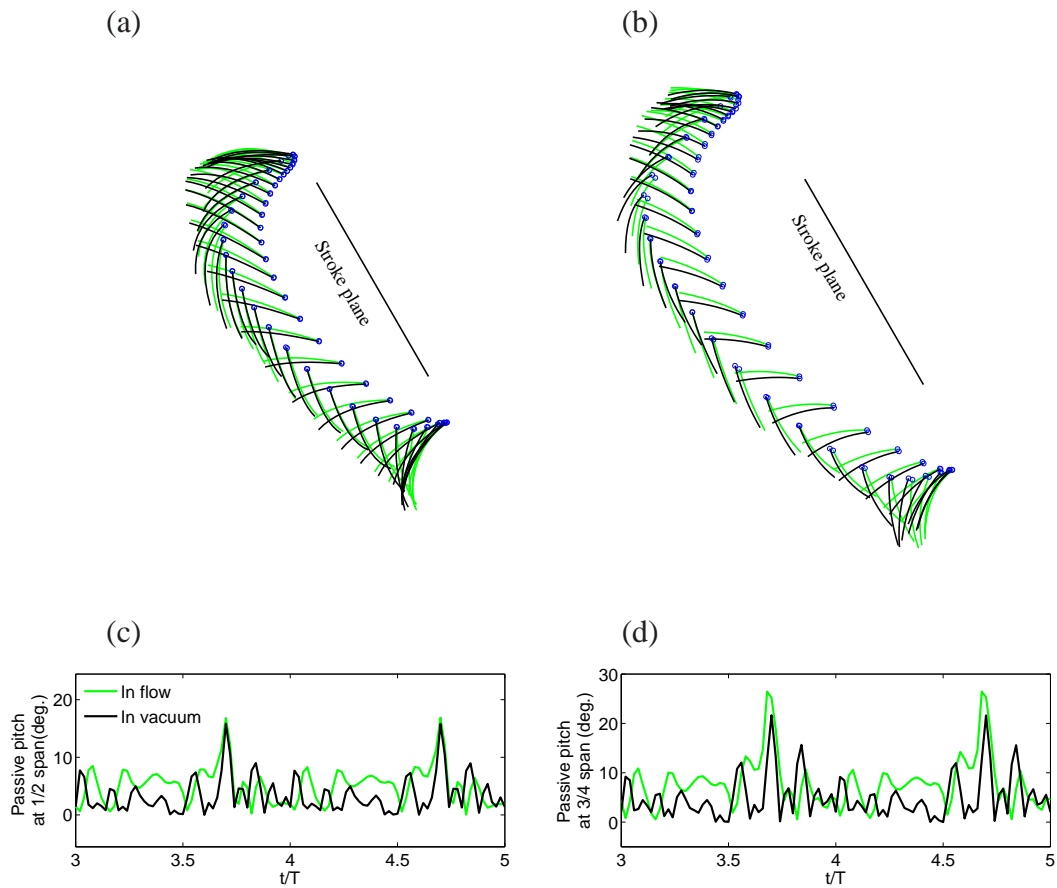
Figure 5.16: Wing deformation in vacuum v.s. in flow. The 2D wing chord is shown at (a) the 1/2 wingspan and (b) the 3/4 wingspan for both in-vacuum (black color) and in-flow (green) deformations. The instantaneous passive pitch angle is plotted in (c) for the 1/2 wingspan and in (d) for the 3/4 wingspan.

wing surface from either ventral or dorsal side. The force is 60 mg, about one-third of the total mass of the insect. Two positions are chosen as the loading point, as indicated in Fig. 5.17 by F1 and F2. The displacement of point C, a point on the trailing edge obtained from the simulation is used for measurement. Both the cambered wing and the flat (uncambered) wing are tested. Results are given in Table 5.5. It is found that for the cambered wing, the deformation caused by a ventral force is significantly lower than that by a dorsal force. For the uncambered wing, symmetric deformation is seen from the table, as expected. Furthermore, the uncambered wing has greater deformation than the cambered wing when the load is on the ventral side. When the
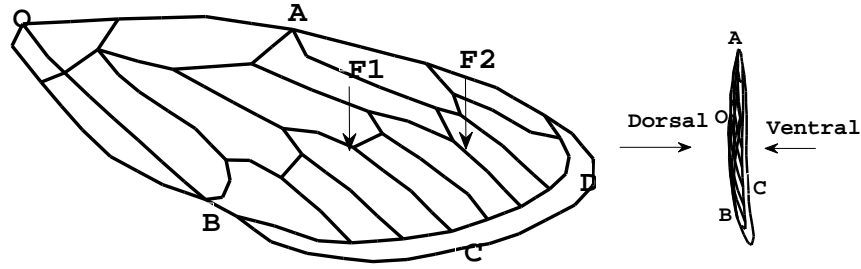
Figure 5.17: The static-load test for the effect of the pre-existing camber, where the load is applied normal to the wing surface.

	Cambered wing		Uncambered wing	
Load applied	ventral load	dorsal load	ventral load	dorsal load
F1 = 60 mg	0.28	-0.35	0.36	-0.36
F2 = 60 mg	0.29	-0.47	0.51	-0.51

Table 5.5: The static-load test for the effect of the pre-existing camber, where the displacement is measured at point C in the static-load tests. The unit of the displacement is cm.

load is on the dorsal side, the uncambered wing has only slightly larger deformation than the cambered wing. Therefore, the pre-existing camber strengthens the flexural stiffness of the wing mainly for the ventral load. The camber thus introduces an asymmetric stiffness to the wing, which is important for the dynamic deformation of the wing.

Next, we run the FSI simulation for the uncambered wing and compare the wing deformation with that from the cambered wing simulation. The deformation pattern is analyzed in Fig. 5.18 where the tip displacement, the instantaneous wing chord, and the passive pitch angle at the 1/2 and 3/4 wingspans are shown. Together shown are the result from the cambered wing. Consistent with the static-load test, the uncambered wing shows much greater deformation during downstroke than the cambered wing, while during upstroke, the uncambered wing has similar amount of deformation with the cambered wing. During the early upstroke, both

wings have a similar peak value in the passive pitch angle. More quantitatively, the tip displacement during downstroke is nearly doubled for the uncambered wing compared to that of the cambered wing.

From these results, we see that the pre-existing camber has contributed to the stiffness asymmetry of the wing structure. Partially becauase of this stiffness asymmetry, the wing deformation becomes asymmetric between upstroke and downstroke. A similar effect was discussed previously for other insects like butterflies (Wootton, 1993). However, it is important to point out that in the present study, even if this camber is absent, we still observe a significant asymmetry in the wing deformation. This feature can be seen from Fig. 5.18(d,e) where the uncambered wing still shows a greater peak deformation during early upstroke. As discussed earlier, this peak deformation is caused due to the combined the aerodynamic force and wing inertia. Therefore, this particular asymmetric pattern can be caused not only by the structural design of the wing, but also by the inertial and aerodynamic loads on the wing.

The wing model after removing the pre-exisiting camber also has different aerodynamic performance. Fig. 5.19(a-c) shows the instantaneous lift, thrust, and power for both the cambered and uncambered wings. As discussed earlier, the camber is important to maintain the rigidity and reduce wing deformation during downstroke. Furthermore, a camber is beneficial for the production of the aerodynamic lift as in the case of the traditional airfoil. Therefore, in Fig. 5.19(a), we see that the lift force is significantly reduced during downstroke after the camber is removed.

Shown in Fig. 5.19(b), the thrust of the uncambered wing is also reduced during downstroke. However it is increased during upstroke, especially during the early stage. Overall, Table 5.4 shows that the average lift of the uncambered wing is reduced by 30% and the average thrust is increased by 10%. The power cost is also lower for the uncambered wing, which is reduced
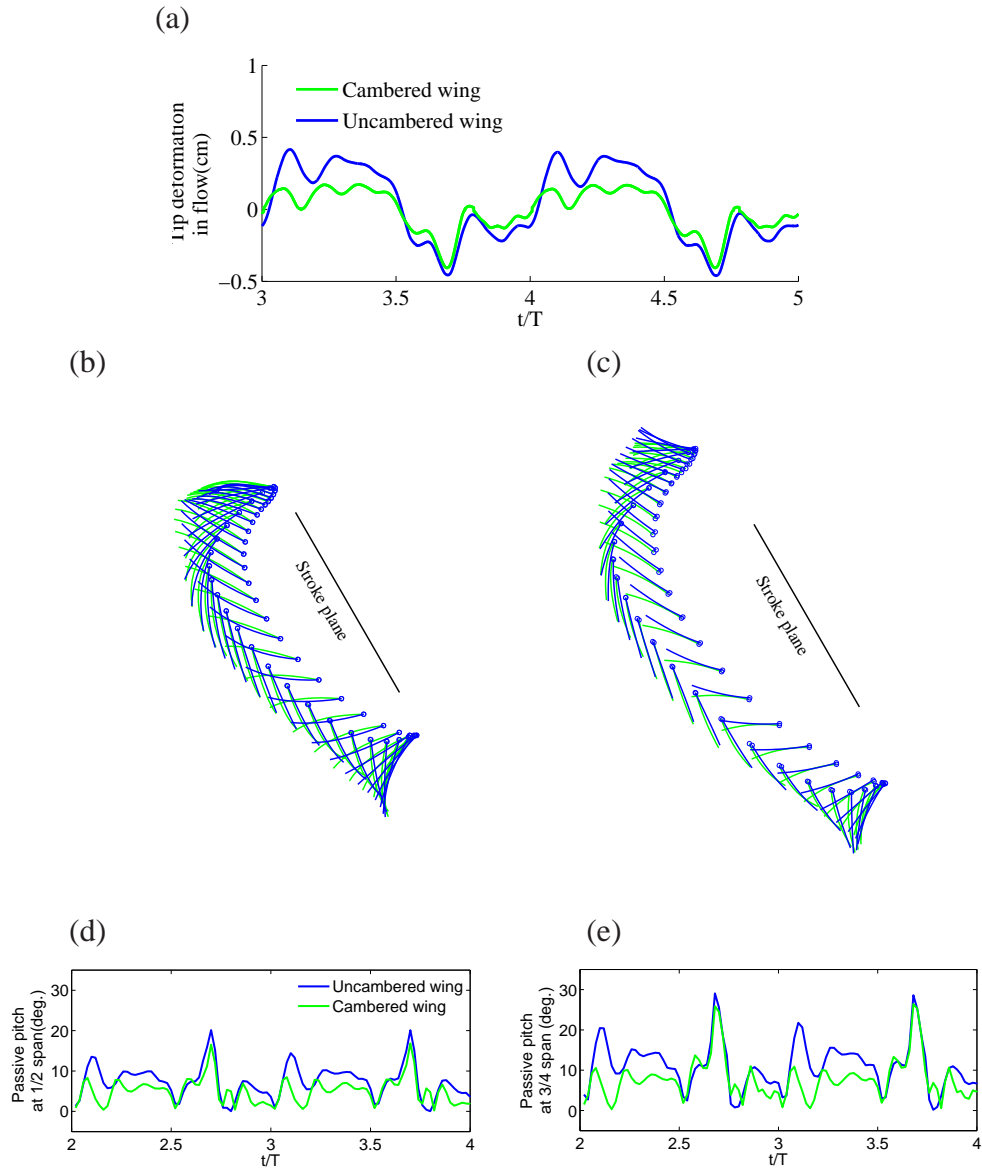
Figure 5.18: Effect of the pre-exising camber on the wing deformation in air. (a) The tip displacement in 3D; (b,c) the instantaneous wing chord at the 1/2 wingspan (b) and the 3/4 wingspan (c); (d,e) the passive pitch angle at the 1/2 wingspan (d) and the 3/4 wingspan (e).

from 29.1×10^{-4} W to 25.0×10^{-4} W, and the overall power economy reaches 0.35 N/W in terms of F/P and 0.32 N/W in terms of F_T/P. Both of these two measures are slightly higher than the corresponding data of the cambered wing. Therefore, in the present case, the camber does not seem to introduce significant benefit in the efficiency of the wing. However, since the contours of the camber is somewhat arbitrary in this study, the exact camber effect on the aerodynamics
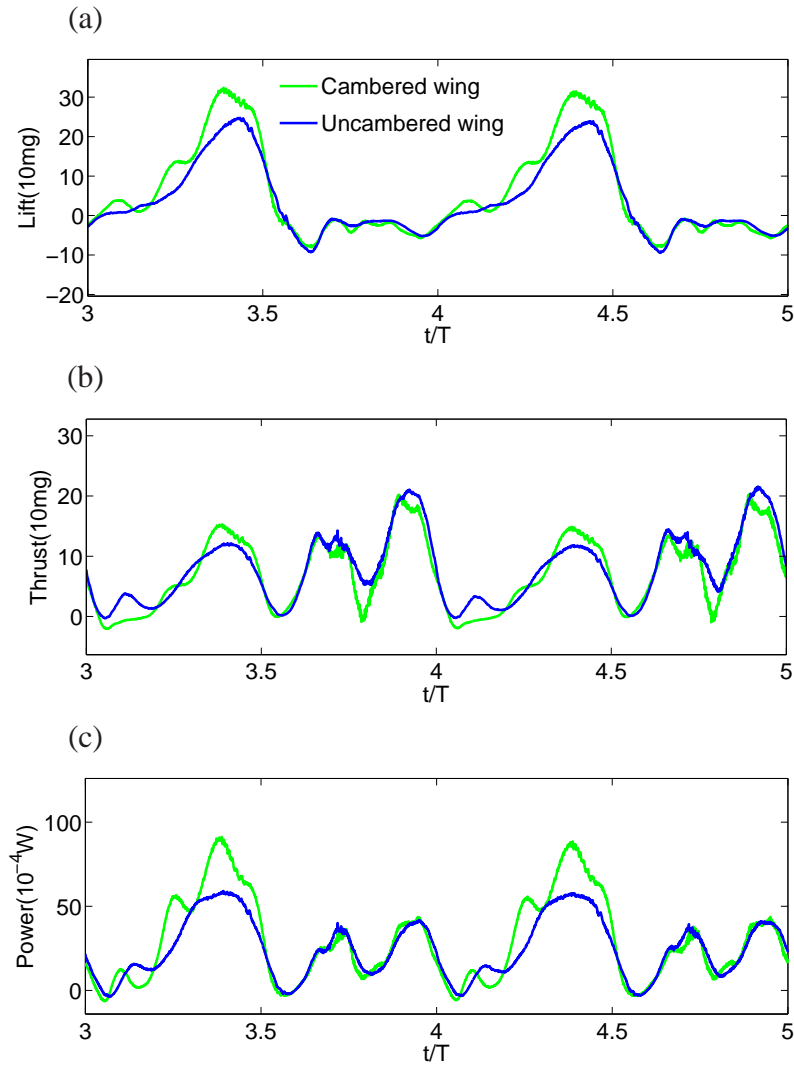
Figure 5.19: Instantaneous lift (a), thrust (b), and power (c) of the uncambered wing along the data for the cambered wing.

will be studied in future with more realistic camber specification.

5.6.7 Unsteady flow field

The flow field is visualized by plotting the vortex structures in the flow. The isosurface is defined as the maximal imaginary part of complex eigenvalues of the velocity gradient tensor, Λ_{max}. Fig. 5.20 shows the vortex fields at time $t/T = 2$, 2.25, 2.5, 2.75, which correspond to pronation, mid-downstroke, suppination and mid-upstroke, respectively. Under the tethering

condition, there is no incoming flow to convect the vortices generated by the wing to the far field. Therefore, the flight in this case may be viewed as hovering flight where the fore-aft axis is treated as the vertical axis in hovering flight and the gravity is acting in the negative x-direction. In the absence of freestream, the vortices in the flow are more likely to interact with each other. From these figures, we can identify various vortex structures that are distinct features of flapping wings in general, such as the leading-edge vortex, the trailing-edge vortex, and the tip vortex.

5.7   Conclusion

In this study, we have described an integrated approach to model the aerodynamics and aeroelasticity of the flexible wings of insects. The forewing of the periodical magicicada is used as the subject. The study integrates high-speed imaging for the wing kinematics, experimental measurement of the elastic properties of the wing, three-dimensional simulation of the fluid–structure interaction of the wing with the surrounding fuid, and validation of the computational model against the experimental data. To the best of our knowledge, this is the first time for such a methodology to be used in modeling flexible wings of insects. Thus, it represents a significant advancement in the study of insect flight.

In the model, the complex structure of the cicada wing is reconstructed from images of the wing and the material properties are parametrized by only a few variables for the vein groups. Yet the essential features of the dynamic deformation pattern has been captured in the numerical simulation. Therefore, the modeling approach may provide useful guideline for the future study of the insect wings.

Our scaling and simulation results show that the wing deformation of the cicada forewing is caused by both the wing inertia and the aerodynamic force produced by the wing itself. Fur-
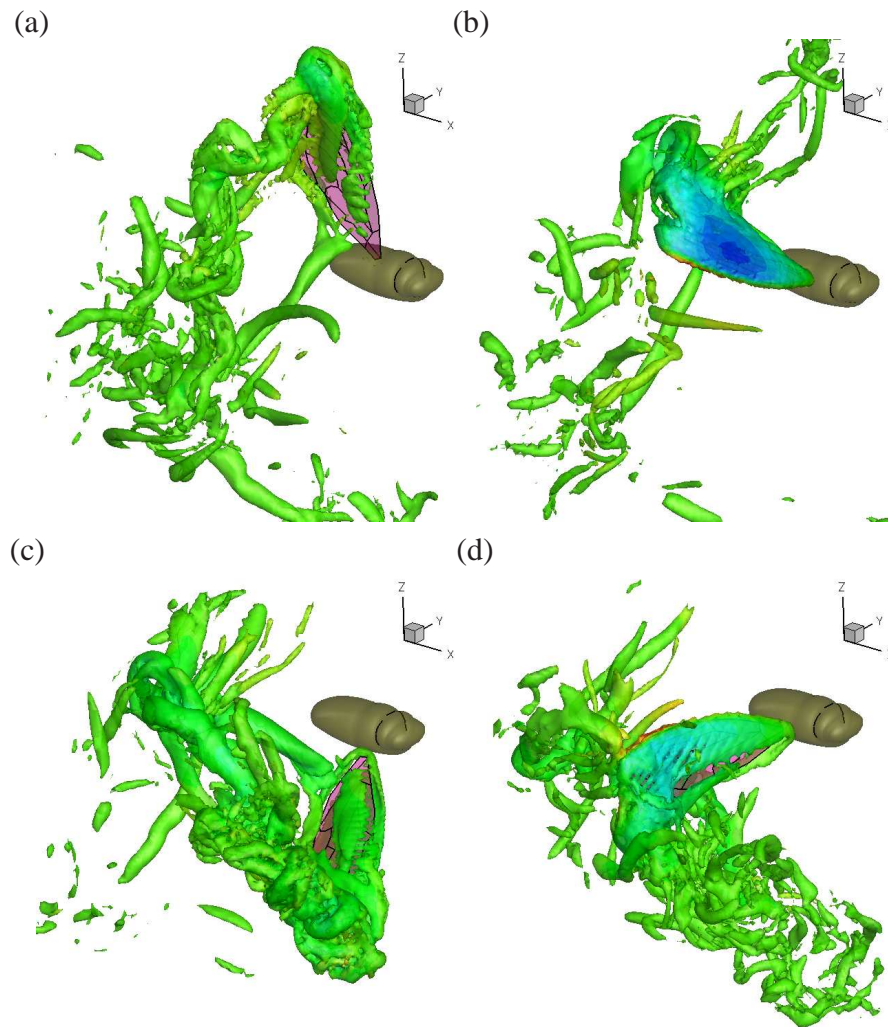
Figure 5.20: Instantaneous flow field of the flexible wing, where the vortex structures are shown for (a) pronation, (b) middle downstroke, (c) suppination, and (d) middle upstroke. The isosurface of the vortex structures is shown and it is colored with the pressure level. Note that the insect body is added to indicate the relative wing position but it is not actually included in the simulation.

thermore, the deformation is significantly asymmetric as seen for many other insects. That is, the deformation is greater during upstroke than during downstroke. According to our analysis, such an pattern has to do with both the wing design, i.e., the pre-existing camber on the wing surface, and asymmetric wing kinematics, and also the fluid–structure interaction. For the last factor, the aerodynamic force modulates the phase of the elastic deformation and recovery, and along with the wing inertia, they lead to a peak displacement of the wing during early upstroke.

Our simulation suggests that the effect of the wing flexibility is beneficial for the aerodynamic performance in terms of power efficiency. This result is consistent to the studies we presented in previous chapters using idealized flapping-wing models. By running the simulation with the pre-existing camber removed, we found that the wing stiffness is reduced during downstroke but is not affected significantly during upstroke. Therefore, the camber contributes to the asymmetrical stiffness of the wing. However, even if the camber is removed, the asymmetric deformation as discussed earlier still persists, which confirms the contributions from the aerodynamic and wing inertial factors.

Finally, although the insect is tethered in the present study and therefore the wing motion may be different from that in the real flight, the results described here nevertheless shed some light into the role of the wing flexibility in the aerodynamics of the insect and also the mechanism of the wing deformation.

CHAPTER VI

SUMMARY, CONTRIBUTIONS, AND FUTURE WORK

6.1   Summary of this thesis

In this thesis, we focus on the computational modeling of the fluid–structure interaction involved in flexible insect wings and fish fins. Given that an efficient method for this type of problem is still lacking, we first developed a general-purpose 3D numerical approach that is suitable for flows interacting with thin-walled structures. Based on a fixed Cartesian grid and an improved immersed-boundary solver, the method can treat large displacements of the boundary without the need for mesh regeneration. The finite-element method used to solve the solid-body dynamics employs the classical formulations of thin-walled structures such as frames, membranes, and plates and is thus suitable for modeling the vein or ray network of the biological propulsors. The fluid–structure coupling is achieved by iterating the two solvers alternatingly until convergence is reached. Therefore, each full time step is implicit, and strong coupling is achieved. Although more computationally expensive than an explicit approach, the current strong-coupling approach greatly improves the numerical stability and leads to much more robust simulations. We have provided several case studies to validate the current numerical method.

Three model configurations have been developed to study various aspects of the fluid–structure interaction of the flapping wings/fins. In the first model, a rectangular low-aspect-ratio elastic panel pitching in a freestream to model propulsion of an elastic fish fin. By varying the magnitude of the pitching angle and the fin rigidity, we found that when the fin has the

first-mode deformation pattern, the thrust coefficient is primarily a function of Strouhal number, which is defined on using the swimming speed, pitching frequency, and the tail excursion of the deformable fin. In another word, compared to the rigid panel with the same pitching angle and frequency, the flexible panel has an increased excursion amplitude due to deformation and thus produces more thrust. In terms of power consumption, the efficiency of the fin is significantly enhanced due to the elasticity of the fin. Compared to the rigid panel flapping at an equivalent amplitude, the flexible panel produces the same amount of thrust but requires less power input. Therefore, the result suggests that the passive deformation of fins is beneficial to the hydrodynamic performance of fish.

In the second configuration, we investigate different roles of the wing inertia and the aerodynamic pressure in the deformation of insect wings and in the wing performance. The relative importance of the inertia with respect to the pressure is characterized by a dimensionless parameter, the mass ratio, and the flexibility is characterized by the ratio between the flapping frequency and the natural frequency of the wing, i.e., the ratio between the inertial force and the elastic force in the wing. Using a rectangular plate in hovering condition and varying its mass ratio and flexibility, we found that the chordwise deformation of the wing causes a dynamic pitching, and the aerodynamic performance of the wing is affected not only by the increased pitching amplitude due to the deformation but also by the phase and rate of the passive pitching. At high mass ratios, the wing exhibits an advanced pitching; while at low mass ratios, the wing exhibits a delayed pitching. Regardless the mass ratio, wing deformations of proper magnitude enhance the lift production and improve the power efficiency. Furthermore, at low mass ratios, the aerodynamic force sustains the chordwise deformation initiated by the inertial force at the wing reversals, and the power efficiency can be further improved. The results suggests that the low mass ratio of many insect wings in the distal area has significant aerodynamic advantages.

In the third configuration we, for the first time, have developed a high-fidelity computational model of the real insect wing and have studied the aerodynamics and aeroelasticity simultaneously for a real insect. The overall methodology integrates high-speed imaging of the insect wing kinematics, experimental measurements of the mechanical properties of the wing, computational modeling of the 3D flow and wing deformation, and validation of the simulation results against the experimental data. In this study, the cicada forewing is used as the subject. A sophisticated finite-element model is built to resolve the wing's vein network, so that the inhomogeneous and anisotropic properties of the entire wing are incorporated by these frame elements. The mass distribution and bending stiffness of the veins are measured, and the data are inserted into the structural model. The wing actuation kinematics is reconstructed from one camera view. Finally, the FSI model is validated by comparing the simulated wing displacement with that obtained from the high-speed imaging measurement. The result shows that the complex wing structure of the insect can be parametrized efficiently using a few variables. Comparing to the rigid wing, the flexible wing has led to significant power efficiency. Furthermore, the wing deformation depends on both the wing inertia and the aerodynamic force. The inertial and aerodynamic forces work in different phases of a wing stroke, and together they cause a deformation pattern that assists with the wing reversal and improves the force production during the wing stroke. The simulated deformation pattern is asymmetric. That is, the wing has greater deformation during upstroke than during downstroke. This pattern is consistent with the experimental observation of the cicada wing, and it is also common in many other insects. This asymmetry has to do with both the pre-existing camber and the wing actuation kinematics. Therefore, the result suggests that the asymmetric wing deformation in insects is dependent not only on the asymmetric design in the wing structure, i.e., the camber or the "one-way hinges", but also on the asymmetric wing kinematics and consequently the asymmetric aerodynamic/inertial forces

134

on the wing.

6.2   Contributions of this thesis

Given that the three-dimensional fluid–structure interaction in insect flight and fish swimming has been rarely studied previously, and there is still a lack of the proper numerical method for this type of problem, this thesis has made the following significant contributions:

- We have developed a three-dimensional numerical method for simulating the fluid–structure interaction between a viscous incompressible flow and thin-walled structures with large-displacement and large-rotation deformations, since there is a lack of proper methods of such in literature. Based on the immersed-boundary method for the flow and the finite-element method for the structure, the method can handle moving boundaries without the need for mesh regeneration, and it is particularly suitable for modeling biological structures such as insect wings and fish fins that consist of membranes and vein/ray networks. We envision this method will be useful for in-depth understanding of the fluid dynamics involved in the flying and swimming in nature and also for the future development of biomimetic aerial/underwater vehicles.

- We have utilized the computational approach to study a low-aspect-ratio flexible pitching foil in free stream, an idealized model for the caudal fin of fish, and have obtained a scaling law for its thrust production. In addition, its power efficiency and the three-dimensional wake are characterized.

- We have utilized a 3D hovering wing model to study the effect of wing flexibility on the aerodynamic performance of flapping wings. The new finding suggests that the effect of the wing deformation should not only be viewed from a quasi-static point of view,

135

e.g., change of the angle of attack or creation of a camber by the deformation; instead, the phase and rate of pitching due to the dynamic deformation change the instantaneous lift, drag, and power and thus have significant effect on the performance of the wing. Furthermore, the study has clarified the cause of the wing deformation in terms of the inertia-induced or inertia-and-pressure-induced deformation and has found the aerodynamic consequences associated with each of the deformation situations.

- For the first time, we have utilized an integrated approach to model the aerodynamics and aeroelasticity of real insect wings with high fidelity. The results have significant implication on the accurate and efficient parametrization of insect wings. Furthermore, the results confirms the role of the wing flexibility found using the idealized models in improving the aerodynamic performance of the wing, and they have led to new findings in the exact cause of the particular wing deformation pattern as observed in real insects.

The work described in this thesis has been presented in the form of the following peer-reviewed journal publications or conference abstracts:

1. Tian, F.-B., **Dai, H.**, Luo, H., Doyle, J.F., Rousseau, B. (2013) Fluid-structure interaction involving large deformations: 3D simulations and applications to biological systems. Submitted to Journal of Computational Physics.

2. **Dai, H.**, Luo, H., Ferreira de Sousa, P., Doyle, J. F. (2012) Thrust performance of a flexible low-aspect-ratio pitching plate. Physics of Fluids. 24, 101903.

3. **Dai, H.**, Luo, H., Doyle, J. F. (2012) Dynamic pitching of an elastic rectangular wing in hovering motion. Journal of Fluid Mechanics. 693, 473-499.

4. Luo, H., **Dai, H.**, Ferreira de Sousa, P., Yin, B. (2012) On numerical oscillation of the direct-forcing immersed-boundary method for moving boundaries. Computers & Fluids.

56, 61-76

5. **Dai, H.**, Luo, H., Song, J., Doyle, J.F., (2013) Effect of the pre-existing camber on fluid–structure interaction of cicada wings. AIAA Paper 2013-952.

6. Luo, H., **Dai, H.**, Mohd Adam Das, Shahrizan Syawal, Song J., Doyle, J. F. (2012) Toward high-fidelity modeling of the fluid-structure interaction for insect wings. AIAA Paper 2012-1212.

7. Luo, H., **Dai, H.**, & Doyle, J. (2010) Three-dimensional flow-structure interaction in dragonfly wings. AIAA Paper 2010-556.

8. Luo, H., **Dai, H.**, Doyle, D.F. Three-dimensional simulations of fluid and elasticity for flapping wings and fins. *Fluids & Elasticity 2012*, November 14-16, 2012, La Jolla, CA.

9. Luo, H., **Dai, H.**, Mohd Adam Das, Shahrizan Syawal, Song J., Doyle, J. F. (2012) Toward high-fidelity modeling of the fluid-structure interaction for insect wings. *The 50th AIAA Aerospace Sciences Meeting*. Jan. 9-12, 2012. Nashville, TN.

10. **Dai, H.**, Mohd Adam Das, Shahrizan Syawal, Luo, H. Observation of the wing deformation and CFD study of cicadas. *The 64th Annual Meeting of APS/DFD*, November 20-22, 2011. Baltimore, Maryland.

11. Ferreira de Sousa, P., **Dai, H.**, Luo, H., Doyle, J. Thrust performance and wake structure of a pitching flexible plate at low aspect ratios. *The 63rd APS/DFD Annual Meeting*, Nov. 21-23, 2010. Long Beach, California.

12. Luo, H., **Dai, H.**, Doyle, J. Three-dimensional flow-structure interaction in dragonfly wings. *The 48th AIAA ASM Meeting*, Jan 4-7, 2010. Orlando, FL.

137

13. Luo, H., **Dai, H.**, Ferreira de Sousa, P. A hybrid formulation to suppress the numerical oscillations caused by immersed moving boundaries. *The 62nd APS/DFD Annual Meeting*, Nov. 22-24, 2009. Minneapolis, MN.

14. **Dai, H.**, Luo, H., Deng, X. Flapping counter force - a unique flight stabilizing mechanism enabled by flapping wings. *The 62nd APS/DFD Annual Meeting*, Nov. 22-24, 2009. Minneapolis, MN.

15. Luo, H., **Dai, H.** Unsteady flow motions in the supraglottal region during phonation. *The 61st APS/DFD Annual Meeting*, Nov. 23-25, 2008. San Antonio, TX.

6.3   Directions of the future work

Based on the work described in this thesis, we make the following suggestions for the directions of the future research:

- *More advanced CFD methods:* In terms of the numerical method, higher-order approaches capable of handling large-displacement moving boundaries can be developed for modeling flapping wings. As other common CFD methods, the current numerical method is second-order accurate. However, the relatively low Reynolds number flows of the flapping wings/fins can be still be turbulent, e.g., large-size birds and fish, which may lead to prohibitive computational cost for direct numerical simulations. Without resorting to the less accurate turbulent modeling approaches, one way is to develop a higher-order (e.g., 6th- or 10th-order) approach to simulate the turbulent flow with moderate resolution. Such a method could be very useful for modeling bird/fish and small-size biomimetic unmanned aerial/underwater vehicles.

- *Further in-depth understanding of the aerodynamics and aeroelasticy:* The complex flow

138

behavior of the flapping wings and fins require more in-depth studies, especially in three dimensions and when fluid–structure interaction is involved. For example, what is the role of the spanwise flow in a 3D situation? Is there a quantitive relationship between the vortical structures in the wake and the force production of the propulsor for general situations? Does the role of the wing flexibility still remain the same for various species of insects when their wing structures, morphology, and kinematics are drastically different? And if so, how can the different deformation patterns provide the same function? We expect computational modeling can be used as a powerful tool to answer these questions.

- *Fluid dynamics in unsteady maneuvers:* So far there has been very limited study on the fluid dynamics involved in the unsteady flight modes, e.g., take-off, perching, fast yaw/roll/pitch turning. Unlike conventional aircrafts, in these flight modes the aerodynamics of the flapping wings is closely coupled with the flight dynamics. Full 3D simulations would be needed along with the experiments to understand the flow and force/torque production during execution of unsteady maneuvers. In addition, the nonlinear stability problems involved in these flight modes need to be thoroughly investigated to better understand the flight control of these animals.

- *Engineering development of the biomimetic robots:* Current designs of the flying/swimming robots that emulate the animals are still largely based on intuitive and qualitative understanding of the fluid dynamics. It requires further study to see how the understanding of the biological propulsors can be translated into the engineering designs that do not necessarily fully replicate the actuation mechanism or the wing/fin structure in nature. Another important topic is about the development of low-order flow models (e.g., 1D or lumped-parameter models) that require only minimal calculations but still have a satisfactory level of fidelity. Such models will be extremely useful for the design optimization

and the implementation of the feedback control algorithm. Currently, such models do not yet exist for flapping wings/fins in general. We envision that the high-order models that we are developing will be useful in identifying/creating/calibrating those low-order models in the future.

REFERENCES

A   , D.L., D   , R. & E   , C.P. 2004 Aerodynamic forces of revolving hummingbird wings and wing models. *Journal of zoology* **264** (04), 327–332.

A   , JM, S   , K., B   , DS & T   , MS 1998 Oscillating foils of high propulsive efficiency. *Journal of Fluid Mechanics* **360** (-1), 41–72.

B   , P., H , M.Y. & B   , S. 2001 Direct numerical simulation of flow and heat transfer from a sphere in a uniform cross-flow. *J. Fluids Eng.* **123**, 347.

B , P., C   , E. & Z   , H. 2009 Aerodynamic characteristics, power requirements and camber effects of the pitching-down flapping hovering. *Journal of Bionic Engineering* **6** (2), 120–134.

B   , J.L., B   , K.J.
"U.R. & H , L.W. 1980 A study of three-node triangular plate bending elements. *International Journal for Numerical Methods in Engineering* **15** (12), 1771–1812.

B   , D.W., M. B   , W. H   & M   , R. 1997 Biological surfaces and their technological application - laboratory and flight experiments on drag reduction and separation control. *AIAA Paper* **97**, 1960.

B   , P.G. & F   , C.A. 1985 A triangular membrane element with rotational degrees of freedom. *Comput. Meth. Appl. Mech. Eng.* **50**, 25–69.

B   , P.A. & F   , O.M. 2008 A local directional ghost cell approach for incompressible viscous flow problems with irregular boundaries. *J. Comput. Phys.* **227** (9), 4354–4397.

B   , D.G. & K   , M.M. 2009 MTV measurements of the vortical field in the wake of an airfoil oscillating at high reduced frequency. *Journal of Fluid Mechanics* **620**, 63–88.

B   , I   & S   , F   2008 Numerical investigation of the hydrodynamics of carangiform swimming in the transitional and inertial flow regimes. *J. Exp. Biol.* **211**, 1541.

B   , J.H.J. & S   , A.J. 2006 On the evolution of the wake structure produced by a low-aspect-ratio pitching panel. *Journal of fluid mechanics* **546** (-1), 433–443.

B   , J.H.J. & S   , A.J. 2008 The wake structure and thrust performance of a rigid low-aspect-ratio pitching panel. *Journal of fluid mechanics* **603** (-1), 331–365.

C   , J. S., C   , J. Y. & C   , Y. F. 2008 On the natural frequencies and mode shapes of dragonfly wings. *J. Sound Vibration* **313**, 643–654.

C   , A. J. 1968 Numerical solution of the navier–stokes equations. *Mathematics of Computation* **22** (104), 745.

C , R., G , J.R. & W , M.E. 1978 *Bubbles Drops and Particles*. Academic Press, New York.

C , S. A. & D , T. L. 2003*a* Flexural stiffness in insect wings i. scaling and influence of wing venation. *J. Exp. Biol.* **206**, 2979–2987.

C , S. A. & D , T. L. 2003*b* Into thin air: contributions of aerodynamic and inertial-elastic forces to wing bending in the hawkmoth manduca sexta. *J. Exp. Biol.* **206**, 2999–3006.

D ., H., L , H. & D , J. F. 2012 Dynamic pitching of an elastic rectangular wing in hovering motion. *J. Fluid Mech.* **693**, 473–499.

D , P.A., C , A. & S , A.J. 2012 On the relationship between efficiency and wake structure of a batoid-inspired oscillating fin. *Journal of Fluid Mechanics* **691**, 245–266.

D , M. H., L , F.-O. & S , S. P. 1999 Wing rotation and the aerodynamic basis of insect flight. *Science* **284**, 1954.

D , H., M , R. & N , FM 2006 Wake topology and hydrodynamic performance of low-aspect-ratio flapping foils. *Journal of Fluid Mechanics* **566** (-1), 309–343.

D , J.F. 1991 *Static and dynamic analysis of structures*. The Netherlands: Kluwer.

D , J.F. 2001 *Nonlinear analysis of thin-walled structures: statics, dynamic, and stability*. New York: Springer-Verlag.

D , J.F. 2008 *QED: static, dynamic, stability, and nonlinear analysis of solids and structures*. Software manual, version 4.60.

E , R. H. & C , H. K. 1982 The separation vortex in the weis-fogh circulation-generation mechanism. *J. Fluid Mech.* **120**, 463–473.

E , J.D. 2007 Numerical simulation of the fluid dynamics of 2d rigid body motion with the vortex particle method. *J. Comput. Phys.* **221** (2), 626–648.

E , J. D., T , J. & M , A. 2010 On the roles of chord-wise flexibility in a flapping wing with hovering kinematics. *J. Fluid Mech.* **659**, 94–115.

E , C. P., B , C. V., W , A. P. & T , A. L. R. 1996 Leading-dege vortices in insect flight. *Nature* **384**, 626.

E , A. R. 1988*a* The importance of torsion in the design of insect wings. *J. Exp. Biol.* **140**, 137–160.

E , A. R. 1988*b* The inertial cause of wing rotation in diptera. *J. Exp. Biol.* **140**, 161–169.

142

E , B   P. & T   , A   H. 2007 Impulse generated during unsteady maneuvering of swimming fish. *Exp. Fluids* **43**, 691–700.

F   , E.A., V   , R., O   , P. & M   -Y   , J. 2000 Combined immersed-boundary finite-difference methods for three-dimensional complex flow simulations. *J. Comput. Phys.* **161** (1), 35–60.

F   , R.P., A   , T., M   , B. & O   , S. 1999 A non-oscillatory eulerian approach to interfaces in multimaterial flows (the ghost fluid method). *J. Comput. Phys.* **152** (2), 457–492.

G   , D., H   , R. & S   , L. 1993 Modeling a no-slip flow boundary with an external force field. *J. Comput. Phys.* **105** (2), 354–366.

H   , S. & G   , I. 2007*a* Flexible flapping airfoil propulsion at low Reynolds numbers. *AIAA J.* **45**, 1066–1079.

H   , S. & G   , I. 2007*b* Flexible flapping airfoil propulsion at low Reynolds numbers. *AIAA J.* **45** (5), 1066–1079.

H   , S., M   , D. & G   , I. 2004 Flexible flapping airfoil propulsion at zero freestream velocity. *AIAA J.* **42** (11).

H   , S., W   , Z. & G   , I. 2008 Effect of spanwise flexibility on flapping wing propulsion. *J. Fluid Struct.* **24** (2), 183–199.

H   , T   L. 2008 Software techniques for two- and three-dimensional kinematic measurements of biological and biomimetic systems. *Bioinsp. Biomim.* **3** (034001).

H   , T. L., C   , B. & D   , X. 2009 Wingbeat time and the scaling of passive rotational damping in flapping flight. *Science* **324** (5924), 252–255.

H   , R.D. 1995 Details of the drag curve near the onset of vortex shedding. *Phys. Fluids* **7**, 2102.

J   , T.A. & P   , V.C. 1999 Flow past a sphere up to a Reynolds number of 300. *J. Fluid Mech.* **378**, 19–70.

K   , K., A   , P., P   , S. & C   , J.P. 2000 Fictitious domain approach for numerical modelling of navier–stokes equations. *Int. J. Numer. Meth. Fluids* **34** (8), 651–684.

K   , J., K   , D. & C   , H. 2001 An immersed-boundary finite-volume method for simulations of flow in complex geometries. *J. Comput. Phys.* **171** (1), 132–150.

K   , C   , L   , Z   , G   , Z   , W   , H   & D   , H   2012 3d reconstruction and analysis of wing deformation in free-flying dragonflies. *J. Exp. Biol.* **215**, 3018–3027.

K   , M. 1989 Vortical patterns in the wake of an oscillating airfoil. *AIAA journal* **27** (9), 1200–1205.

K   , J. & C   , H. 2010 Sectional lift coefficient of a flapping wing in hovering motion. *Phys. Fluids* **22**, 071703.

L   , G.V. 2000 Function of the caudal fin during locomotion in fishes: kinematics, flow visualization, and evolutionary patterns. *American Zoologist* **40** (1), 101.

L   , G   V. & M   , P   G. A. 2007 Fish locomotion: kinematics and hydrodynamics of flexible foil-like fins. *Exp. Fluids* **43**, 641–653.

L   , L. & L   , R.J. 2003 An immersed interface method for incompressible Navier-Stokes equations. *SIAM J. Sci. Comput.* **25** (3), 832–856.

L V   , R.J. & L , Z. 1994 The immersed interface method for elliptic equations with discontinuous coefficients and singular sources. *SIAM J. Numer. Anal.* **31** (4), 1019–1044.

L   , C.C., C   , Y.W., L   , C.A. & M D   , JM 2010 Simulating flows with moving rigid boundary using immersed-boundary method. *Computers & Fluids* **39** (1), 152–167.

L   , M. J. 1960 Note on the swimming of slender fish. *J. Fluid Mech.* **9**, 305–317.

L   , M. J. 1973 On the weis-fogh mechanism of lift generation. *J. Fluid Mech.* **60**, 1–17.

M   , S., K   , S., L   , H. & U   , H.S. 2005 Sharp interface Cartesian grid method I: an easily implemented technique for 3D moving boundary computations. *J. Comput. Phys.* **210** (1), 1–31.

M   , S. & L   S   , S.G. 2009 Resonance and propulsion performance of a heaving flexible wing. *Phys. Fluid* **21**, 071902.

M   , R. 1999 A Fourier–Chebyshev spectral collocation method for simulating flow past spheres and spheroids. *Int. J. Numer. Meth. Fluids* **30** (7), 921–937.

M   , R. & B   , S. 1995 Generation of streamwise vortical structures in bluff body wakes. *Physical Review Letters* **75** (7), 1300–1303.

M   , R., D   , H., B   , M., N   , F.M., V   , A. & L   , A. 2008 A versatile sharp interface immersed boundary method for incompressible flows with complex boundaries. *J. Comput. Phys.* **227** (10), 4825–4852.

M   , R. & I   , G. 2005 Immersed boundary methods. *Annu. Rev. Fluid Mech.* **37**, 239–261.

M   , R., W   , J.J. & N   , F.M. 2002 Symmetry properties of the transitional sphere wake. *AIAA J.* **40** (3), 579–582.

N   , R. & A   , A. 1993 The instability of the steady flow past spheres and disks. *J. Fluid Mech.* **254**, 323–344.

O , M., P   , G., A   , G. & E   , J. 2008 Flight controls and performance chal-
  lenges for mavs in complex environments. In *AIAA Paper*, p. 6508.

O   , D. & P   , M. 1999 Transition to turbulence in the wake of a sphere.
  Phys. Rev. Lett. **83** (1), 80–83.

P, D   & RW, B   1997 The kinematics and performance of fish fast-start swim-
  ming. *J. Exp. Biol.* **200**, 1165.

P   , D. & S   , T.T. 2009 Computation of incompressible flows with immersed bodies
  by a simple ghost cell method. *Int. J. Numer. Meth. Fluids* **60** (12), 1378–1401.

P   , C.S. 2002 The immersed boundary method. *Acta Numerica* **11**, 479–517.

P   , C. S. 1972 Flow patterns around the heart valves. *J. Comput. Phys.* **10**, 252–271.

P   , P., H   , F.S. & T   , M.S. 2003 The effect of chordwise
  flexibility on the thrust and efficiency of a flapping foil. In *Proc. 13th Int. Symp. on
  Unmanned Untethered Submersible Technology: special session on bioengineering
  research related to autonomous underwater vehicles, New Hampshire.*

R   , S., G   -D   , R. & T   , B. 2011 Rather than resonance, flapping
  wing flyers may play on aerodynamics to improve performance. *Proceedings of the
  National Academy of Sciences* **108** (15), 5964.

R   , TN, P   , G., V   , S. & C   , JP 2005 Numerical mod-
  elling of solid particle motion using a new penalty method. *Int. J. Numer. Meth. Fluids*
  47 (10-11), 1245–1251.

R   , H. & W   , X. 2012 Biomechanical behaviors of dragonfly wings: relationship
  between configuration and deformation. *Chin. Phys. B* **21(3)**, 034501.

S   , H. & H   , H. 1995 The formation mechanism and shedding frequency of
  vortices from a sphere in uniform shear flow. *J. Fluid Mech.* **287**, 151–171.

S   , A., V   , S., C   , JP & A   , P. 2008 Eulerian–lagrangian grid
  coupling and penalty methods for the simulation of multiphase flows interacting with
  complex objects. *Int. J. Numer. Meth. Fluids* **56** (8), 1093–1099.

S   , C. & H   , J.H. 1999 Blowfly flight and optic flow. i. thorax kinematics
  and flight dynamics. *Journal of experimental biology* **202** (11), 1481.

S   , T., A   , A. & B   , T. 2009 Vortex wakes of a flapping foil. *Journal
  of Fluid Mechanics* **633** (-1), 411–423.

S   , W., A   , H., C   , S. K., T   , P., K   , C. K., C   , C.E.S. & L ,
  H. 2010 Recent progress in flapping wings aerodynamics and aeroelasticity. *Prog.
  Aerospace Sci.* **46(7)**, 284–327.

S   , W , L   , Y   , T   , J   , V   , D   & L , H   2008 *Aerodynam-
  ics of low Reynolds number flyers.* Cambridge University Press.

S , J. & C , B.J. 1994 Topological visualisation of focal structures in free shear flows. *Appl. Sci. Res.* **53** (3), 375–386.

F S , P.J.S.A. & A , J.J. 2011 Thrust efficiency of harmonically oscillating flexible flat plates. *Journal of Fluid Mechanics* **1** (674), 43–66.

S , M. & D , G. 2003 Lift and power requirements of hovering insect flight. *ACTA Mechnica SINICA* **19(5)**, 458–469.

S , M. & T , J. 2002*a* Lift and power requirements of hovering flight in drosophila virilis. *J. Exp. Biol.* **205**, 2413–2427.

S , M. & T , J. 2002*b* Unsteady aerodynamic force generation by a model fruit fly wing in flapping motion. *J. Exp. Biol.* **205** (17), 55.

S , M. & W , J. K. 2007 Flight stabilization control of a hovering model insect. *J. Exp. Biol.* **210**, 2714–2722.

S , M. & W , J. H. 2003 Aerodynamic force generation and power requirements in forwarding flight in a fruit fly with modeled wing motion. *J. Exp. Biol.* **206**, 3065–3083.

S , S. M., B , M. B. & C , D. R. 1992 Wing bone stresses in free flying bats and the evolution of skeletal design for flight. *Nature* **359**, 726.

T , K. & C , T. 2009 Three-dimensional flows around low-aspect-ratio flat-plate wings at low Reynolds numbers. *J. Fluid Mech.* **623**, 187–207.

T , S. 1956 Experimental investigation of the wake behind a sphere at low Reynolds numbers. *J. Phys. Soc. Japan* **11** (10), 1104–1108.

T , B.W., W , D.R., C , C.J., P , D.R., H , T.L., H , G.A. & B , A.A. 2007 Three-dimensional kinematics of hummingbird flight. *J. Exp. Biol.* **210** (13), 2368–2382.

T , GS, T , MS & G , MA 1993 Optimal thrust development in oscillating foils with application to fish propulsion. *Journal of Fluids and Structures* **7** (2), 205–224.

T , M.S., T , A.H. & H , F.S. 2004 Review of experimental work in biomimetic foils. *Oceanic Engineering, IEEE Journal of* **29** (3), 585–594.

T , MS, T , GS & G , R. 1991 Wake mechanics for thrust generation in oscillating foils. *Physics of Fluids A: Fluid Dynamics* **3**, 2835.

T , Y.H. & F , J.H. 2003 A ghost-cell immersed boundary method for flow in complex geometry. *J. Comput. Phys.* **192** (2), 593–623.

U , H.S., M , R., R , P. & K , A. 2001 A sharp interface cartesian grid method for simulating flows with complex moving boundaries. *J. Comput. Phys.* **174** (1), 345–380.

U   , M. 2005 An immersed boundary method with direct forcing for the simulation of particulate flows. *J. Comput. Phys.* **209** (2), 448–476.

V   , M. & B   , E. 2009 A moving-least-squares reconstruction for embedded-boundary formulations. *J. Comput. Phys.* **228** (18), 6617–6628.

V   , M., F   , T., P   , S., B   , E. & B   , B. 2009 Influence of flexibility on the aerodynamic performance of a hovering wing. *J. Exp. Biol.* **212**, 96–105.

V   , J. J. 1993 *Fish swimming*. London, U. K.: Chapman & Hall.

W   , S. M., T   , A. L. R. & T   , G. K. 2010 Deformable wing kinematics in free-flying hoverflies. *J. R. Soc. Interface* **7**, 131–142.

W   , H., Z   , L., L   , H. & Y   , C. 2003 Measuring wing kinematics, flight trajectory and body attitude during forward flight and turning maneuvers in dragonflies. *J. Expl. Biol.* **206** (4), 745.

W   , Z.J. 2005 Dissecting insect flight. *Ann. Rev. Fluid Mech.* **37**, 183–210.

W   , Z.J., B   , J.M. & D   , M.H. 2004 Unsteady forces and flows in low Reynolds number hovering flight: two-dimensional computations vs robotic wing experiments. *J. Exp. Biol.* **207** (3), 449–460.

W   , Z. J. 2000 Two dimensional mechanism for insect hovering. *Phys. Rev. Letters* **85**, 2216.

W   , D.R., T   , B.W. & P   , D.R. 2009 Lift production in the hovering hummingbird. *Proc. R. Soc. B* **276**, 3747–3752.

W   -F   , T. 1973 Quick estimates of flight fitness in hovering animals, including novel mechanisms for lift production. *J. Exp. Biol.* **59**, 169–230.

W   -F   , T. & J   , M. 1956 Biology and physics of locust flight. I. basic principles in insect flight. a critical review. *Phil. Trans. R. Soc. Lond. B* **239**, 415–458.

W   , C.H.K. 1992 The natural and forced formation of spot-like 'vortex dislocations' in the transition of a wake. *J. Fluid Mech.* **243**, 393–441.

W   , R.J. 1981 Support and deformability in insect wings. *Journal of Zoology* **193** (4), 447–468.

W   , R.J. 1992 Functional morphology of insect wings. *Annual review of Entomology* **37** (1), 113–140.

W   , R.J. 1993 Leading edge section and asymmetric twisting in the wings of flying butterflies (insecta, papilionoidea). *Journal of Experimental Biology* **180** (1), 105.

W   , RJ, H   , RC, Y   , PG & E   , KE 2003 Approaches to the structural modelling of insect wings. *Phil. Trans. R. Soc. Lond. B* **358**, 1577–1588.

W , P., I   , P. & S   , B. 2010 Flapping wing structural deformation and thrust correlation study with flexible membrane wings. *AIAA journal* **48** (9), 2111–2122.

W , T. Y   -T   . 1961 Swimming of a waving plate. *J. Fluid Mech.* **10**, 321–344.

W , T. Y   -T   . 1971 Hydromechanics of swimming propulsion. *J. Fluid Mech.* **46**, 521.

Y   , J.M. & B   , E. 2006 An embedded-boundary formulation for large-eddy simulation of turbulent flows interacting with moving boundaries. *J. Comput. Phys.* **215** (1), 12–40.

Y   , B. & L   , H. 2010 Effect of wing inertia on hovering performance of flexible flapping wings. *Phys. Fluids* **22**, 111902.

Y   , J., W   , S.M., B   , R.J., T   , G.K. & T   , A.L.R. 2009 Details of Insect Wing Design and Deformation Enhance Aerodynamic Function and Flight Efficiency. *Science* **325** (5947), 1549.

Z   , Q. 2007 Numerical simulation of a flapping foil with chordwise or spanwise flexibility. *AIAA J.* **45** (10), 2448–2457.